Adhesion and dissipation at nanoscale

Tianjun Li

T H È S E

en vue d'obtenir le grade de

Docteur de l'Université de Lyon, delivré par l'École Normale Supprieure de Lyon

en cotutelle aver / International co-direction of doctoral thesis with

East China Normal University (Shanghai)

Discipline : Physique

Laboratoire de Physique de l'ENS de Lyon

École Doctorale de Physique et Astrophysique de Lyon

présentée et soutenue publiquement le 10 octobre 2013

par Monsieur Tianjun LI

Adhesion and dissipation at nanoscale

Thèse en cotutelle dirigée par :

Directeur de thèse : Ludovic Bellon
Co-directeur de thèse : Zhuo Sun

Devant la commision d'examen formée de :

Rapporteur :	Thierry ONDARÇUHU	-	CEMES-CNRS, Toulouse
	Yafei ZHANG	-	SJTU, Shanghai
Directeur de thèse :	Ludovic BELLON	-	ENS de Lyon, Lyon
Directeur de thèse :	Zhuo SUN	-	ECNU, Shanghai
Invité	Artyom PETROSYAN	-	ENS de Lyon, Lyon

Abstract

In this thesis, we test some interactions involving surfaces processes at the nanometer scale. The experiments are conducted with a highly sensitive interferometric Atomic Force Microscope (AFM), achieving a resolution down to $10^{-28}\,\mathrm{m}^2/\mathrm{Hz}$ for the measurement of deflection. Combined with original thermal noise analysis, this tool allows quantitative characterization of the mechanical response of micrometer and nanometer sized systems, such as microcantilevers or carbon nanotubes, on a large frequency range.

The first part of my work deals with the viscoelasticity of the coating of AFM cantilevers. Evidenced by a $1/f$ thermal noise at low frequency, this phenomenon is present when a cantilever is coated with a metallic layer (gold, aluminium, platinium, etc...). Using the fluctuation dissipation theorem and Kramers Kronig relations, we extract the frequency dependance of this viscoelastic damping on a wide range of frequency (1 Hz to 20 kHz). We find a generic power law dependence in frequency for this dissipation process, with a small negative coefficient that depends on materials. The amplitude of this phenomenon is shown to be linear in the coating thickness, demonstrating that the damping mechanism takes its roots in the bulk of the metallic layer.

The second part of my work tackles new experiments on the interaction of carbon nanotubes with flat surfaces. Using our AFM, we perform a true mechanical response measurement of the rigidity and dissipation of the contact between the nanotube and the surface, in a peeling configuration (the nanotube is partially absorbed to the substrate). The results of this protocol are in line with the dynamic stiffness deduced from the thermal noise analysis, showing an unexpected power law dependence in frequency for the contact stiffness. We suggest some possible physical origins to explain this behavior, such as an amorphous carbon layer around the nanotube.

Keywords : Interferometer, dissipation, Van der Walls force, adhesion, single wall carbon nanotube (SWNT), microcantilever, AFM

Résumé

Ce travail de thèse est dédié à l'étude de quelques phénomènes de surface impliquant des processus d'interactions à l'échelle nanométrique. Les expériences sont réalisées à l'aide un microscope à force atomique (AFM) à grande sensibilité, utilisant un interféromètre différentiel permettant d'atteindre une résolution de $10^{-28}\,\mathrm{m}^2/\mathrm{Hz}$ dans la mesure de la déflexion de la sonde de force. Combiné à une approche originale d'analyse du bruit thermique, cet outil permet une caractérisation quantitative de la réponse mécanique de systèmes de taille micrométrique et nanométrique, tel que des micro-leviers ou des nanotubes de carbone, sur une large plage de fréquence.

La première partie de mon travail porte sur la viscoélasticit
e du revêtement de leviers AFM. Mis en évidence par un bruit thermique en $1/f$ à basse fréquence, ce phénomène est présent lorsque le micro-levier est recouvert d'une couche nanométrique de métal (or, aluminium, platine, etc.) À l'aide du théorème fluctuation-dissipation et des relations de Kramers-Kronig, nous mesurons la dépendance en fréquence de cet amortissement viscoélastique dans une large gamme de fréquence (1 Hz à 20 kHz). Nous observons une dépendance en fréquence générique sous la forme d'une loi de puissance pour ce processus de dissipation, avec un petit coefficient négatif qui dépend du matériau considéré. L'amplitude de cet effet est linéaire avec l'épaisseur du revêtement, démontrant ainsi que le mécanisme de dissipation est une propriété du volume de la couche métallique plutôt que de ses interfaces.

La deuxième partie de mon travail se concentre sur de nouvelles expériences sur l'interaction de nanotubes de carbone avec des surfaces planes. En utilisant notre AFM, nous réalisons une mesure directe de la réponse mécanique (raideur, dissipation) du contact entre le nanotube et la surface, dans une géométrie de pelage (le nanotube est partiellement adsorbé sur la surface). Les résultats de ce protocole sont en accord avec la mesure de la raideur dynamique déduite de l'analyse du bruit thermique, démontrant une dépendance inattendue en loi de puissance de la raideur du contact en fonction de la fréquence. Nous proposons quelques origines physiques possibles pour expliquer ce comportement, tel qu'une couche de carbone amorphe autour du nanotube.

Mots clefs : interfèromètre, dissipation, force de Van der Walls, adhésion, nanotube de carbone mono-paroi, micro-levier, AFM

Acknowledgements

I am so emotional when it is time to write my thankful words to some people, they play an indispensable role in the preparation of this thesis, they are also one of the most important people in my life.

I would like first to give my deepest gratitude to Professor Ludovic BELLON, my supervisor, for his constant encouragement and guidance from the day I had arrived in Lyon. In my heart, ludovic is a very warmhearted, very intelligent and very patient professor. During nearly 3 years of work in the laboratory, I have learnt not only huge amount of knowledge about a novel tool to probe the adhesion property of the nanotube, but also lots of working attitudes, that is always being direct, being perfect, always believe every problem has its resolution, and the most critical, being academically stringent. To a large extent, they will influence me in my future work.

I would like to express my heartfelt gratitude to my chinese director Professor Zhuo SUN, who had helped guid me into the mysterious scientific world during my mater in China, for his new ideas and consistent various support during my PhD. Zhuo is a very kind, facetious professor, he is alway the right man when you seek help. With his recommendation, I got the precious opportunity of the support of Chinese Scholarship Council to start my study in France in 2010. He has provided me lots of novel comments about my work, some are probably becoming my future research interests.

My deepest gratitude would like to go to Professor Artyom PETROSYAN, senior engineer of my laboratory. I would say I spent half of my working time with him. He is a very warmhearted, very conversable man, he can always surprise you because he seems to know every corner in the lab, he can find everything you want even say with his eyes covered. He has given me a lot of guidance to make me be familiar with the new lab, including every corner, of course. In experiment, he has helped me design small but critical systems in my thesis, even this takes him couples of days.

I would like to give my thanks to Professor Athony AYARI in LPMCN, Lyon 1 university for his direction in the growth of single wall carbon nanotube.

I want to express my thankful words to Professor Yafei Zhang in Shanghai Jiaotong University, Professor Thierry ONDARCUHU in CEMES-CNRS, Professor Sumei HUANG in ECNU, Professor Zhenjie ZHAO in ECNU, Jun SHEN in Tongji University for accepting to be referees of this manuscript, ...

My gratitude would also go to my colleages in ENS de Lyon : Felipe AGUILAR SANDOVAL, Audrey STEINBERGER, Clemence DEVAILLY, Mickael GEITNER, Antoine BERUT, Justine LAURENT, Caroline CRAUSTE. It is a memorable time working with them, they are all nice, they make me feel at home. They have also helped me well understand french culture and improved me a lot in my oral french.

I would also give my grateful words to the financial support during my PhD : China Scholarship Council, Coopérations et mobilité international Rhone-Alpes, and ANR (Agence Nationale de la Recherche) project "High resolution adhesion force measurement".

Finally, I would like to sincerely thank my wife Li Zhang, my parents and sisters. They are always there backing me, I love them !

Table des matières

Chapitre 1

Introduction

Nowdays, it is being a global trend that man made devices become smaller and smaller, in a quest to integrate more and more functionality in portable objects (oscillators as time base, accelerometers, sensors, etc.). Moreover, smaller devices means less energy consumption for the same function, which is consistent with the expectation of establishing a environment-friendly and low-carbon emission modern society. However, these technological developments are far from straightforward and some fundamental research is needed to help overcoming the physical and technological issues involved when the devices are reaching micrometer and nanometer scales. Among these issues, surface effect is of great interest to physicists since when the size of the devices drops to nanoscale, a highly increased surface to volume ratio is expected, this means that surface properties are very important at lower scales, and may drive the mechanical properties of tiny objects.

For example, single wall carbon nanotubes (SWCNTs) are well known for its unique mechanical, electrical, thermal and chemical properties and are chosen as potential materials in nano-scale systems. In these systems, the interaction between the nanotube and the rest world is realized through Van der Walls (VdW) force, which is undoubtedly a key point in the physics of nano-systems. Studying the interaction between the nanotube and the rest world is a special case of interesting topics in unveiling the surface effect at nanoscale.

Another new problem that arises at nano scale is importance of the thermal noise driven fluctuations, it can be a limit to the operation or precision of the small systems, and it is also important to understand its mechanism. In this work, I will present a tool to measure this thermal noise and use its information to gain more insight in the physics of surface effects in nano-systems.

For example, when an microcantilever is in equilibrium with the environment, it suffers the excitation of thermally induced noises. Measuring its fluctuations can lead directly to the study of thermal noise. We need thus special tools in order to measure the tiny deformations. Our home built interferometer allows this measurement, due its high resolution in sensing the deflexion of the cantilever. It is a useful tool to later interpret these fluctuations in terms of the system response from statistical physics : in the Fluctuation Dissipation Theorem (FDT), the Power Spectrum Density (PSD) of thermal fluctuation is linked to the response function of the systems. Measuring the thermal noise can give us access to explore the mechanical properties of microcantilevers. For instance, it is used in calibration of cantilevers to get precise stiffness, resonant frequency and quality factor values.

While the thermal noise is seen as a limitation to the performance of nano-systems, the FDT tells us that loss in resolution in smaller devices is related specifically to the losses of energy occurring during the deformations. Therefore, understanding the roots and behaviors of damping of the system become a meaningful and challenging subject. In this thesis, I will study the various damping sources of a cantilever with a metallic coating and the adhesion and dissipation properties of a carbon nanotube through thermal fluctuations.

Let me briefly outline this manuscript : In chapter 2, I will give a short introduction about our home made interferometer. Thanks to its ultra low background noise, we obtain the PSD of deflexion of the cantilever in a wide frequency range. In chapter 3, using the FDT and Kromers-Kronig's relations, we reconstruct the response function of the system, this allows us to access to the sources of damping of the cantilever : viscous damping due to the air and viscoelastic damping due to the metallic coating. In chapter 4, we will study the adhesion force of a single wall carbon nanotube pushed perpendicularly against a flat surface, we access direct quantitative characterization of the adhesion property of nanotube : from the measured adhesion energy the diameter of peeled nanotube is also estimated. In chapter 5, I will show that by measuring the force plateaux on various substrates, the adhesion energy of the nanotube is substrate dependent. In chapter 6, I will present an experiment to measure dynamic peeling stiffness of a nanotube. When the nanotube is peeled away from the surface, its peeling stiffness and peeling dissipation are shown to be frequency dependent.

Chapitre 2

Quadrature phase interferometer

Contents

2.1 Introduction

Atomic Force Microscopy (AFM), that has been invented by Binnig, Quate and Gerber [1] more than 20 years ago, has become a indispensable tool that is used widely in numerous fields, such as material science [2, 3, 4, 5], biological science [6, 7, 8, 9, 10], nanotechnology [11, 12] and so on. Thanks to its high resolution property which is of the order of the nanometer, one can use it to image, measure, and even manipulate matter at the nanoscale for scientific research.

Far before the invention of the AFM technique, interferometric devices have been investigated and use widely in science and industry for the measurement of small displacements, refractive index changes and surface irregularities [13, 14, 15, 16, 17, 18, 19]. In analytical science, interferometers are used in continuous waves Fourier transform spectroscopy to analyze light containing features of absorption or emission associated with a substance or mixture [20]. At large scale, an astronomical interferometer consists of two or more separate telescopes that combine their signals, offering a resolution equivalent to that of a telescope of diameter equal to the largest separation between its individual elements [21].

Interferometer have been used in early ages of AFM to record the cantilever deflexion. The introduction of the optical lever technique [22] however, much simpler to implement and still very sensitive, limited those techniques to a few specialized application where optical access to the cantilever is restricted or the ultimate precision of the measurement is important [23, 24, 25]. Our study of thermal fluctuationa at nanoscale belongs to the latter category, that is lowering the detection noise to get more information about small displacements. To lower the detection noise, we use a quadrature phase interferometer in the context of AFM measurement. This

technique has been first introduced by my supervisor Ludovic BELLON [26], I will give a quick presentation of the setup in chapter 2.

In this chapter, I would like first to present briefly this quadrature phase interferometric setup, then to introduce the measurement of the thermal fluctuations with this highly sensitive tool. The quadrature phase interferometer is based on a differential interferometry approach [27, 19] : two beams are produced by a birefringent element, the first beam is reflected on a static reference region of the cantilever, the second beam is reflected on the free end of the cantilever (illustrated in figure 2.1). The optical path difference between the two beams is thus linked to the deflexion d of the cantilever.

2.2 Quadrature phase interferometric AFM

2.2.1 Configuration of setup

The strategy to produce the two beams in the measurement area is inspired by reference [19], where a calcite prism is used. Calcite beam displacers are made from $CaCO_3$, they split the linearly polarized input beam of light into two orthogonally polarized rays which exit parallel to each other. The ordinary polarization transmits straight through while the extraordinary transmits through the crystal making approximately 6° with the straight through beam and emerges parallel to it. The lateral displacement is thus one tenth of the thickness of the plate. Before the beam passes through the calcite, it crosses a Glan-Taylor prism and an half-wave plate, as shown in figure 2.4. With the Glan-Taylor prism, we obtain a beam with high linear polarization. The half-wave plate is used to tune easily the angle of the linear polarization with respect to the calcite axes, this way, we can tune the relative intensity of the 2 laser beams (reference and sensing beams) so that they are equal after reflexion, we can by such maximize the contrast. This angle corresponds to 45° with respect to the calcite birefringent axes. The calcite beam displacer has a thickness of 2 mm, the displacement between the produced ordinary and extraordinary beams is around 200 µm, as illustrated in figure 2.2. By such, we have polarized sensing beam being focused on the tip of the cantilever, with reference beam being focused close to the base of the cantilever. Note that, here the displacement produced by the calcite is 200 µm, smaller than the common length of the cantilever 450 µm, the reference beam is thus not exactly focused on the base, we have to make a correction in order to measure the actual deflexion of the cantilever (this work will be presented in section 2.2.4).

After reflexion, the two beams are merged back together by the birefringent components and can be measured in the analysis area that I will introduce later in this chapter. The optical path difference δL is twice the deflexion d of the free end of the cantilever :

$$\delta L = 2d \tag{2.1}$$

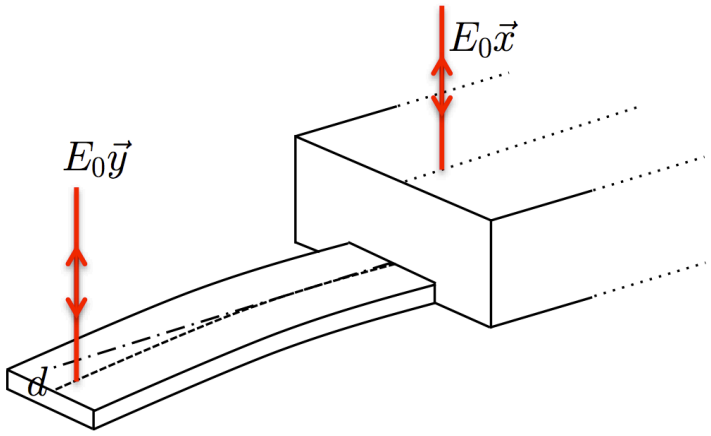

FIGURE 2.1 – Two parallel laser beams are focused on the cantilever, the reference beam $E_0\vec{x}$ is reflected on the flat chip of the cantilever and the sensing beam $E_0\vec{y}$ is reflected on the tip. Any changes in the optical path between the two beams is used to extract the information about the deflexion d of the cantilever.

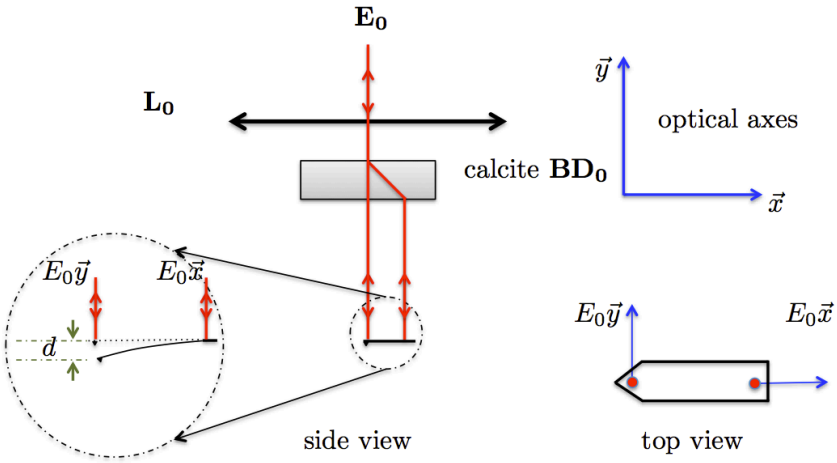

FIGURE 2.2 – Measurement area : the incident beam (electric field $E_0(\vec{x}+\vec{y})$) is focused on the cantilever by the lens L_0. When passing through a calcite beam displacer BD_0 with orthogonal axes $\vec{x}$ and $\vec{y}$, light is split into 2 parallel beams, which are reflected by the base and free end of the cantilever. Deflexion d of the cantilever increases the optical path of the second beam by $\delta L = 2d$. On the top view, blue arrows show the direction of polarizations of the beams.

For the reflexion of the two beams on the cantilever, one of the problem we have to take into account is the intrinsic curvature of the cantilever. When it is coated with a metallic layer to enhance the reflectivity or used in some other applications (for instance, gold (Au) is commonly used as a functionalization material for the adsorption of specific chemical compounds), the metallic coating may produce internal stress which can lead to a static curvature along the cantilever. Strategies to minimize this effect are used (symmetric coating for example), however, avoiding any small bending curvature is still a hard requirement. In our case, the two light beams need to be overlapped in order to record interferences, and the bending curvature of the cantilever generate a spatial separation of the 2 polarizations. For instance, a small 2° curvature (typical tolerance of commercial cantilevers) translate the two interferometric beams into 2 mm separation after the two beams pass through the lens which focusing length is 30 mm. In such a case, the obtained interference is too small to get sufficient contrast.

To address such problem, the strategy we use in the setup is that we split the two beams using a Wollaston prism [1], as illustrated in figure 2.3. This is very similar with reference [15] : the initial beam (field $E_0(\vec{x}+\vec{y})$) first passes through a Wollaston beam splitter, which produces 2 rays of orthogonal polarizations ($E_0\vec{x}$ and $E_0\vec{y}$), with an $\alpha = 2°$ separation angle. If the point where the two beams come out is placed at the focal point of the lens, the optical axes of the two beams are parallel, this is equivalent to the calcite configuration. However, using a translation of the wollaston along the optical axis, we can change the angle of incidence of the beam on the cantilever. Cantilever with any small static curvature can be effectively compensated in this Wollaston configuration.

The distance between the 2 focalization points is given by the angular separation of the prism $\alpha = 2°$ and the focal length f =30 mm, that is 1 mm in the setup, this distance is always much longer than the length of the cantilever, the reference beam is thus always reflected on the chip of the cantilever. For the comparison of the measurement between the Wollaston configuration and the calcite configuration, one can find description in detail in reference [29].

2.2.2 Interferometer : analysis area

As presented in section 2.2.1, after reflection, for both configurations, the 2 beams are merged into one single beam, the optical path difference between them is thus a linear function of the deflexion of the cantilever (equation (2.1)).

The analysis area in our setup is based on the quadrature phase technique [26, 30], as illustrated in figure 2.4 : the beam is separated in two equivalent

1. A Wollaston prism is an optical device, invented by William Hyde Wollaston, it is used to manipulates polarized rays. In our case, it separates linearly polarized beam into two orthogonal polarized outgoing rays. The Wollaston prism consists of two orthogonal calcite prisms, cemented together on their base (traditionally with Canada balsam) to form two right angle prisms with perpendicular optic axes. Outgoing light beams diverge from the prism, giving two polarized rays, with the angle of divergence 2° between the two rays. Commercial prisms are available with divergence angles from 2° to about 45° [28].

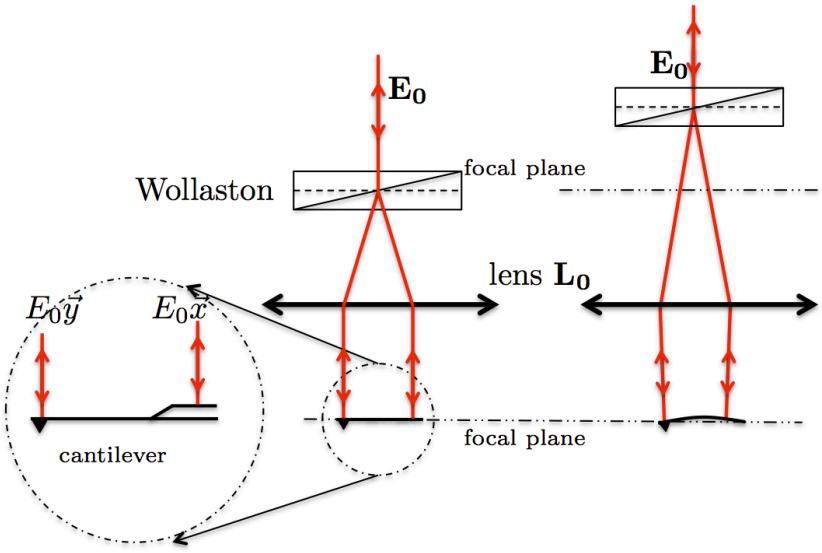

FIGURE 2.3 – Wollaston configuration : the incident beam ($E_0(\vec{x}+\vec{y})$) is splited into 2 orthogonal polarizations ($E_0\vec{x}$ and $E_0\vec{y}$) by the Wollaston prism, then are focused on the cantilever by the lens L_0. Translating the position of the Wollaston along the optical axis, any small static curvature of the cantilever can be compensated, after reflection, the two beams are merged back and can interfer with each other in the analysis area. A difference with figure 2.2 is the distance between the two beams : this is 1 mm, which is longer than the length of the cantilever, the reference beam ($E_0\vec{x}$) is thus reflected on the chip.

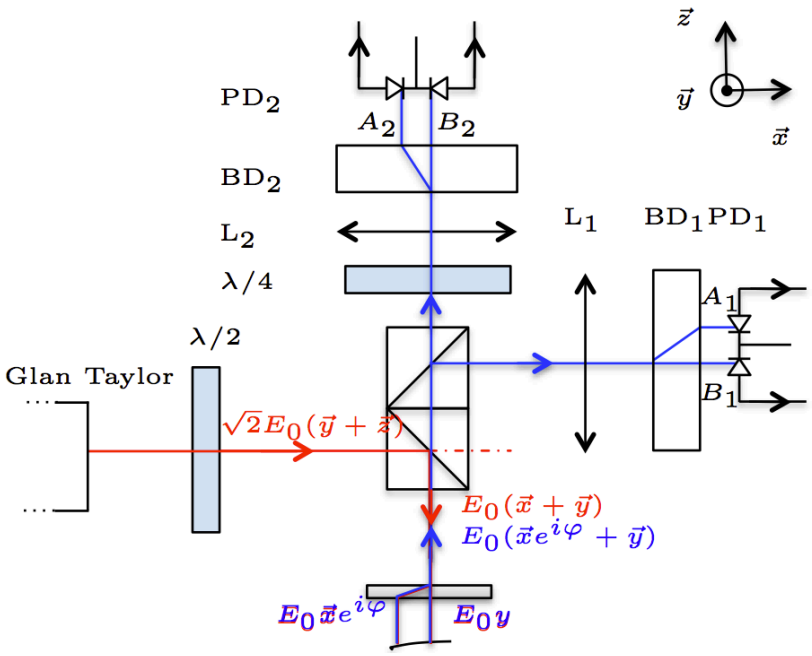

FIGURE 2.4 – Interferometer configuration : The polarized laser beam is fed into the setup (red arrow) through a Glan Taylor prism and half wave plate. The merged two beams with an optical path difference (blue arrow) coming from the measurement area are splitted into two beams by a cube beam splitter, indexed with subscript $n = 1, 2$ (the overlapped beams in the figure stands for the beams before (red) and after (blue) reflexion.). To have the beams interfere we use a 5 mm calcite prism (BD_n) oriented at 45° with respect to the birefringent component (BD_0 or Wollaston). The two beams exiting BD_n are focused by a plano convex lens (L_n, f =25 mm) on the 2 segments of a 2 quadrant photodiode PD_n to record their intensities A_n, B_n. In the second analyzing beam ($n = 2$), a quarter wave plate ($\lambda/4$) is added in order to add $\psi_2 = -\pi/2$ to the phase shift ψ.

arms (indexed with subscript $n = 1, 2$) by a non polarizing cube beam splitter, then is focused on the photodiodes by a plano convex lens (L_n, focal length=25 mm). To record interferences, the beams exiting the cube beam splitter are projected by two calcite beam displacers (BD_n, thickness=5 mm) whose axes are at 45° with respect to the optical axes of the birefringent component (BD_0 or Wollaston). The two beams exiting from each calcite prism have a distance 0.5 mm with each other, they are collected by the two segments of a 2 quadrant photodiode (*UDT* Spot-2DMI). The only difference between the two arms is the addition of a quarter-wave plate in the second arm, subtracting $\pi/2$ to the phase shift between the two polarizations.

Let us define the unity vectors along the optical axes of the calcite BD_0 as $\mathbf{x}$, $\mathbf{y}$, the electric field of the input beam in the setup (red color beam in the figure 2.4) is thus described as $\mathbf{E}_0 = \sqrt{2}E_0(\mathbf{y}+\mathbf{z})$. The electric field of the beam after reflection is given by $E_0(\mathbf{x}+e^{i\varphi}\mathbf{y})$, where φ the phase shift between the polarizations due to the deflexion of the tip of the cantilever. Since the phase difference follow $\Delta\varphi = 2\pi\Delta L/\lambda$ with respect to the optical path difference, and the optical path difference is twice the deflexion d of the tip, φ is thus given by :

$$\varphi = \frac{4\pi}{\lambda}d \tag{2.2}$$

where λ =633 nm is the wavelength of the He-Ne laser we use. Hence the intensities of the projected beams on the 2 quadrants of the photodiodes are :

$$\begin{aligned} A_n &= \frac{I_0}{4}(1+\cos(\varphi+\psi_n)) \\ B_n &= \frac{I_0}{4}(1-\cos(\varphi+\psi_n)) \end{aligned} \tag{2.3}$$

where subscript n links to the analysis arms ($n = 1, 2$), $I_0 = E_0^2$ is the total intensity of the incident beam, $\psi_1 = 0$ for the first arm, $\psi_2 = -\pi/2$ for the second arm with a quarter wave plate. Using home made low noise preamplifiers and post-acquisition digital signal processing, we can measure the contrast of the two signals (A and B) of each arm :

$$C_n = \frac{A_n - B_n}{A_n + B_n} = \cos(\varphi+\psi_n) \tag{2.4}$$

thus C_1, C_2 can be expressed as :

$$C_1 = \cos\varphi, C_2 = \sin\varphi \tag{2.5}$$

This way, the contrasts of the two signals do not dependent on the fluctuation of the laser intensity I_0. Let us rewrite the equation 2.5 as :

$$C = C_1 + iC_2 = \cos(\varphi) + i\sin(\varphi) = e^{i\varphi} \tag{2.6}$$

The obvious advantage of using two analyzing arms rather than one is : it allows one have a complete determination of φ (modulo 2π). In the (C_1, C_2) plane, the measurement will lay on the unit circle, its polar angle being the optical phase

shift φ. The sensitivity to measure a small deflexion of the cantilever tends to be independent of the static deflexion and the intrinsic optical path difference :

$$\left|\frac{\mathrm{d}C}{\mathrm{d}d}\right| = \left|e^{i\varphi} i \frac{\mathrm{d}\varphi}{\mathrm{d}d}\right| = \frac{4\pi}{\lambda} \tag{2.7}$$

To measure the deflexion d of the the cantilever, what we need is the two contrast C_1 and C_2, the deflexion d is then constructed by standard digital processing tools :

$$d = \frac{\varphi}{4\pi}\lambda = \frac{\arctan(C_2/C_1)}{4\pi}\lambda \tag{2.8}$$

2.2.3 Calibration of the interferometer

In the experiment, the unavoidable imperfections of optical components and of their alignment will lead the complex contrast to lay on a ellipse with radius smaller than 1 rather than a unit circle, the measured contrast is rewritten as :

$$\tilde{C} = C_1^{raw} + iC_2^{raw} = \zeta_1 \cos(\varphi) + c_1 + i(\zeta_2 \sin(\varphi + \psi) + c_2) \tag{2.9}$$

where C_1^{raw} and C_2^{raw} represent the value measured in the experiment, $\zeta_n < 1$ are the contrast amplitudes in each arm, c_n the contrast offsets, and ψ a residual mismatch to perfect quadrature [26].

These 5 parameters can easily be extracted from a calibration of the interferometer : the free cantilever is excited with a large amplitude oscillation by a piezo (the cantilever and the piezo are linked by a specially designed cantilever holder), the excited deflexion of the cantilever changes the optical path of the beams, thus leading to an ellipse in the $\tilde{C}$ plane.

Figure 2.5 illustrates the measured contrast with this excitation at the resonant frequency of the cantilever. The 5 unknown parameters can be extracted by a generic fit of the ellipse. For the Wollaston configuration, we can also produce the ellipse by a lateral translation of the birefringent prism, which also allows us to calibrate the interferomer without oscillating the cantilever : as indicated in figure 2.6, any small translation of the Wollaston prism can modify the initial optical path difference. Once the ellipse is fitted, raw measurement values (C_1^{raw}, C_2^{raw}) can be post processed by equation (2.10) and be projected on a unit circle (ideal value C), to extract the actual deflexion d [26].

$$C = C_1 + iC_2 = \frac{C_1^{raw} - c_1}{\zeta_1} + i\left[\frac{C_2^{raw} - c_2}{\zeta_2} - \frac{(C_1^{raw} - c_1)\sin(\psi)}{\zeta_1}\right]\frac{1}{\cos(\psi)} \tag{2.10}$$

Let us do a simple summary for the key points presented above for the interferometer. The laser beam is split into 2 beams : reference focused on the base chip of the cantilever, sensing beam focused on the free end of the cantilever. The phase difference between the beams after reflexion is linked to the deflexion of the cantilever (equation (2.1)). After reflexion, the two beams are merged back and are split

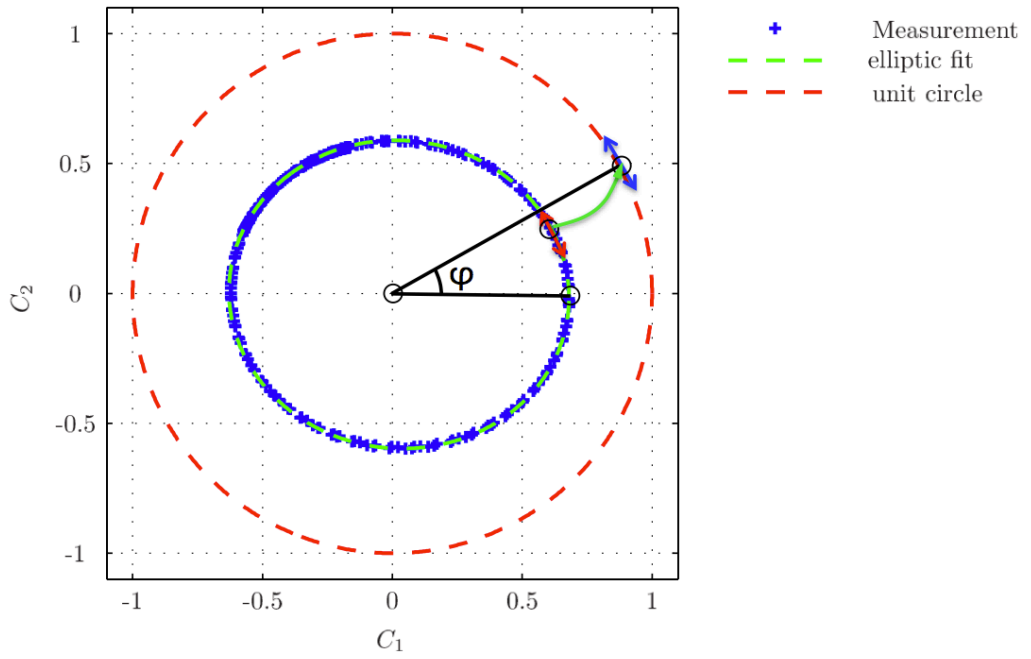

FIGURE 2.5 – Interferometer calibration : the cantilever is excited at its resonant frequency, the measured contrast (blue) lays on an ellipse. After a simple fit (green) of the measured contrast, we can directly project the measurement point (black) on the unit circle (red), and identify its polar angle with the optical phase shift φ

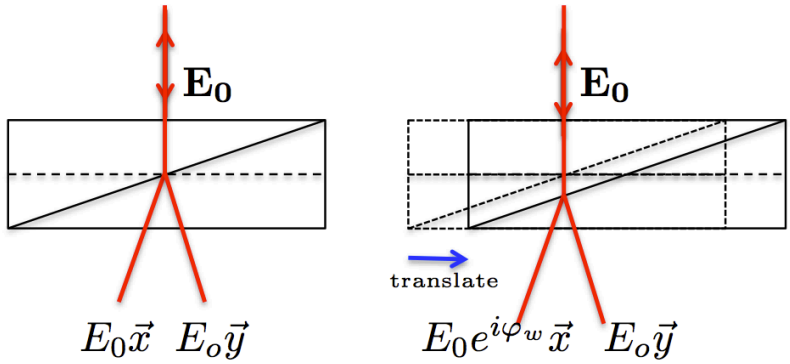

FIGURE 2.6 – Tunning the initial optical path difference : a small translation of the Wollaston prism along the separation axis can modify the optical path of the two polarizations ($E_0\vec{x}$ and $E_0\vec{y}$) inside the birefringent material, adding an optical phase φ_w between the 2 beams.

into 2 arms to measure the interferences, the output of the two arms are C_1^{raw} and C_2^{raw}. The raw measurement of the two signal C_1^{raw} and C_2^{raw} lays on an ellipse with a diameter smaller than one. After fitting and post processing, the data can be used to record precisely any small change of phase that corresponds to the deflexion d by equation (2.8)

2.2.4 Thermal noise measurement

Based on the calibration described above, we can record the fluctuations of the cantilever that are induced by thermal noise : thermal noise behaves like white random noise force which is exciting every modes of the microcantilever when it is in equilibrium with the outside environment. In figure 2.7, we plot the Power Spectrum Density (PSD) of deflexion S_d in a 100 kHz frequency range. The cantilever used here is a *Budget Sensors* Cont-GB-G with overall gold coating covering its both sides. The measurement is performed in calcite configuration. The spectrum indicates the precision of our setup, in the frequency range from 3 Hz to 100 kHz, the limitation of the PSD is the background noise of the setup, around $2 \times 10^{-14}\,\mathrm{m}/\sqrt{\mathrm{Hz}}$. The main source of this noise is the shot noise due to the photodiode we used, it is not avoidable, thus presents a limitation of the setup. To get the intrinsic noise of the setup, instead of focusing the two beams on a cantilever (one beam works as the reference, another as the sensing beam), we move the two beams onto a rigid mirror, and measure the equivalent deflexion, we can thus estimate the background noise that only comes from the apparatus.

The setup is very sensitive to the external perturbation especially at low frequency, where the background noise increases a little higher than that at high frequency. Anyway, the mechanical noise is still everywhere above the background noise, and below the first resonance for this cantilever, ensure us access to a lot of information about the cantilever.

Besides the first resonant frequency that can be clearly found in the figure, another flexural mode around the frequency f =52 kHz can be seen in this 100 kHz frequency range. The obvious $1/f$ like behavior at low frequency is studied in chapter 3.

Figure 2.8 shows a photography of our home-made quadrature phase interferometer with superposed optical path.

2.3 Summary

We present our innovative atomic force microscope (AFM) which detection process is based on a quadrature phase differential interferometer. We measure the difference of phase between the reference beam and the sensing beam, which leads to the precise measurement of the deflexion d of the cantilever. We get a high resolution detection of the deflexion (background noise down to $2 \times 10^{-14}\,\mathrm{m}/\sqrt{\mathrm{Hz}}$). This enables us to measure the power spectrum density on a wide frequency range.

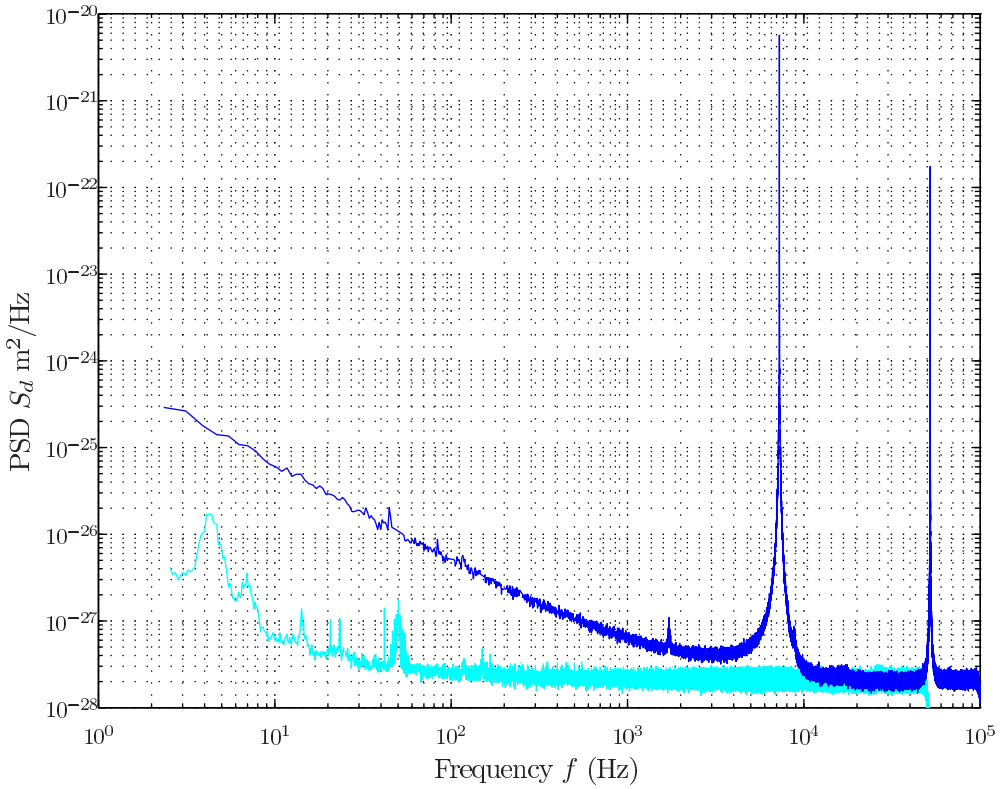

FIGURE 2.7 – Power spectrum density (blue curve) of deflexion and background noise (cyan curve) measured in the calcite configuration of a Au coated cantilever in vacuum. The plotted data indicates the high precision of our interferometer : we obtain a background noise level as low as 2×10^{-14} m/Hz on a wide frequency range. This allows us to obtain not only the first resonant frequency, but also the second mode and the low frequency behavior of the mechanical thermal noise of the cantilever.

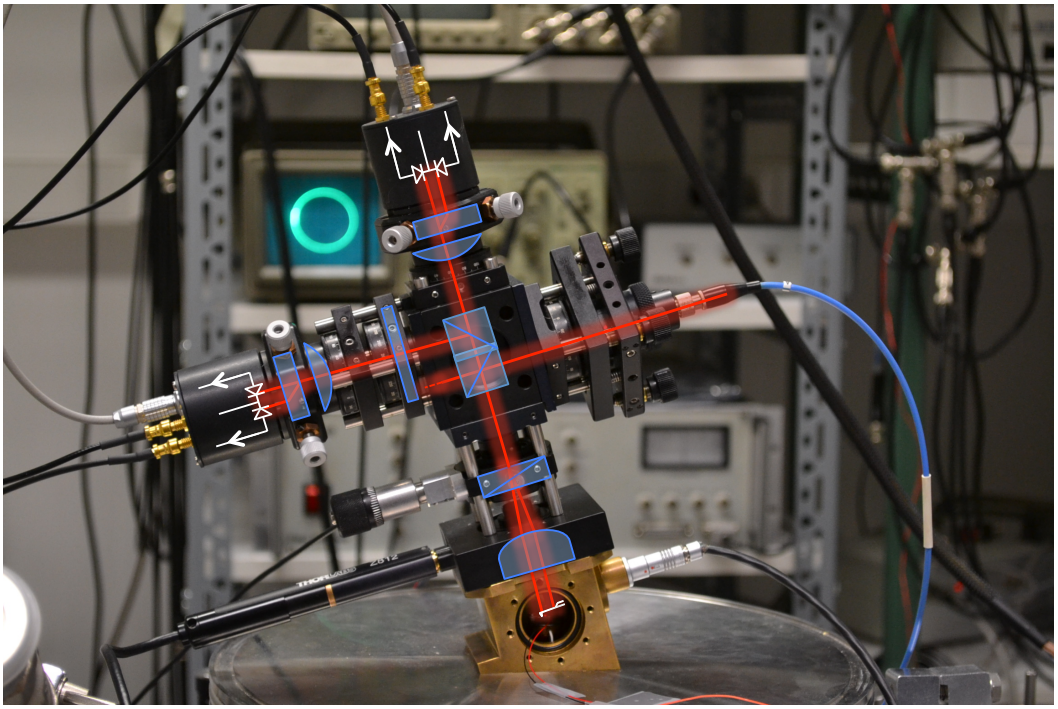

FIGURE 2.8 – Photography of our home-made quadrature phase interferometer for AFM measurement with superposed optical path. The laser beam is fed into the setup by an optical fibre (blue line on the right of the figure). In the background, an oscilloscope in XY mode displays the elliptic trace of the outputs when the optical path difference is created by a large amplitude oscillation of the cantilever ($> \lambda/2$).

The highly sensitive setup allows us to conduct the investigation about the dissipation of a cantilever coated with a metallic layer in chapter 3 and to probe the adhesion behaviors between a single wall carbon nanotube and various substrates in chapter 4.

Chapitre 3

Dissipation of AFM cantilevers

Contents

3.1 Introduction

Microcantilevers exhibit high utility in many fields ranging from biological sensors [31] to scanning probe microscopy [32]. They are also present as an essential part in many microelectromechanical systems (MEMS). Used in Atomic Force Microscopy (AFM), they are used in various studies in terms of force measurement [33], manipulation on a protein [34], topography of biological membranes [35], mechanical response of biological cells [36, 37], MEMS and other nanoscale device applications [38, 31].

The functionality of MEMS, AFM probe or mass sensors is based on the deformation of the cantilever. The sensitivity of the resonant cantilever when used as a mass sensor depends on the spectral resolution, thus of its quality factor Q which is defined as the ratio of stored vibrational energy over energy lost per cycle of vibration [39]. Energy dissipation in the cantilever causes the stored mechanical energy to leak away and be converted into heat. The stronger the coupling between the cantilever and the heat bath, the faster the decay of cantilever motion toward thermal equilibrium and the lower the mechanical quality factor Q of the oscillating mode.

The thermal fluctuation involved in these microscopic systems presents one of the most critical noise source which can determine the sensitivity of these sensors and thus the performance in these devices [40, 41, 31, 42, 43, 44, 39]. Thermal mechanical noise is a consequence of the cantilever being in thermal equilibrium with its environment (i.e. a heat bath with many microscopic degrees of freedom). Besides, this thermal related noise can also have a significant role in macroscopic systems, for example, it is a relevant term in the sensitivity limitations of interferometric detector in the study of gravitational waves [45, 46, 47, 48].

According to the fluctuation dissipation theorem (FTD) [49], the thermal induced fluctuations are linked to the mechanical response function of the system, and more specifically to the losses of energy occurring during its deformations. Therefore, measuring damping on thermal fluctuations should lead to the same physical information. Indeed, though the thermal noise is a limitation for most operations of cantilever, it can also gives us an access to explore the mechanical properties of the micro-sized cantilevers. The most common use of thermal noise is to calibrate the AFM cantilever for parameters of stiffness k, resonant frequency f_0, quality factor Q and so on : the equipartition theorem states that the energy stored in the spring is in average equal to the thermal energy, it indicates how much thermal energy is in each mode of the cantilever :

$$\frac{1}{2}k\left\langle d^2\right\rangle = \frac{1}{2}k_B T \tag{3.1}$$

where k is the spring constant to be calibrated, $\left\langle d^2\right\rangle$ the mean quadratic deflexion, k_B the Boltzmann constant, and T the environmental temperature. This calibration process is necessary, especially when one measures the deflexion of the cantilever with high accuracy to obtain the precise value of force in AFM with a conversion factor from meter to Newton. Normally, it should be easier to derive the parameters of cantilevers, k, f_0, by computing through the geometric dimension description of the cantilever. However, manufacturer nominal values for the geometry have large uncertainty, making it hard to compute a precise value by such estimation. In addition, geometric description of its bulk properties might bring some incertitudes since the surface effects at this scale have also to be taken into account, the common use of metallic coating on the surface of cantilever can add again more errors in this estimation. Therefore, choosing to conduct the calibration based on the thermal noise is often indispensable and it can give us a trustable value for each cantilever, and ensure that one can get the real response of the cantilever, and leading to force measurements with high accuracy.

Many models have been proposed to account for the various physical sources of dissipation : viscous damping from the surrounding medium [50], clamping damping [51], damping resulting from internal friction (internal damping results from a variety of physical mechanisms : motion of lattice defects, thermoelastic dissipation (TED) phonon-phonon scattering, etc) [39]. Traditionally, internal friction is considered as a bulk effect, but surface effects can dominate for submicron-thick cantilevers or for resonators with very high Q [52, 53].

For the study of viscous damping, Sader and co-workers performed a thorough investigation and led to a prediction of a frequency dependent damping coefficient [50, 54, 55]. Saulson and co-workers presented a model focused on structural damping to describe the mechanical-thermal noise for a simple harmonic oscillator with viscoelastic dissipation. Notably, they showed a $1/f$ like trend at low frequency in the power spectrum density in this kind of structural damping [44]. All these models are discussed trying to describe the frequency dependence of the dissipation or the thermal noise. It is thus very interesting to measure directly this structural or fluid related damping or thermal noise experimentally in the frequency space. Up to date, few experiment have succeed in directly measuring the fluctuations out of resonance, specially at low frequency. In this chapter, I will present how our highly sensitive interferometer enable us to measure the Power Spectrum Density (PSD) of the displacement of a cantilever in a large frequency range, and how we can use this spectrum to rebuild the response function of the cantilever.

I will introduce first the Simple Harmonic Oscillator (SHO) model to describe generally an AFM cantilever. Then we consider another model—Jonscher's model, which takes only into account the structural damping, this leads to a $1/f$ like trend at low frequency in PSD of the deflexion. Combination of the two models is used to compare with the measurement.

In chapter 2, we presented a direct measurement of the mechanical-thermal noise of micro-cantilever with our high resolution interferometer. The measured spectrum spans in a wide frequency range that is not only restricted on the resonance as the commercial counterpart does. In section 3.2.4, I will show that, due to the ultra low background noise we obtain, we can access to a full PSD of the deflexion in a wide frequency range after subtracting the background noise. The full range of spectrum enables us to reconstruct the response function by Kramers-Kronig relations. Any change of characteristics in the PSD can be reflected in the response function G of the cantilever, we can thus discuss easily various damping models based on a known G in the frequency space.

Then I will present the first resonance that is well described by SHO model—viscous damping, which is induced by the air fluxing around the cantilever. By removing the impact of the air, the left contribution of the dissipation leads to the second damping source—viscoelasticity. It is a frequency dependent term that is described by a power law with small exponent. By measuring this viscoelasticity on various coated cantilevers, we will indicate that this viscoelasticity is not only frequency dependent but also material dependent. At last, we will discuss various dissipation mechanisms for viscoelastic damping : it is not due to the interface between the cantilever and the coating but to the bulk of the metallic coating.

3.2 Mechanical response function of an AFM cantilever and thermal noise

3.2.1 Simple Harmonic Oscillator (SHO) model

In a first approximation, the AFM cantilever can be modeled by a damped spring-mass system. The displacement d of the punctual mass in the model corresponds to the deflexion of the cantilever, the spring constant k corresponds to the response of the system to the external force F acting on the tip, the mass m corresponds to the inertia of the mechanical system, and the damping coefficient γ corresponds to the dissipation which is brought by the surrounding air or fluid. The equation of motion of this simple harmonic oscillator can be written as :

$$m\ddot{d} = -kd - \gamma\dot{d} + F \tag{3.2}$$

where dotted variables are derivated with respect to time t. Since what we are interested in is the behavior of the system with respect to frequency, we can rewrite its response function in Fourier's space :

$$G(\omega) = \frac{F(\omega)}{d(\omega)} = k\left[1 - \frac{\omega^2}{\omega_0^2} + i\frac{\omega}{\omega_0 Q}\right] \tag{3.3}$$

where we introduce the resonant angular frequency $\omega_0 = \sqrt{k/m}$, the quality factor $Q = m\omega_0/\gamma$, and $\omega = 2\pi f$ the angular frequency corresponding to frequency f.

The infinitesimal work of F when the displacement changes by δd is $\delta W = F\delta d$, for a reversible transformation, $d\widehat{H} = \delta W = F\delta d$, thus we have :

$$\frac{\partial \widehat{H}}{\partial d} = F \tag{3.4}$$

The force F and the displacement d are coupled by the Hamiltonian $\widehat{H}$ of the system. We can apply the Fluctuation Dissipation Theorem (FDT) to the deflexion, the Power Spectrum Density (PSD) S_d^{SHO} of thermal fluctuation of d is :

$$S_d^{\mathrm{SHO}}(f) = -\frac{4k_BT}{\omega}\mathrm{Im}\left[\frac{1}{G^{\mathrm{SHO}}(\omega)}\right] = \frac{4k_BT}{k\omega_0}\frac{1/Q}{(1-u^2)^2 + (u/Q)^2} \tag{3.5}$$

where k_B is the Boltzmann constant, T the temperature of the system, $u = \omega/\omega_0$ is the reduced frequency, and Im(.) is the imaginary part of the argument.

For a given response function of one system, we can estimate the thermal fluctuation $S_d(f)$ by using the FDT. For the SHO model described here, we plot the real part and imaginary part of its response function in figure 3.1, 3.2 and also the thermal fluctuations derived from the FDT in figure 3.3. As is shown in the figures, the real part of the $G^{\mathrm{SHO}}(\omega)$ is a parabolic line centered at $f = 0$, the value at the origin being the spring constant k, the quadratic shape is linked to the inertia of the system. The imaginary part of $G^{\mathrm{SHO}}(\omega)$ is linear with respect to frequency : dissipation is proportional to velocity, thus linear in frequency with a

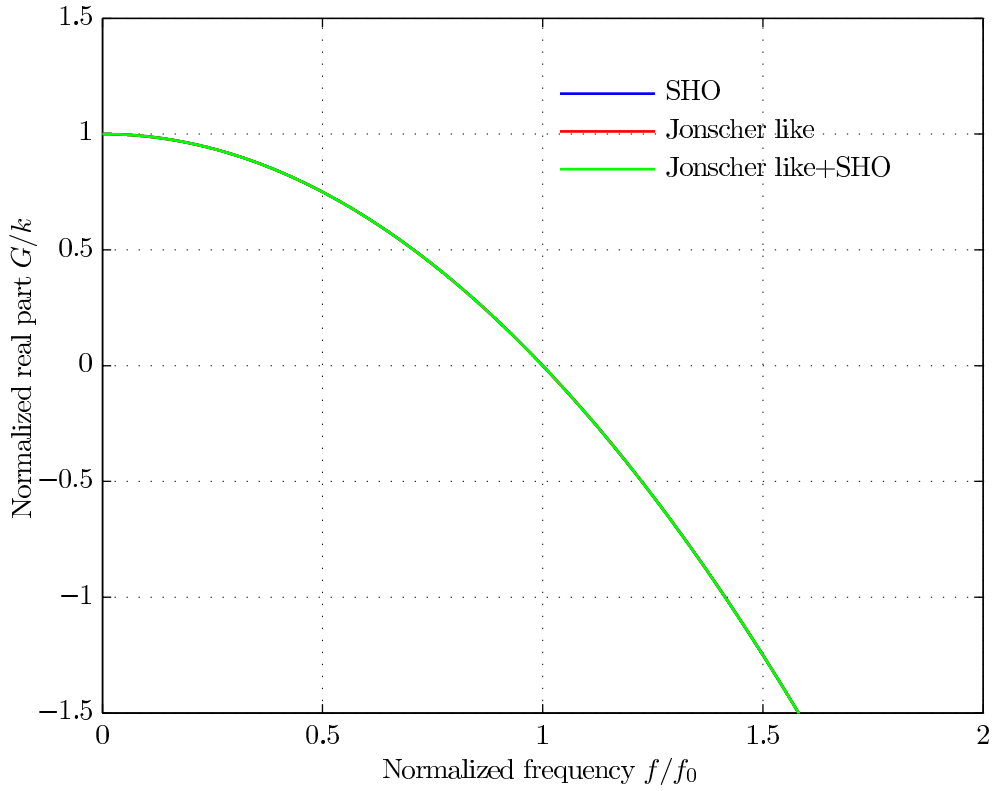

FIGURE 3.1 – Normalized real part of mechanical response function $\mathrm{Re}(G(\omega))$ with stiffness k =0.2 N/m, quality factor $Q = 30$. Frequency f is normalized to the resonant frequency of the cantilever, the real part response G is normalized by the stiffness k. $\mathrm{Re}(G(\omega))$ is a parabola line centered at $f = 0$, the value at the origin being the spring constant k, the quadratic shape is linked to the inertia of the system. The SHO model, Jonscher's like model and the model of their combination present the same curves of $\mathrm{Re}(G(\omega))$.

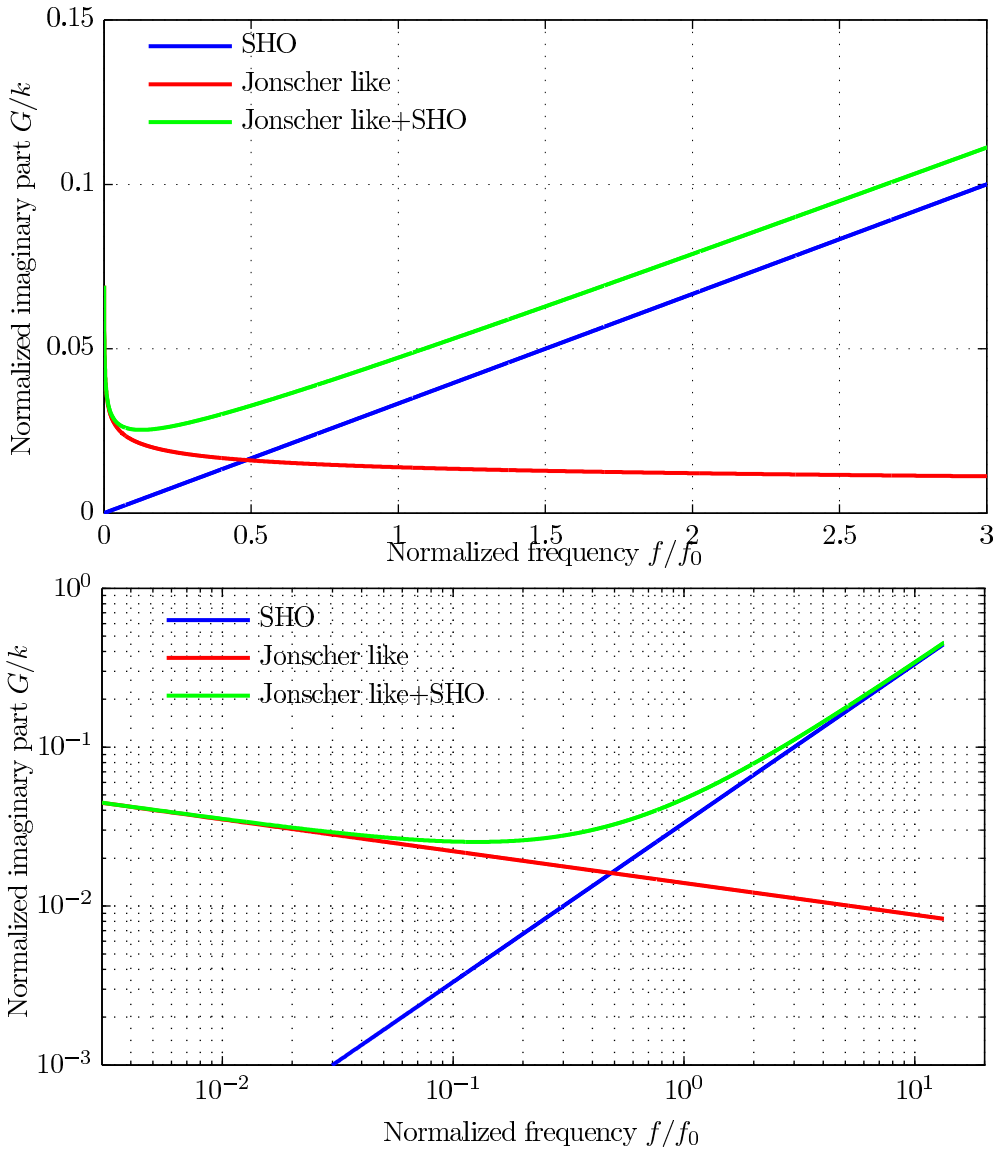

FIGURE 3.2 – Imaginary part of mechanical response function $\mathrm{Im}(G(\omega))$ for the SHO model (blue), Jonscher's like model (red) and the model of their combination (green) with stiffness k =0.2 N/m, quality factor $Q = 30$, $\phi = 10^{-2} \cdot f^{0.12}$. Frequency f is normalized to the resonant frequency of the cantilever, the response G is normalized by the stiffness k. Top graph uses linear scales, bottom graph log scales for both axis, and we plot the same data in both.

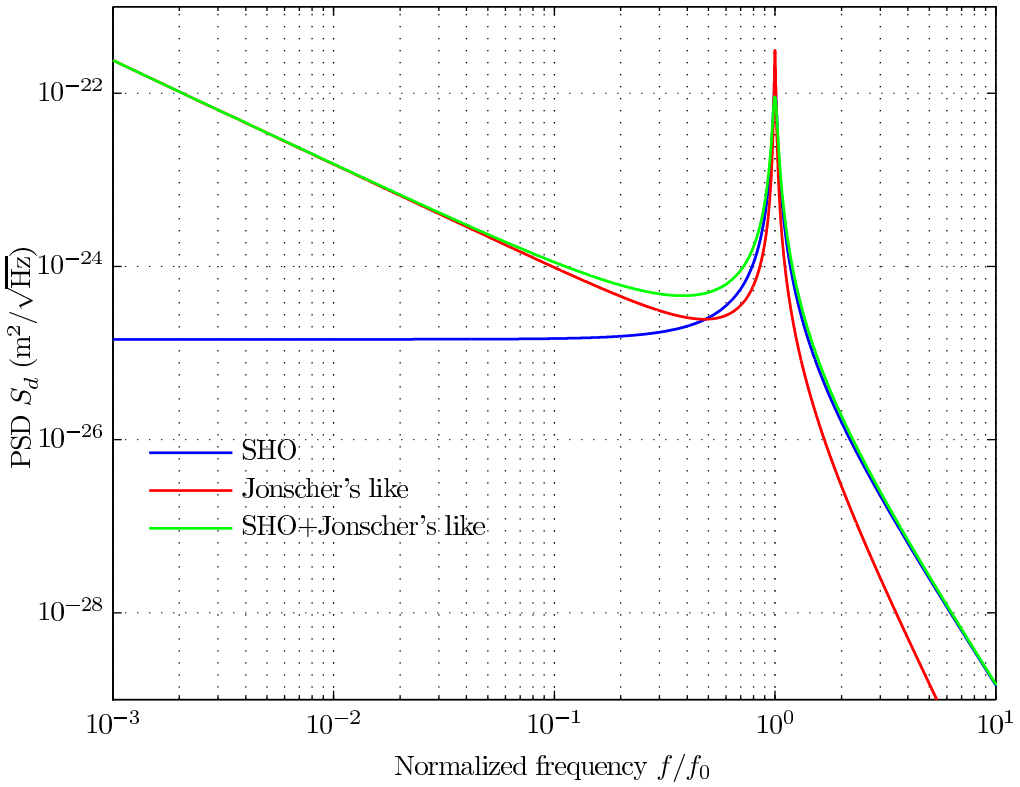

FIGURE 3.3 – Thermal noise spectrum computed using FDT for the SHO model (blue), Jonscher's like model (red) and the model of their combination (green) ($f_0 = 10^4$ Hz, k =0.2 N/m, $Q = 30$, $\phi = 10^{-2} \cdot f^{0.12}$). Frequency f is normalized to the resonant frequency of the cantilever.

slope $k/Q\omega_0$, this is the damping that is induced by the viscous medium fluxing around the cantilever. The $\mathrm{Im}(G)$ starting with a origin 0, meaning no dissipation occurs if there is no any medium fluxing. In the figure 3.3, it is obvious that the spectrum computed by the FTD presents a characteristic Lorentzian shape with the resonant frequency being $f_0 = \omega_0/2\pi$. The physical parameters of the cantilever thus can be inferred from the spectrum : the quality factor being the width of the resonance at half height, the spring constant k can be computed from the integral of the curve using the equipartition theorem.

3.2.2 Saulson's and Jonscher's like model ($1/f$ noise)

The damping we have considered up to now is only a viscous damping, in a more generally case, another damping source can be considered : structural damping, meaning the spring itself may be viscoelastic. Saulson and co-workers proposed a model of mechanical noise for a simple harmonic oscillator with viscoelastic damping [44]. They showed that the PSD of fluctuations present $1/f$ like trend at low frequency. In this model, it is supposed that the stiffness of the cantilever is a complex constant : $k^* = k(1 + i\phi)$ in frequency space.

In the Jonscher like model, Paolino et al. found that the viscoelasticity ϕ is not frequency independent, it follows a simple power law approximation with a small exponent : $\phi(\omega) = \mathrm{Im}(G)/k \propto \phi_0\omega^\alpha$ [56]. If focusing only on this damping, the response function G and the thermal fluctuation S_d^{SHO} are modified as :

$$G^{\mathrm{Im}(k)}(\omega) = k\left[1 - \frac{\omega^2}{\omega_0^2} + i\phi(\omega)\right] \tag{3.6}$$

$$S_d^{\mathrm{Im}(k)}(f) = \frac{4k_BT}{k\omega_0}\frac{\phi(\omega)/u}{(1-u^2)^2 + \phi(\omega)^2} \tag{3.7}$$

We plot the normalized response function and thermal fluctuation in figure 3.1 3.2 and 3.3 in red line with $\alpha = -0.12$, $\phi_0 = 10^{-2}$. The normalized real part is exactly the same with that of SHO model—a parabola centered at $f = 0$, the value at the origin being the spring constant k, the quadratic shape is linked to the inertia of the system. The normalized imaginary part exhibits a different trend with respect to the SHO model, it presents a slight decrease with respect to the frequency. We plot it also in log scale in figure 3.2, it is a line with a small negative slope with respect to the frequency. Note that, in the figure 3.3, a clear difference in the spectrum between the SHO model and Jonscher like model is that there is a $1/f$ like trend at low frequency for Jonscher like model.

Generally, both viscous damping and structural damping contribute to the dissipation of the cantilever, thus we combine the two models :

$$G^{(k^*)}(\omega) = k\left[1 - \frac{\omega^2}{\omega_0^2} + i\left(\frac{\omega}{\omega_0 Q} + \phi(\omega)\right)\right] \tag{3.8}$$

We plot the response function G and thermal fluctuation in figure 3.1, 3.2 and 3.3 in green. In the log scale plot (figure 3.2), the thermal noise of combined model is the sum of the two effects. This will be more clearly illustrated in experimental results by computing the imaginary part of G using Kromer-Kronig relations in section 3.2.4.

3.2.3 Measuring thermal noise spectra

As presented in the chapter 2, due to the ultra low background noise our interferometer reaches, we can measure the PSD of the deflexion of the cantilever in a wide frequency range. We plot the PSD of a gold coated cantilever (*Budget Sensors*, ContGB) in a frequency range from 1 Hz to 40 kHz in figure 3.4, both of its sides are coated with a gold coating of thickness of 70 nm : the measured spectrum features a $1/f$ like trend at low frequency, it is in line with the Jonscher like model, the $1/f$ like trend is related to the structure of the cantilever.

One may argue that the background noise in the figure 3.4 adds a contribution to the mechanical noise that might cause the special behavior at low frequency. However the level of the background noise in the spectrum is quite low at around $1.8 \times 10^{-28}\,\mathrm{m}^2/\mathrm{Hz}$, as is indicated in the figure (black line). We can thus subtract this noise from the spectrum, which will result in the pure PSD signal of the mechanical fluctuations of the cantilever.

$$S_d = S_d^{measure} - S_d^{background} \tag{3.9}$$

Once being subtracted the background noise, the remaining spectrum can still provide a lot of information as it is mostly well above the background noise. This would be hard for a commercial AFM setup since they present a higher background noise, if subtracting its background noise, only the resonance would be left, the spectrum at low and high frequency would be lost.

We plot the PSD of the gold coated cantilever in air with its background noise being subtracted (red) : the PSD behaviors are very similar in the two spectrums, implying the $1/f$ like trend at low frequency is not related to the background electronic noise, this trend should have some link with the gold coating.

To valid this assumption, we measured PSDs of silicon (blue), gold coated (red), platinum coated (magenta) and aluminum coated (green) cantilevers with all of their background noises subtracted in air and plot the data in figure 3.5. The measurement is performed in a calcite configuration of the setup to ensure a much lower external disturbance at low frequency. PSD of the cantilevers with a metallic coating present a striking difference at low frequency comparing with the cantilever without coating : the cantilevers with gold coating, platinum coating and aluminum coating exhibit a similar $1/f$ trend that contrasts with a slightly increasing trend for silicon cantilever. The results evidently show that the $1/f$ like trend in the PSD is linked to the metallic coating rather than the contribution from the background electronic noise.

Note that an obvious difference of PSDs for these metallic coated cantilevers is the magnitude of the trend at low frequency, I will explain in section 3.4.2 that this

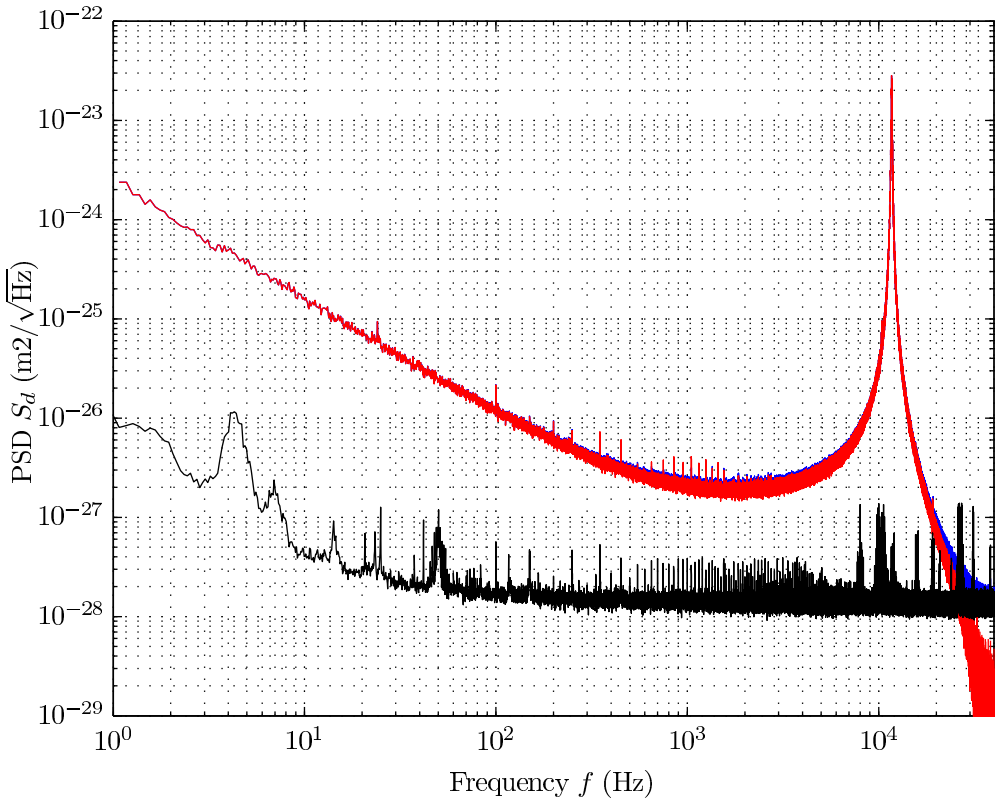

FIGURE 3.4 – Power Spectrum Density (PSD) of thermal noise induced fluctuations with (red) and without (blue) being subtracting the background noise for the Au coated cantilever at ambient pressure. Actual mechanical noise is obtained by subtracting the background noise. The black line marks the level of background noise due to the acquisition system. The $1/f$ like trends at low frequency for the two spectrums is very similar.

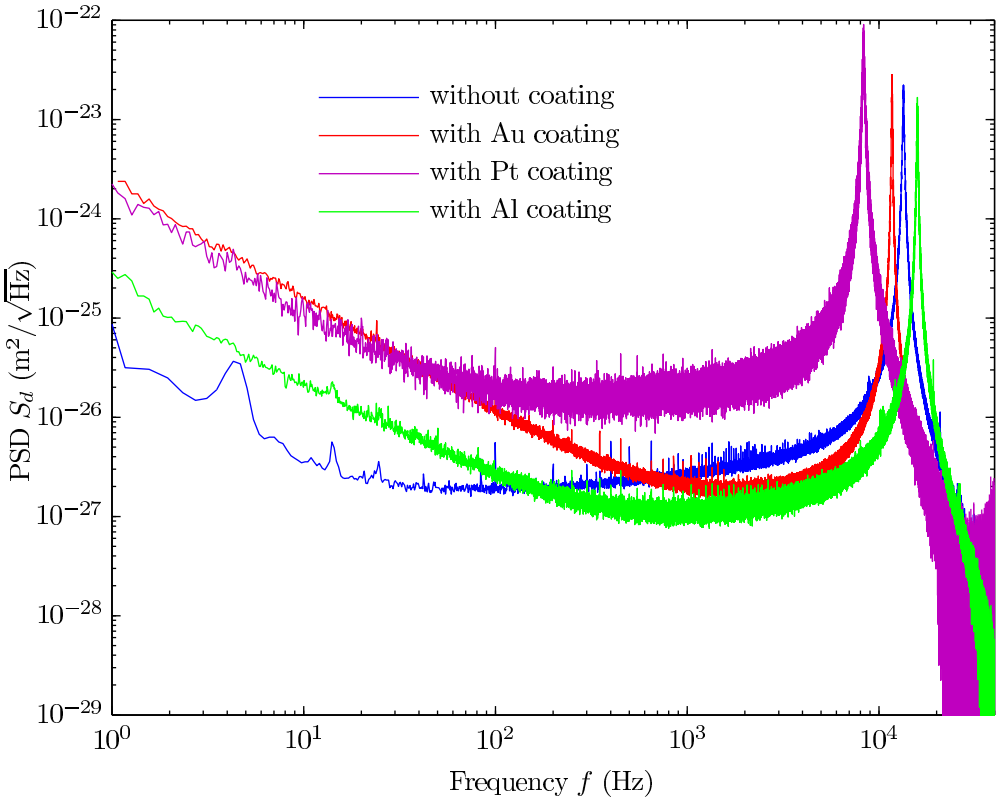

FIGURE 3.5 – Measured PSDs of silicon, gold, platinum and aluminum coated cantilevers in air. For all spectrums we have subtracted the background noise. PSDs at low frequency for cantilevers with metallic coating present clearly a $1/f$ trend while that is a slow increase trend for the silicon cantilever (without coating).

is related to the value of the viscoelastic damping in these metallic coatings. Based on these experimental observations, we know that the two models (corresponding to two dissipations) have to be taken both into account in totally describing the dissipative behavior of the cantilever.

Besides, we carefully check that the observed $1/f$ like trend is not yet due to the laser interaction with the surface of the cantilever, several reasons are listed as follows [56], I want still to mention them in order to give a clear presentation of this special trend :

(a) Frequency response function χ_{dI} of the deflexion d to the laser intensity is measured by controlling laser power I. During the measurement, the laser power is always remaining constant but some slight fluctuations might stir little movement of the beam. The PSD of the deflexion that is triggered by the fluctuation of the laser can be estimated as : $S_d^{laser} = |\chi_{dI}|S_I$, the value of which is at least 3 orders of magnitude smaller than the thermal noise triggered deflexion. It can not be the laser that leads to the $1/f$ like trend at low frequency in PSD for Au coated cantilever.

(b) If we decrease the light intensity of the laser by a factor of 10 on the coated cantilever, the shot noise grows, but it is still much lower than the measured PSD at low frequency which stays even.

(c) Some other cantilevers that are coated on one side only are measured, and except the higher background noise that is due to the bad reflectivity obtained on the uncoated side, there is no obvious difference in the $1/f$ trend.

(d) Several coated cantilevers are measured proving a reproducible characterization of $1/f$ trend.

In the section 3.2.4, we will illustrate how to access to the mechanical response function of the cantilever from the measured spectrum by Kramer-Kronig relations. This process plays a critical role in discussing the viscous damping and viscoelastic damping after.

3.2.4 From noise to mechanical response : FDT and Kramers-Kronig relations

As we presented in section 3.2.1, the AFM cantilever is modeled by a damped spring-mass system, the force acting on the tip of the cantilever and induced deflexion d are coupled variables by the Hamiltonian $\widehat{H}$ of the system, we apply the Fluctuation Dissipation Theorem (FDT) with the deflexion, the Power Spectrum Density (PSD) S_d^{SHO} of the thermal fluctuation of d is expressed by (3.5).

In the section 3.2.1, we illustrated that we computed the thermal deflexion of the cantilever for a known response function by using FTD. Now it is more interesting for us to reconstruct the response of the cantilever directly from the experimental data since our high sensitive interferometer enable a measurement of the whole spectrum on a wide frequency range.

From equation (3.5), we have :

$$\mathrm{Im}[G^{-1}(\omega)] = -\frac{\omega S_d(\frac{\omega}{2\pi})}{4k_B T} \tag{3.10}$$

The PSD that we measure is actually a direct access to the imaginary part of $G^{-1}(\omega) = d(\omega)/F(\omega)$. G^{-1} being the linear response function of deflexion d to an external force F in Fourier's space, it obeys the Kramers-Kronig relations (K-K relations) [57] :

$$\mathrm{Re}[G^{-1}(\omega)] = \frac{1}{\pi}\mathcal{PP}\int_{-\infty}^{+\infty}\frac{\mathrm{Im}[G^{-1}(\Omega)]}{\Omega-\omega}\mathrm{d}\Omega \tag{3.11}$$

$$\mathrm{Im}[G^{-1}(\omega)] = -\frac{1}{\pi}\mathcal{PP}\int_{-\infty}^{+\infty}\frac{\mathrm{Re}[G^{-1}(\Omega)]}{\Omega-\omega}\mathrm{d}\Omega \tag{3.12}$$

Hence,

$$G^{-1} = -\frac{\mathcal{PP}}{4\pi k_B T}\int_{-\infty}^{+\infty}\frac{\Omega}{\Omega-\omega}S_d(\frac{\Omega}{2\pi})d\Omega - \frac{i\omega}{4k_B T}S_d(\frac{\omega}{2\pi}) \tag{3.13}$$

where $\mathcal{PP}$ stands for the principal part of the integral. By the expression (3.11), we can compute the $\mathrm{Re}[G^{-1}(\omega)]$ from the knowledge of $\mathrm{Im}[G^{-1}(\omega)]$, and thus the full response function G can be given in the end. The approach is possible with our measured PSD due to the wide range of frequency that it covers. I would like to refer the interested readers to Appendix to find more detail of the computing process from thermal fluctuations to mechanical response.

We measure the thermal induced fluctuations of a cantilever *Budget Sensor* CONT-GB with both sides coated with a 70 nm gold coating in calcite configuration in ambient air. The spectrum spans in a wide frequency range allows us to apply Kramers-Kronig relations algorithm and reconstruct the full mechanical response function $G(\omega)$ with a few Hz resolution.

We plot in figure 3.6 and 3.7 the real part $\mathrm{Re}(G)$ and the imaginary part $\mathrm{Im}(G)$ of the reconstructed response function. $\mathrm{Re}(G)$ exhibits a characteristic parabolic shape of a harmonic oscillator as the SHO model shown in figure 3.1, the spring constant of the cantilever k can be inferred at its origin. Note that the shape of imaginary part of G in the figure 3.7 can be well comparable with Jonscher's like plus SHO model (figure 3.2) : below around 100 Hz, it follows a slowly decreasing trend, a drastic almost linearly increase trend is then observed when the frequency is above 100 Hz. In section 3.3, we will give a specific explanation for this dissipative part, it involves two dissipation sources dominating at different frequency ranges. In following sections 3.3 and 3.4, we will insight separately into the two dissipations—viscous damping and structural damping through the rebuilt response function.

3.3 Viscous dissipation

When the cantilever-composed micro mechanical system operate in a fluid, air or any other environment, the surrounding medium plays an important role in its

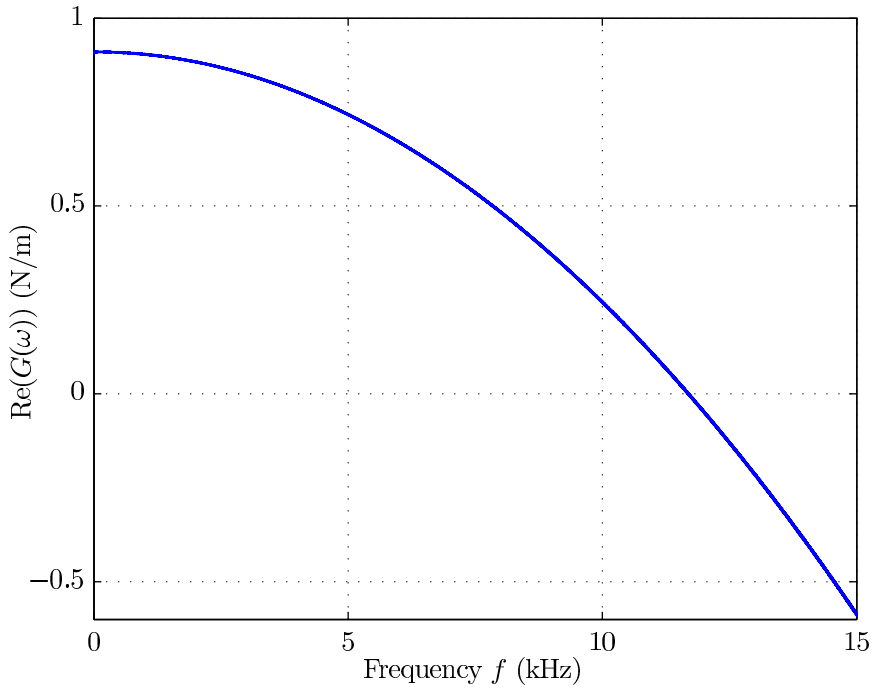

FIGURE 3.6 – Real part of mechanical response function $\mathrm{Re}(G)$ of a gold coated cantilever reconstructed from the noise spectrum of figure 3.4. The origin of the $\mathrm{Re}(G)$ can be used to infer the spring constant of the cantilever.

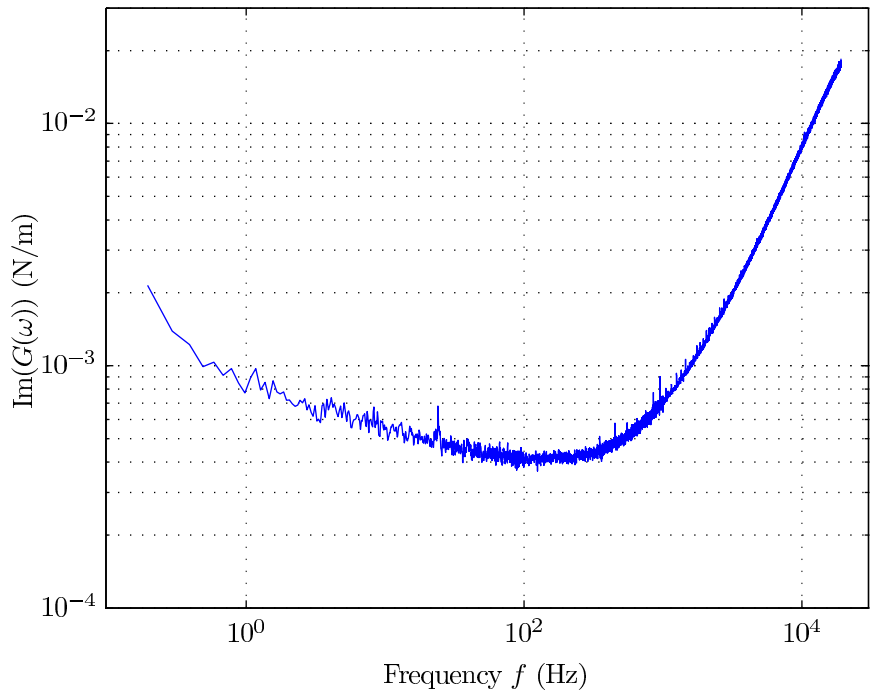

FIGURE 3.7 – Imaginary part of mechanical response function $\mathrm{Im}(G)$ of a gold coated cantilever reconstructed from the noise spectrum of figure 3.4.

mechanical behavior, as the viscous medium acts like added dynamic mass to the cantilever which can broaden and shift the resonant frequency to a lower value. To explain this behavior, a number of theoretical models [50, 58, 54, 59] have been developed to rigorously account for the effects of the surrounding medium, which in turn have been validated by detailed experimental measurements [60, 61, 62]. These works concluded that viscosity plays an essential role in the frequency response of the cantilever of microscopic size ($\sim$ 500 µm in length), as the cantilevers used in the AFM and in microelectromechanical systems (MEMS). Macroscale cantilevers($\sim$ 1 m in length) are unaffected by fluid viscosity.

I will present in the following the response of the PSD and the mechanical response function G to the change of air pressure environment P in which a cantilever is usually operated to work.

As previously presented, when the cantilever is in equilibrium at temperature T, the thermal fluctuations of its deflection d are described by the FDT, linking the PSD to the mechanical response function G of the system (equation (3.3) and (3.5)). I will show that the viscous damping of the cantilever vanishes when the air pressure decreases gradually, this corresponds to a larger quality factor Q which is read clearly on a sharper resonance of the PSD.

We use a gold (Au) coated AFM cantilever (**cAu**) with the following geometry : length 450±10 µm, width 50±10 µm, thickness 2±1 µm. We study the influence of ambient pressure P on the PSD and the mechanical response G of **cAu** : in figure 3.8 and 3.9, we plot the PSD (with the background noise being subtracted) of the deflexion for pressures from ambient to 10^{-3} mbar. It is clear that the resonance of the cantilever become sharper, implying the increase of the effective quality factor when the pressure drops. We notice here that the $1/f$ like noise for this gold coated cantilever can still be observed, indicating again that this noise is structral, it is independent of the air pressure. If the cantilever is used as a mass detector, the resolution is higher when it works in a lower pressure environment, because the resonant frequency shift triggered by the added mass can be more precisely measured than that in ambient condition.

By fitting the measured PSD of thermal induced deflexion of the cantilever by a SHO model, we get the resonant frequency as a function of air pressure, it shifts to larger values when the pressure P drops, then reaches a constant value at around 11 745 Hz, as shown in figure 3.10. This is due to a smaller effective mass of the cantilever, which means the effect brought by the air surrounding the cantilever is weakened. It saturates to a constant level when the air pressure is below 1 mbar, it gives us an evidence that the amount of mass added by air is only a small value, there is something else dissipating the vibration energy.

We can also plot the quality factor at resonance as a function of the air pressure in figure 3.11, the quality factor increase with the drop of the air pressure. It saturates also, as the resonant frequency does. Since the quality factor links to the energy loss per movement of the cantilever, and the dissipation brought by the air gets negligible in vacuum, there exists another dissipation source that accounts for the rest lost vibration energy of the cantilever in vacuum, it is named viscoelasticity

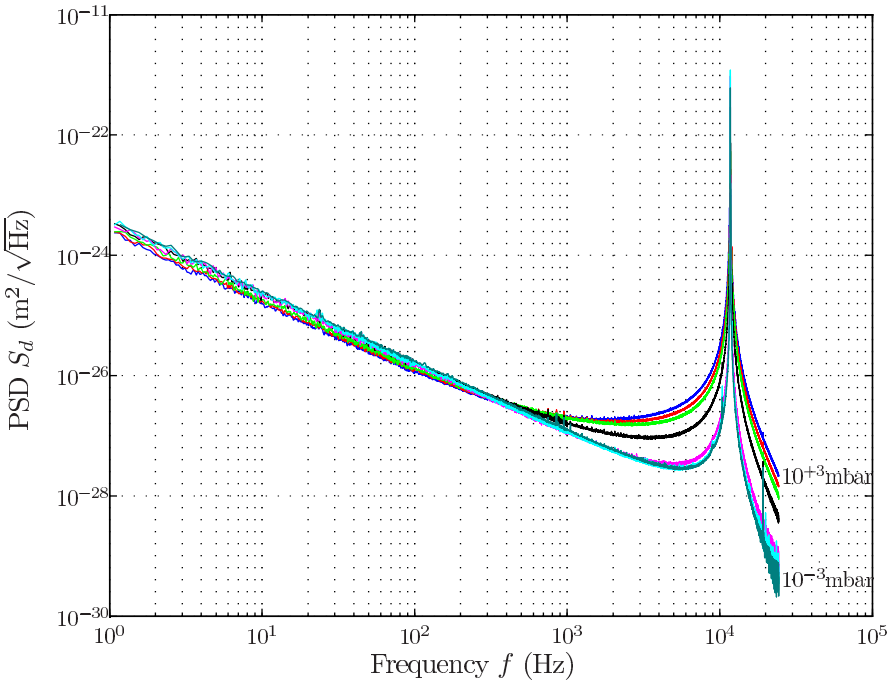

FIGURE 3.8 – Thermal noise spectrums of cantilever **cAu** at different air pressures. Background noise due to the electronics has been subtracted from the measured PSD.

(many litteratures also labeled it as structral damping), it relates to the damping inside the body of cantilever. I will present this dissipation in section 3.4.

As presented in the section 3.2.4, we rebuild the full mechanical response function G of the cantilever using Kramers-Kronig relations to probe its mechanical response behavior in frequency space. We plot the reconstructed response function (real part and imaginary part, both are normalized by spring constant k) under different air pressures in figure 3.12 and 3.13. In the figure 3.12, the additional inertia due to the air can slightly shift the parabola since the resonance frequency ω_0 is shifted. In the figure 3.13. It is clear that the dissipation is the sum of two contributions : pressure-independent internal damping $\phi(\omega)$, always dominant at low frequency and low pressure, and viscous damping term $\omega/\omega_0 Q_a$ which is only dominant at high frequency and high pressure.

For the chosen Au coated cantilever **cAu** and the frequency range probed here, viscous damping becomes negligible when the pressure is lower than 1 mbar. According to equation (3.8), the imaginary part of response function G is written as :

$$\frac{\mathrm{Im}(G)}{k} = \frac{1}{\omega_0 Q}\omega + \phi(\omega) \tag{3.14}$$

As the air pressure drops from ambient condition, the increased quality factor is leading to a lower imaginary part of response function G. As shown in figure 3.14, the red and black dotted line in the figure are the fit on the imaginary part of

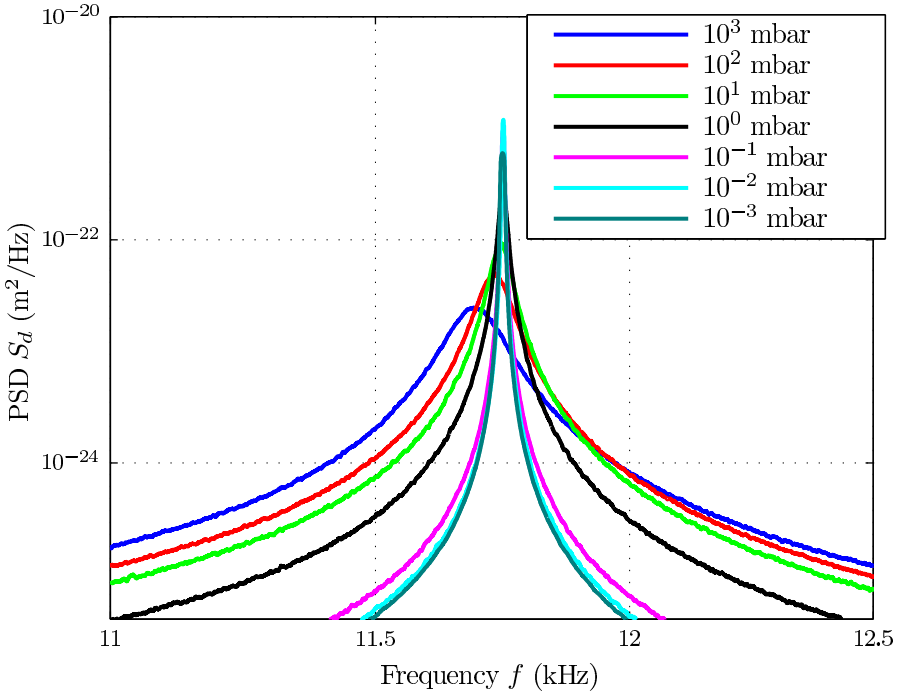

FIGURE 3.9 – Resonant peak of the spectrums as a function of air pressure. Due to the smaller mass added by the air flux surround the cantilever, the effective mass decreases leading to an increase of the resonance frequency of the cantilever. The resonant peaks become sharper which means a higher quality factor Q obtained in vacuum than in air.

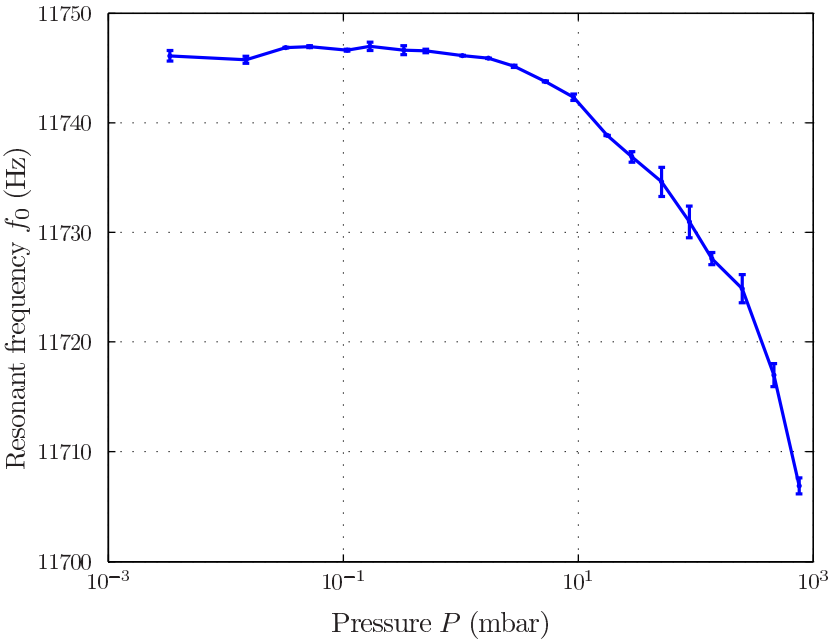

FIGURE 3.10 – The resonant frequency as a function of air pressure. It increases with the drop of air pressure and then saturates to a constant level, implying that the mass of the micro system remains constant when the pressure gets below 1 mbar.

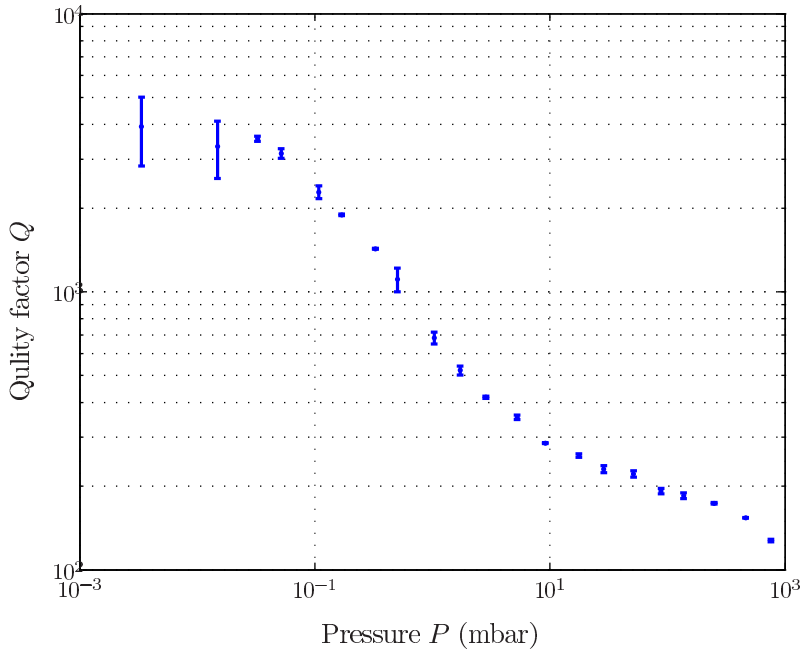

FIGURE 3.11 – Quality factor Q at resonance as a function of the air pressure. Q does not go to infinity but saturates to a constant when P goes to 0, implying another source of dissipation.

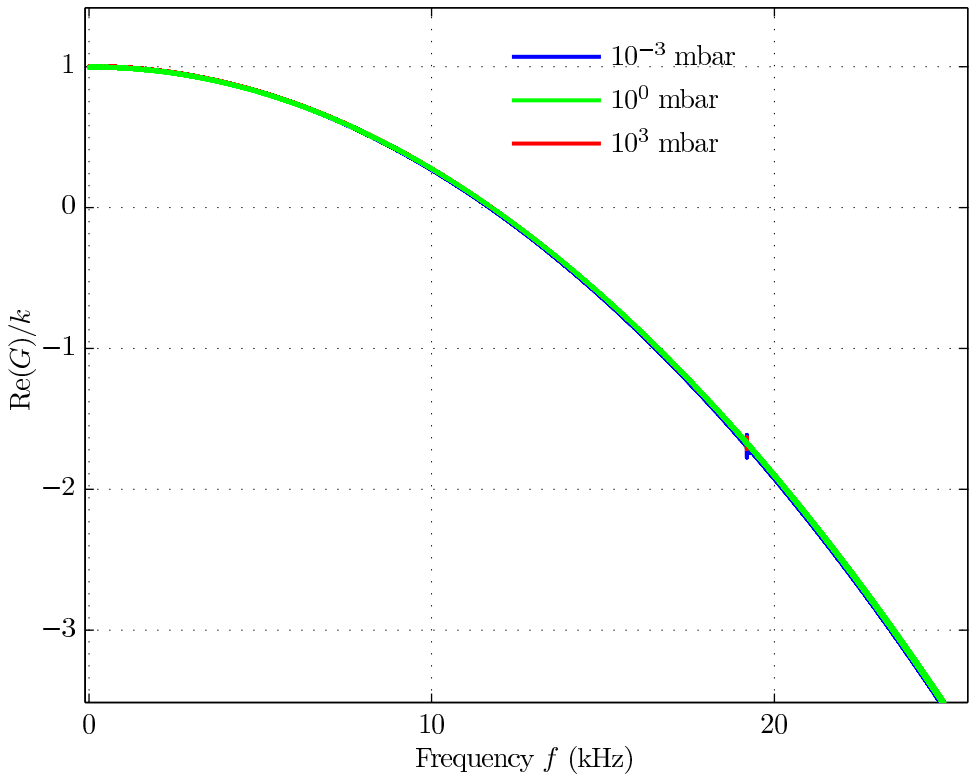

FIGURE 3.12 – Reconstructed real part of the mechanical response function of cantilever **cAu** under different air pressures. The additional inertia due to the air can slightly shift the parabola since the resonance frequency shifted. The origin keeps a constant, it is the spring constant of the cantilever k.

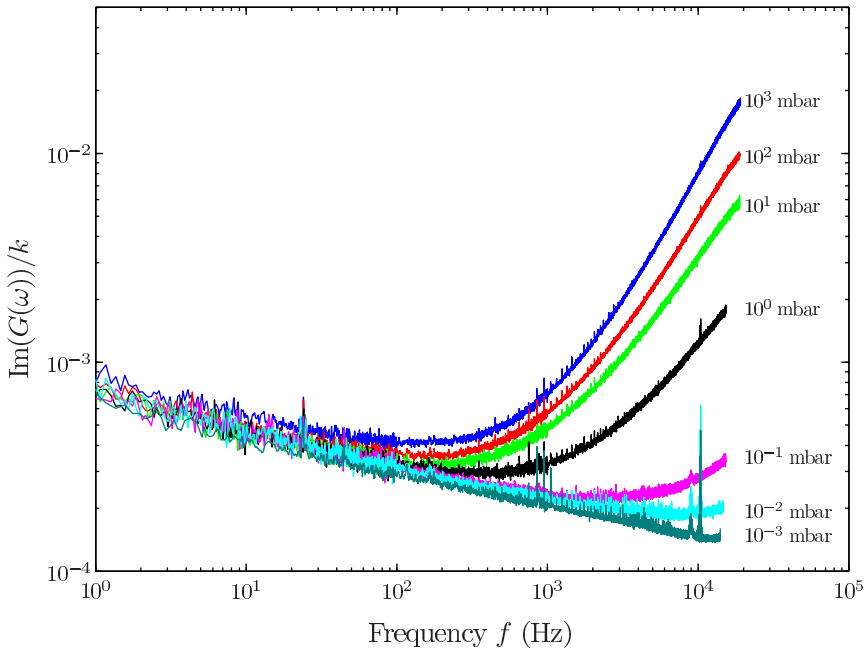

FIGURE 3.13 – Reconstructed dissipative part of the response function G of cantilever **cAu** at different air pressures. Viscous damping which always dominates at high frequency and high pressure vanishes in vacuum. The left viscoelastic damping is pressure independent, it is linked to the structure of the cantilever.

G at high (above 3 kHz) and low (below 100 Hz) frequency range. Note that the dissipative part that is below 100 Hz (black curve) presents a relatively stable trend to the decrease of the pressure while the effect due to the air (red curve) is greatly lowered. Since the dissipation that is below 100 Hz is almost one order larger than that of the dissipation from the air, it hides the latter causing a hard view of the dissipation caused by air at low frequency. That is the reason that the measurements at low and high frequency are connected by a smooth transition.

Since the dissipative part brought by the air is negligible in vacuum, one might be very interested to wonder : what is the measured damping part of G in vacuum as the effect brought by air vanishes in vacuum ? It seems also a slightly frequency dependent term in the range we are probing. Actually, this question is already answered by our previous work, this is a damping that is not linked to the air—viscoelastic damping. I will give more details about this viscoelastic damping in section 3.4.

Let us summarize the key points for this section : we control the air pressure of the environment where the micro cantilever usually works. The measured PSD and the rebuilt imaginary part are pressure dependent. The air flow surrounding the cantilever add a additional mass which lead the resonant frequency of the spectrum being smaller than that in vacuum. With air pressure drops, a sharper resonant peak is observed, indicating a more precise measurement can be obtained when the cantilever is used as an oscillator. Quality factor Q increases with the drop of P

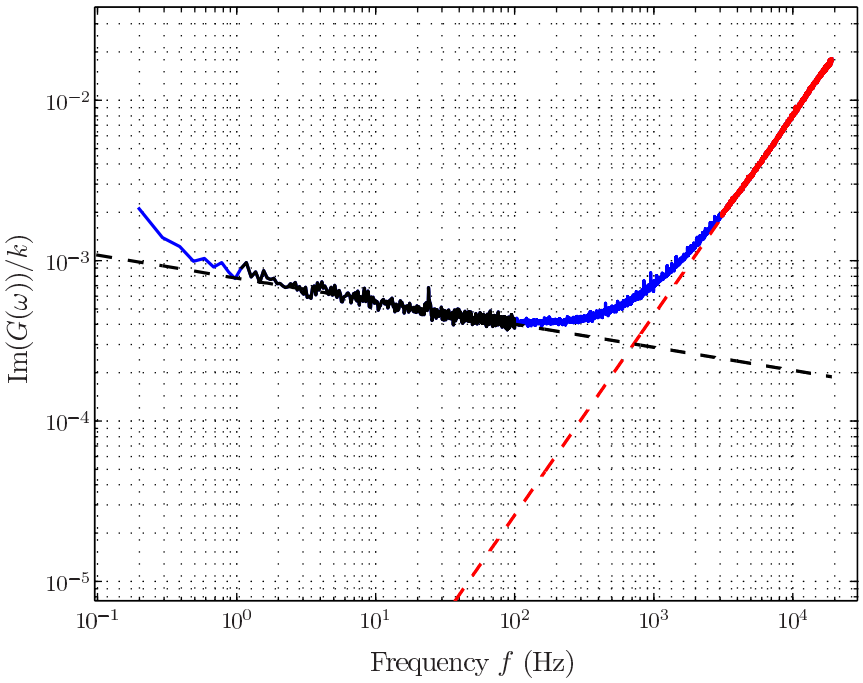

FIGURE 3.14 – Reconstructed dissipative part of the response function of the cantilever **cAu** in air. The dissipation is clearly the sum of the two sources : the viscous damping (red curve) dominates mostly above the frequency $f = 100\,\mathrm{Hz}$ and at high pressure, the internal damping (black curve) dominates at low frequency mostly below $f = 100\,\mathrm{Hz}$ and at low pressure. Red and black dotted line in the figure are the fits on these two kind of dampings.

Cantilever	Commercial type	Adhesion layer	Initial coating	Additional gold coating
cAu	Budget Sensors (ContGB)	2 × 5nm Cr	2 × 70nm Au	-
cPt	Nanoworld POINTPROBE (ContPt-50)	2 × 5nm Cr	2 × 23nm PtIr	-
cAl	Budget Sensors (BS-ContAl)	2 × 5nm Cr	1 × 30nm Al	-
dAu	Budget Sensors (ContGB)	2 × 5nm Cr	2 × 70nm Au	10nm+10nm+...
dPt	Nanoworld POINTPROBE (ContPt-50)	2 × 5nm Cr	2 × 23nm PtIr	10nm+10nm+...
dSi	Budget Sensors (All In One-TL)	1 × 2nm Cr	-	10nm+10nm+...

TABLE 3.1 – Sets of cantilevers characterized in the experiments. For cantilevers where we performed additional gold depositions, layer thickness increments were around 10 nm for the first 3 evaporations, then around 20 nm.

and then saturates when P is below 1 mbar, that means less energy is being lost per cycle of vibration, but implying at the same time another source of dissipation.

The rebuilt dissipative part is composed of two sources : viscous damping term $\omega/\omega_0 Q$ that always dominates at high frequency and high pressure, but vanishes when the pressure drops, and the pressure-independent viscoelastic damping $\phi(\omega)$ term that always dominates at low frequency or low pressure. The viscous damping due to the air flow around the cantilever is largely lowered when the pressure is decreased, it is the left viscoelastic damping that contributes to the main dissipation in vacuum, it is a slightly frequency dependent term.

3.4 Viscoelastic damping of metallic coating

As presented in section 3.3, when the air pressure drops, the viscous damping brought by air vanishes, leaving only the viscoelastic damping described generally by $\phi(\omega)$, it is related to the structural of the cantilever. Several models might be account for this internal dissipation : clamping and support losses, viscoelasticity, surface losses, thermoelastic dissipation (TED), etc. I will present first in this section that this internal damping is not only frequency dependent but also material dependent. After a quick discussion of the possible dissipation source listed above, I will show the exploration of the origin of viscoelasticity : it does not come from the interface between the metal layer and the surface of the cantilever, but from the bulk of the coating.

3.4.1 Material dependence

We present here characteristic datas corresponding to three kinds of AFM cantilevers **cAu**, **cPt**, **cAl** (around 10 samples were measured for each type). Their physical properties are summarized in table 3.1. In addition, we performed successive gold layer deposition on three other types of cantilever **dAu**, **dPt**, and **dSi**, their parameters are also detailed in the table 3.1. The increment of Au layer thickness were around 10 nm for the first 3 evaporations, then around 20 nm for the next depositions. Cantilever **dSi** is initially a raw silicon cantilever, prepared with a 2 nm Cr adhesion layer before the Au coating, its initial internal friction is too small to be measured with our precision.

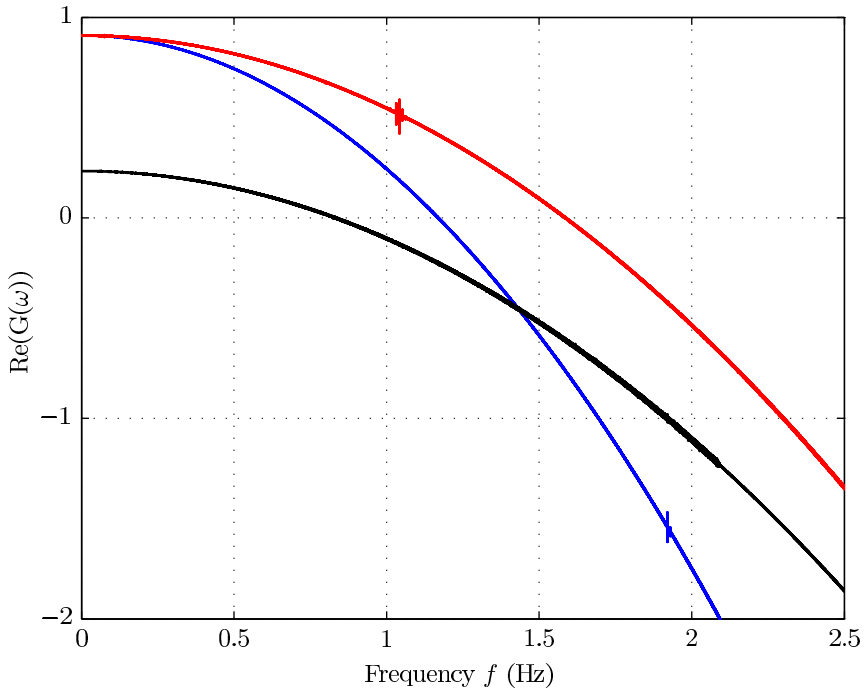

FIGURE 3.15 – Real part of response function G for the cantilever **cAu**, **cPt** and **cAl**, the stiffness of the cantilever can be estimated at its origin : $k(1-\omega^2/\omega_0^2) \to k$, when $\omega \to 0$, k_{Au} =0.92 N/m, k_{Al} =0.9 N/m, k_{Pt} =0.23 N/m.

We measure the PSD of thermal induced fluctuations of these cantilevers in vacuum, and reconstruct the response function G by Kramers-Kronig relations. We plot in figure 3.15 the real part of G. At the origin, when $\omega \to 0$, $\mathrm{Re}(G(\omega))$ gives the spring constant k of the oscillator : $k(1-\omega^2/\omega_0^2) \to k$. We measure this way $k_{\mathrm{Au}} = 0.92\,\mathrm{N/m}$, $k_{\mathrm{Al}} = 0.9\,\mathrm{N/m}$, $k_{\mathrm{Pt}} = 0.23\,\mathrm{N/m}$.

We plot the imaginary part of the response function G normalized by k : $\mathrm{Im}(G(\omega))$
$/k = \phi(\omega)$, hence the viscoelasticity for the three cantilevers in figure 3.16. The magnitude of the internal dissipation is a little smaller for the cantilever **cPt** and **cAl** than for **cAu**, but a similar weak frequency dependence is found. A simple power law with a small exponent is established to describe the viscoelasticity, it matches well the observed frequency dependence for the Au coated cantilever with $\alpha_{\mathrm{Au}} \approx -0.15$.

As shown in the figure, the viscous damping effect can still be observable for the cantilever **cPt** at high frequency (above 1 kHz) at the lowest pressure we can achieve in our system (10^{-3} mbar). If we restrict the frequency to the range 1 Hz − 1 kHz, a similar power law dependance with an exponent $\alpha_{\mathrm{Pt}} \approx -0.12$ can be observed for the cantilever **cPt**. The same data for the cantilever **cAl** however is a little different with the others, it is a flat dependance with the frequency, giving a $\alpha_{\mathrm{Al}} \approx 0$. By consequence, the power law dependence works generically, though

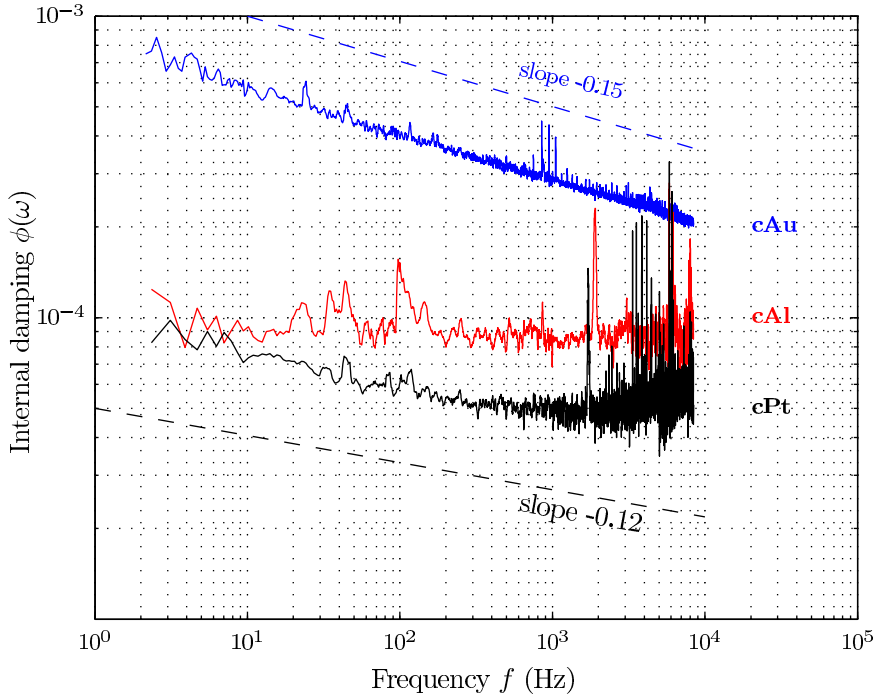

FIGURE 3.16 – Internal damping $\phi(\omega)$ of cantilevers **cAu**, **cAl** and **cPt** reconstructed from the noise spectrums measured in vacuum. Each of them follows a simple power law frequency dependance ω^α with a small exponent α.

the small exponent exhibits slightly differences for different probes. The different exponent α shows that the internal damping $\phi(\omega)$ is a material dependent variable. Cantilevers with any metallic coating can be measured by this method so as to give possible suggestion of obtaining the lowest dissipation when these cantilevers are being used.

3.4.2 The origin of viscoelasticity

To understand the mechanism of this internal dissipation, let us discuss the contribution of the possible main dissipative sources, since the viscous damping by the air has been probed and is negligible in vacuum, the remaining possible sources are :

$$\phi = \phi_{\text{clamping}} + \phi_{\text{support}} + \phi_{\text{TED}} + \phi_{\text{internal}} + \phi_{\text{coating}} + \phi_{\text{surface}} \tag{3.15}$$

where each term in this sum corresponds to clamping and support losses, thermal elastic dissipation (TED), other source of internal dissipation inside the bulk of cantilever (internal friction or viscoelasticity), dissipation inside the bulk of the coating, and all surfaces and interfaces contributions to damping, respectively.

- ϕ_{clamping} : the cantilever and its chip are fabricated in a monolithic design, the clamping loss can thus be largely minimized. The related dissipation can be estimated by equation $\phi_{\text{clamping}} \sim (h/l)^3$ [51], where l and h are the length and the

thickness of the cantilever. In geometry of our used cantilever here, $l = 450\,\mu m$, $h = 2\,\mu m$, the computed loss is of the order of 10^{-7}, and is thus be negligible.

- ϕ_{support} : thanks to our well-designed cantilever holder, the support loss is also negligible. As simple illustration of this fact, the total dissipation of a raw silicon cantilever in vacuum is not measurable outside resonance, with an upper bound around 10^{-5}.
- ϕ_{TED} : for a silicon cantilever, thermoelastic damping can be estimated by [63] :

$$\phi_{\text{TED}} = \frac{E\beta^2 T}{C}\frac{\Omega}{1+\Omega^2} \tag{3.16}$$

where E =169 GPa is Young's modulus of silicon, β =$2.6 \times 10^{-6}\,K^{-1}$ is linear coefficient of thermal expansion, C =$2.6 \times 10^6\,J{\cdot}m^{-3}K^{-1}$ its specific heat per unit volume and Ω the normalized frequency defined as :

$$\Omega = \omega\frac{Ch^2}{\pi^2\lambda} \tag{3.17}$$

where $\lambda = 149\,W{\cdot}m^{-1}K^{-1}$ is the thermal conductivity. In our case, h =2 µm, $\omega = 2\pi f$ <2×10^5 rad/s, leading to $\phi_{\text{TED}} < 10^{-6}$, below our precision level. Using values from [64], we checked that the change in TED due to metallization was also not meaningful in our experiment.

- ϕ_{internal} : we use commercially available high-quality mono crystal silicon cantilevers, thus the bulk loss (internal friction) caused by the motion of crystallographic defects is negligible. Again, as a simple illustration of this fact, the total dissipation of a raw silicon cantilever in vacuum is not measurable outside resonance, with an upper bound around 10^{-5}.
- ϕ_{coating} : this contribution corresponds to the internal dissipation in the bulk of the coating, and is estimated by [39, 65] :

$$\phi_{\text{coating}} = 3\frac{E_c}{E}\frac{h_c}{h}\phi_c \tag{3.18}$$

where E_c, ϕ_c and h_c are bulk Young's modulus, bulk viscoelasticity and thickness of the coating layer (index c). This contribution is thus proportional to the layer thickness h_c.

- ϕ_{surface} : this last contribution accounts for the process of dissipation that may occur at the surface of the cantilever and the interfaces between the silicon cantilever and the various coating layers. By definition, this terms should be independent of the thickness of the coating layer.

Within our experimental precision, all terms in the sum of equation (3.15) are negligible except the last two ones, so the total dissipation in vacuum is :

$$\phi = \phi_{\text{surface}} + 3\frac{E_c}{E}\frac{h_c}{h}\phi_c \tag{3.19}$$

To investigate the origin of this internal dissipation, we measured $\phi(\omega)$ for cantilevers **dSi**, **dPt** and **dAu** as a function of the thickness h_c of an added gold coating : the same 3 cantilevers were characterized in vacuum between the deposition of successive coatings, we plot the results in figure 3.17 the value of $\phi(\omega)$ between 100 Hz and 200 Hz at low frequency and the value of $1/Q_{\text{eff}}$ which is derived from a lorenzian fit of the resonance. As the figure clearly shows, the internal dissipation is roughly proportional to the thickness of gold coating, and remains weakly frequency dependent in these observations. This behavior suggests that the main contribution to the internal damping of the cantilever originates in the bulk of the gold coating, rather than from a surface or interface (between the coating and the surface of cantilever) effect. Indeed, if it is the surface or interface effect that dominates, the internal dissipation would be exist even for the lowest thickness of coating. In the experiment, however, we obtain a smaller value of dissipation with thinner coating, which validates the hypothesis about the origin of the damping. Moreover, we carefully check the effect that might be brought by the adhesion layer of Cr, we measured the cantilevers without coating but the Cr layer and the cantilever coated by 23 nm Au coating, we get the same result from the data, indicating that the adhesion layer add nothing or very tiny damping to the cantilever which can be neglected from the data.

As shown in the figure 3.17, total dissipation in the case of gold coating is simply proportional to the thickness h_c, thus $\phi_{surface}$ is negligible in our experiment. The dissipation that we measure is therefore solely due to the viscoelastic properties of the bulk of the coating, and proportional to coating thickness h_c.

Using manufacturer values for the thickness of metallic layers of cantilevers **cAu**, **cAl** and **cPt**, we can thus extract the viscoelasticity ϕ_c of each coating from the measurement of the total dissipation ϕ, and plot the result in the figure 3.18. $PtIr_5$ is the least dissipative material, with a damping about an order of magnitude lower than gold and aluminum. Those two last materials have similar viscoelasticity, aluminum being better at low frequency (below$\sim$50 Hz) and worse above. Obviously these internal dampings within coatings still follow the same simple power law as described before. The results agree reasonably with the work of Sosale and collaborators [65] in the smaller frequency range probed in their experiments on gold and aluminum.

3.5 Summary

We record the power spectrum density (PSD) of thermal induced fluctuations of the cantilever. Thanks to our highly sensitive interferometer and low background noise level, the spectrum spans on a wide frequency range from 2 Hz to 2×10^4 Hz which is far beyond the capability for commercial AFM setup. By such, we get a full view on the behaviors of the spectrum : in vacuum, the trends of the cantilever of silicon and gold coated are clearly different, slowly increasing spectrum for silicon cantilever and a $1/f$ like trend for the gold coated one. This special trend is seen as

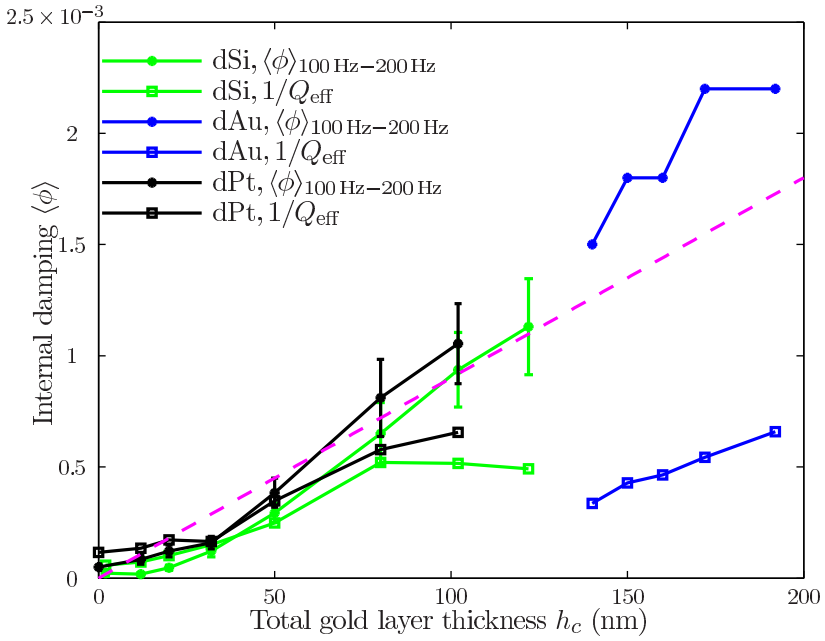

FIGURE 3.17 – Internal damping at low and high frequency (average of $\phi(\omega)$ around 150 Hz and $1/Q_{\mathrm{eff}}$ at resonance) as a function of the total gold layer thickness for cantilever **dSi**, **dAu** and **dPt**. The internal damping is clearly proportional to the thickness of the gold coating, giving evidence about the origin of this damping being the bulk rather than the interface. Typical error bars are shown for two cantilevers. The dashed line corresponds to a linear dependance of ϕ in gold thickness h_c, expected if the viscoelasticity of the coating is the only relevant damping process.

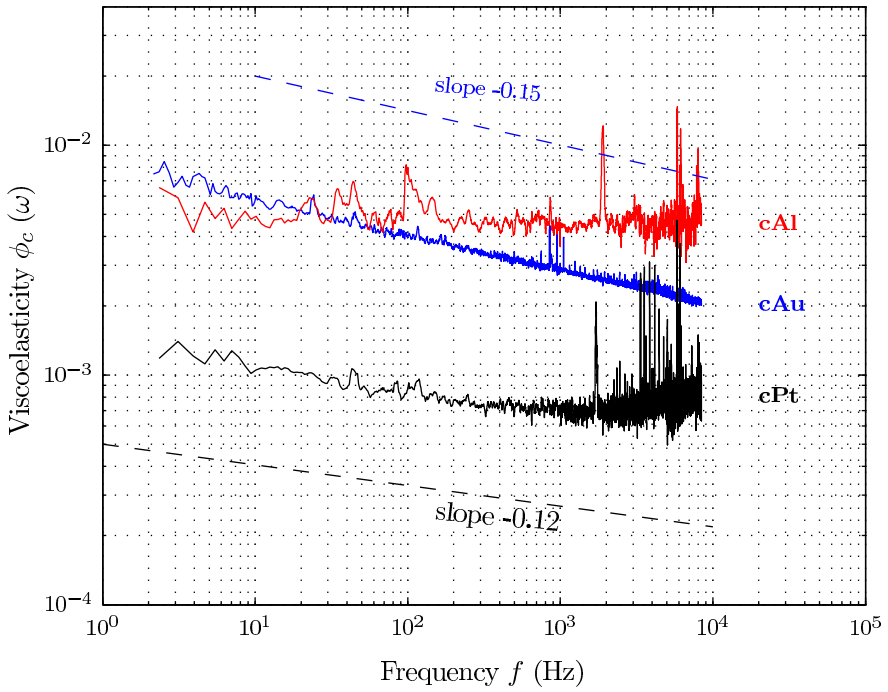

FIGURE 3.18 – Intrinsic viscoelasticity ϕ_c of gold, aluminum and PtIr5 coatings (corresponding to cantilevers **cAu**, **cAl**and **cPt**) as a function of frequency.

the signature of the internal damping of the cantilever. The as used SHO model is too simple for us to describe the cantilever with a metal coating.

To go further, using Fluctuation-Dissipation Theorem (FDT) and the Kramers-Kronig relations, we can rebuild the response function G of the cantilever from the measured PSD, any modification of the cantilever can be directly reflected on the response function. The $1/f$ like trend is related to the internal damping of the cantilever—viscoelasticity. By decreasing the air pressure in which the cantilever is working, we restrict only our focus on the viscoelastic damping since the viscous effect from the air is largely limited.

The derived viscoelastic damping $\phi(\omega)$ presents a material and frequency dependence. A simple power law ω^α with a small exponent α is used to characterize the damping up to 4 decades in frequency. We compute the viscoelasticity as a function of gold coating with various thicknesses, we find that a linear relation of viscoelasticity with respect to the thickness. After discussing various possible damping mechanism that have been proposed up to date, we attribut the origin of this damping to the bulk of the coating rather than to interface or surface effects.

The results fully unveil the dissipation process to us, it shows that the choice of the coating material is critical with respect to internal dissipation in micro-cantilevers, the commonly commercial used gold coating is not the best choice according to this criterion, if it is the material that can not be replaced in chemical requirements, using the smallest thickness of gold is a wise way to largely minimize

the damping. Our characterization procedure features an excellent resolution with measurement of overall mechanical loss tangents down to 10^{-4}. This way, the viscoelasticity due to the coating can be accurately quantified and our measurements should be useful in the perspective of testing models of internal friction, eventually leading to improved coating procedures and better performance of cantilever based sensors.

Chapitre 4

From adhesion force to intrinsic property of nanotubes

Contents

4.1 Introduction

4.1.1 Carbon nanotubes (CNTs)

Ever since their discovery [66], carbon nanotubes have been recognized as particularly important nanoscopic material. Carbon nanotubes (CNTs) are allotropes of carbon with a cylindrical nanostructure. They have been constructed with length-to-diameter ratio of up to $10^8 : 1$ [67], significantly larger than any other material. The cylindrical carbon nanotube is widely investigated in nanotechnology, electronics, optics and other fields of material science and technology due to its unique properties. In particular, owing to their extraordinary thermal conductivity and mechanical and electrical properties, carbon nanotubes are used as additives to various structural materials. For instance, nanotubes are included in the material of some baseball bats, golf clubs, or car parts, etc.

Nanotubes are members of the fullerene structural family. Its name is derived from the long, hollow structure with one-atom-thick wall formed by carbon atoms, also called graphene. These sheets are rolled at specific and discrete ("chiral") angles, the structure of carbon nanotubes is described in terms of the tube chirality, which

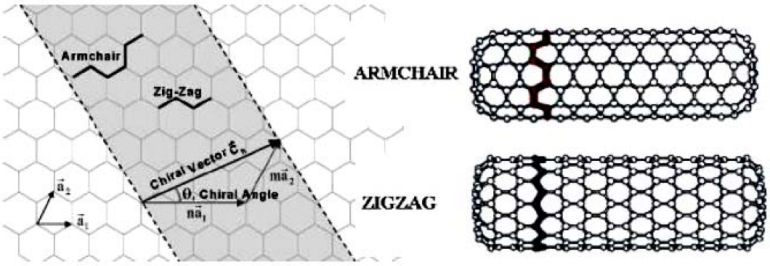

FIGURE 4.1 – By rolling a graphene sheet in different directions typical nanotubes can be obtained : zigzag $(n, 0)$, armchair (m, m), and chiral (n, m), where $n > m > 0$ [68]. Integers (n, m) are the numbers of steps along which the zigzag carbon bonds of the hexagonal lattice, $\vec{a}_1$ and $\vec{a}_2$ are unit vectors, $\vec{C}_h$ is the chiral vector, and Θ is the chiral angle (see equation 4.1)

is defined by the chiral vector $\vec{C}_h$ and the chiral angle Θ, these parameters determine that the individual nanotube has a metal or semiconductor property. As shown in figure 4.1. The chiral vector indicates the way, in which graphene is rolled-up to form a nanotube.

$$\mathbf{C_h} = n\mathbf{a}_1 + m\mathbf{a}_2 \tag{4.1}$$

Where the integers (n, m) correspond the number of steps along the zigzag carbon bonds of the hexagonal lattice, $\mathbf{a}_1$ and $\mathbf{a}_2$ are unit vectors. The electronic property of the CNT deeply depends on the chirality.

There are usually two kinds of CNTs, Singlewall carbon nanotube (SWCNT) and Multiwall carbon nanotube (MWCNT), defined by the structure of the walls (concentric cylinders) and its diameters. MWCNT is often with both of its ends capped, and its diameter is in the range from several nanometers up to 200 nm, SWNT diameters are varied from 0.5 nm to 5 nm.

4.1.2 Synthesis of CNT

The MWNTs were first discovered in the soot of the arc-discharge method by Iijima [66]. This method has been used for a long time before the production of carbon fibers and fullerenes. It cost 2 years for Iijima and coworkers [69], and also Bethune et al [70] to synthesize SWNTs by using metal catalysts in the arc-discharge method in 1993. A significant progress was made by laser-ablation synthesis of bundles of aligned SWNTs with small diameter distribution by Smalley and co-workers [71]. Catalytic growth of nanotubes by the chemical vapor decomposition (CVD) method that is still widely used up to now was first introduced by Yacaman et al [72]. In the following part, we will briefly outline these three major synthesis methods of CNTs.

4.1.2.1 Arc-discharge method

Arc-discharge for the growth of nanotubes have been widely used in the past decades, it has been first introduced by Iijima, it involves the condensation of carbon atoms generated from evaporation of solid carbon sources which is similar to that used for the fullerene synthesis. The temperatures needed in the evaporation are close to the melting temperature of graphite, $3000 - 4000°C$. As shown in the scheme 4.2 (a), carbon needles ranging from 4 to 30 nm in diameter and up to 1 µm in length were grown on the negative carbon electrode due to the plasma of argon gas ignited by high currents passing through opposing carbon anode and cathode in a chanel filled with argon (Ar) (100 Torr). Transmission electron microscopy (TEM) revealed that the needle comprised 2 to about 50 coaxial tubes of graphitic sheets, this is what we called later multi-walled carbon nanotubes. Helical formation was formed by carbon atoms hexagons on each tube. The helical pitch presents different for different needles and also from tube to tube for a single needle. The tips of the needles were usually closed by a curved, polygonal, or a cone-shaped caps.

Arc-discharge has been developed into an excellent method for producing both high quality multiwall nanotubes and singlewall nanotubes. MWNTs can be obtained by controlling the growth conditions such as the pressure of inert gas in the discharge chamber and the arcing current. In 1992, a breakthrough in MWNT growth by arc-discharge was first made by Ebbesen and Ajayan who achieved growth and purification of high quality MWNTs at the gram level [73]. This provides a possible opportunity to industrial production of the CNTs.

For the growth of singlewall carbon nanotubes, a metal catalyst is used in the arc-discharge method. The first success in producing substantial amounts of SWNTs by arc-discharge was made by Bethune and coworkers in 1993 [70]. Large-scale synthesis of MWNTs by a variant of the standard arc-discharge technique was reported by Ebbesen and Ajayan [73]. In 1993, Iijima [69] and Bethune [70] almost reported at the same time the arc-discharge and catalyst-assisted synthesis of SWNTs. Iijima use arc-discharge chamber filled with a gas mixture of 10 Torr methane and 40 Torr argon. Two electrodes were installed in the center of the chamber, the lower one—cathode had a shallow dip to hold a small piece of iron during the evaporation. Between the installed two electrodes, a DC current of 200 A was applied to perform the arc-discharge. The relative ratio of the used components—argon, iron and the methane play an important role in the synthesis process.

Large quantities of SWNTs were produced by arc-discharge method by Journet and co-workers [74]. The similarity of yield CNT in this method and that of Thess [71] lead to the conclusion of CNT growth mechanism : it does not depends on the varied experimental condition but on the kinetics of carbon condensation in a non-equilibrium situation.

4.1.2.2 Laser-ablation method

The growth of high quality SWNTs at several gram scale was achieved by Smalley and coworkers by a laser ablation method [71], as illustrated in figure 4.2 (b).

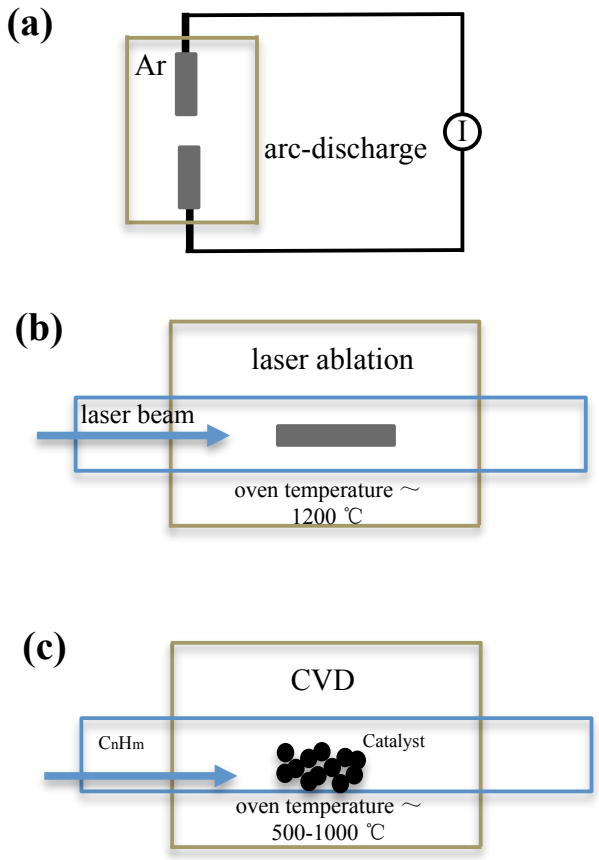

FIGURE 4.2 – CNT synthesis : Arc-discharge (a), laser-ablation (b) and catalytic growth scheme (c). (a) Two graphite electrodes are used to produce arc by DC current in inert gas in the arc-discharge method. (b) Laser beam vaporizes the target of a mixture of graphite and metal catalyst in a tube in a atmosphere with flowing inert gas at $\sim$ 1200°C, the synthesised CNTs are collected in a container outside the furnace. (c) In the catalytic method, hydrocarbon gas is chemically decomposed assisted by a transition metal catalyst in a quartz tube to produce CNTs at a temperature of 550-750°C

The method used intense laser pulses to ablate a carbon target containing 0.5 atomic percent of Ni and Co. The target was placed in a tube-furnace heated to 1200°C. During laser ablation, a flow of inert gas was passed through the growth chamber to carry the grown natures downstream to be collected on a cold finger. The produced SWNTs are mostly in the form of ropes consisting of tens of individual nanotubes close-packed into hexagonal crystals via van der Waals interactions. The optimization of SWNTs growth by laser-ablation was achieved by Journet and coworkers using a carbon anode containing 1.0 atomic percentage of Yttrium and 4.2 at. % of Ni as catalyst [74].

In the method of arc-discharge and laser ablation, typical by-products include fullerenes, graphitic polyhedrons with enclosed metal particles, and amorphous carbon in the form of particles or overcoating on the sidewalls of nanotubes. A purification process for SWNT materials has been introduced by Smalley and coworkers [75] and is now widely accepted by researchers. The method involves refluxing the as-grown SWNTs in nitric acid solution for an extended period of time, oxidizing away amorphous carbon species and removing some of the metal catalyst species. The success in producing high quality SWNT materials by laser-ablation and arc-discharge has led to wide availability of samples useful for studying fundamental physics in low dimensional materials and exploring their applications.

For the two growth methods, arc-discharge and laser-ablation, the arc-discharge is a much cheaper way to produce CNT than the laser-ablation.

4.1.2.3 Chemical Vapor Deposition method

Chemical vapor deposition (CVD) methods have been successful in making carbon fiber, filament and nanotube materials since more than 10-20 years ago [76, 77, 78, 79, 80, 81, 82, 83, 84]. A schematic experimental setup for CVD growth is indicated in figure 4.2 (c). The growth process involves heating a catalyst material to high temperatures in a tube furnace and flowing a hydrocarbon gas through the tube for a period time of reaction. Materials that grow over the catalyst are collected by cooling the system to room temperature. The key parameters in CVD method are the hydrocarbons, catalysts and growth temperature.

The active catalytic species are typically transition-metal nanoparticles that are formed on a support material such as alumina. The general mechanism of CNT growth (see figure 4.3) in a CVD process involves the dissociation of hydrocarbon molecules catalyzed by the transition metal, and dissolution and saturation of carbon atoms in the metal nanoparticle. The precipitation of carbon from the saturated metal particle leads to the formation of tubular carbon solids in sp^2 structure. Tubule formation is favored over other forms of carbon such as graphitic sheets with open edges. This is because a tube contains no dangling bonds and therefore is in a low energy form. For MWNT growth, most of the CVD methods employ ethylene or acetylene as the carbon feedstock and the growth temperature is typically in the range of $550 - 750$°C. Iron, nickel or cobalt nanoparticles are often used as catalyst. The rationale for choosing these metals as catalyst for CVD growth of nanotubes

lies in the phase diagrams for the metals and carbon. At high temperatures, carbon has finite solubility in these metals, which leads to the formation of metal-carbon solutions and therefore the aforementioned growth mechanism. Noticeably, iron, cobalt and nickel are also the favored catalytic metals used in laser ablation and arc-discharge. This simple fact may hint that the laser, discharge and CVD growth methods may share a common nanotube growth mechanism, although very different approaches are used to provide carbon feedstock.

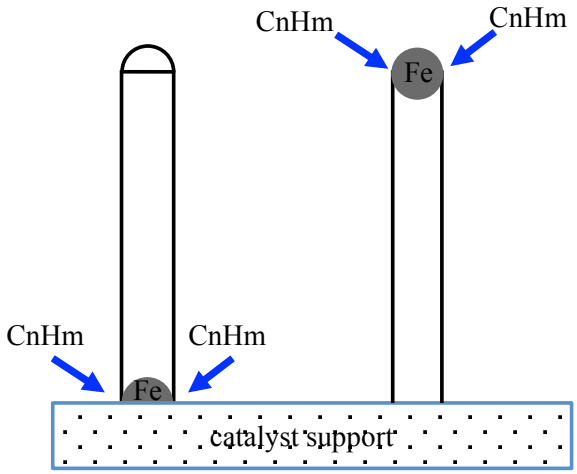

FIGURE 4.3 – Two general growth modes of nanotube in chemical vapor deposition. Left diagram : base growth mode. Right diagram : tip growth mode.

A major pitfall for CVD grown MWNTs has been the high defect densities in their structures. The defective nature of CVD grown MWNTs remains to be thoroughly understood, but is most likely be due to the relatively low growth temperature, which does not provide sufficient thermal energy to anneal nanotubes into perfectly crystalline structures. Growing perfect MWNTs by CVD remains a challenge to this day.

Since the synthesis of nanotubes with small diameters $\sim 1.4\,\text{nm}$ requires catalyst and it is necessary to clarify the role of the catalyst in the growth of nanotube. There are two possible explanations for the growth : the first mechanism of catalyst-assisted tip-growth assumes that the metal atoms sit on the open edge of precursor fullerene clusters [71]. The metals atoms scoot around the open edge of the cluster preventing the formation of carbon pentagons and the dome closure. The metal atom locally inhibits the formation of pentagons that would initiate dome closure. Additionally, the metal catalyst assists incoming carbon atoms in the formation of hexagons and thus in the lengthening of the tube. This mechanism is consistent with the experimental observation that no metal particle could be found on the grown tubes [71]. Another possible mechanism is the catalyst-assisted base growth of SWNTs. It was suggested that the nanoparticles, often with dangling bonds, could catalyze the growth of SWNTs by adding carbon atoms to the tubes. Molecular-

dynamics and total-energy calculations using a realistic three-body potential for carbon were carried out in order to clarkfy the base growth mechanism [85]. It was found that nanometer sized protrusions on the nanoparticle surface lead to nucleation of very narrow tubes.

4.1.3 Adhesion property of SWCNT

Single wall carbon nanotubes (SWNTs), are well known by its extraordinary mechanical, electrical, thermal, and chemical properties [86, 87, 68, 88, 89, 90], and provide tremendous potential for development of many applications such as composite material [91, 92], components of nanoscale electronics [93, 94, 95], mechanics and sensors [92, 96]. Whatever exceptional their intrinsic properties may be, SWNTs need to interact with the environment where they are to be useful.

The diameter of SWNTs varies from 0.5 nm to 5 nm, owing to the high aspect ratio, SWNTs grown from traditional methods (outlined in section 4.1.2) are typically in the form of bundle nanotubes rather than individual one. It is the van der Waals interactions between each carbon atoms that leads to such strong adhesion inside SWNTs bundle. The van de Waals forces thus play a critical role in the properties of SWNT at nanoscale and can dominate strongly the performance of the nano-devices that is partly composed of SWNT.

In practical cases, SWNT can stick easily on surfaces, which presents a problem when they are used as shafts, pillars, or any other suspended mechanical uses [97] : they can loose their functionality if sticking occurs when the SWNT somehow get too close to a surface. On the contrary, Kis and co-workers [98] created for example, a rigid clamping or good electrical contact using this strong adhesion of SWNTs. Therefore, beyond these physical properties they own, understanding the mechanism of the adhesion behavior of SWNT and more generally of other nano wires and nanoscopic object is also of great importance not only to the separation of bundled SWNTs but also to those nano implementations where the adhesional interaction might dominates the performance. For instance, for carbon-nanotube-based nano switches [99, 100] and nanotweezers [101, 102], the adhesion is an important parameter to be taken into account.

Several investigations for the adhesion properties of SWNT have been launched both by experiments [100, 38, 103, 104, 105] and modeling [106, 107, 108, 109, 110, 111, 112]. Using atomistic simulations, Buehler and co-workers [106] observed that wirelike CNTs behave similarly to flexible macromolecules and can form thermodynamically stable self-folded structures, the folding and unfolding transition are due to an entropic driving force that dominate over the elastic energy at elevated temperature. Shortly after, the contact length for self-folded single and multi wall carbon nanotubes is predicted [109]. Hertel et al. simulate the van de Waals interaction between the CNT and the substrate which results in high binding energy. They experimentally measured this binding energy of $0.8 \pm 0.3 \mathrm{eV}/\mathring{\mathrm{A}}$ by controlling the shape of crossed CNT adsorbed on a silicium substrate, their analysis is performed with an AFM, and they use the tip to induce various deformations of the CNT :

bending, straightening, translating, and rotating [105, 112]. A nonlinear deformation of CNT above a CNT-bundle substrate due to the van de Waals interaction is reported by Li et al [107]. Tang et al. reported how single wall carbon nanotube with a circular cross section can collapse into ribbons under the influence of self-van de Waals interactions by molecular simulations [108]. The estimation of adhesion forces between SWNT mentioned above are based on the hypothesis of perfect (defect free) nanotubes, it is noted that the imperfections, for instance, defects and some avoidable contamination during synthesis process of the nanotube can largely affect those simulation results, thus to experimentally measure this adhesion force is challenging but imperative.

The experimental study of adhesion interaction of nanotubes is limited partially due to the technical realization, obstacles brought by nano-positioning and precise nano-manipulation of nanotube. Some pioneers has been investigating these adhesive properties of nanotube using several smart but indirect measurements. Among those techniques, atomic force microscopy (AFM) is the first choice to study directly the adhesion properties of nanotube, and involved interactions, friction, etc. Bhushan and co-workers [38] investigated in ambient the adhesion and friction at crossed nanotube junctions by using AFM in tapping mode : a conventional AFM probe tipped with a multiwall carbon nanotube (MWNT) is scanned across a SWNT that is suspended over a 2-µm-wide trench. From force-distance curves and scans from hard trench surfaces, they found the adhesion between the nanotubes critically depend on the morphology of the MWNT tip. The adhesive force and friction force can be estimated by analysising the attenuation of vibrational amplitude of AFM cantilever. They measured the adhesive force when the MWNT tip end detached from the shell of the SWNT, the adhesion force is evaluated to be 0.7 ± 0.3 nN. By dividing the friction with the measured adhesion force,they gave the upper limit value of coefficient of friction is around 0.006 ± 0.003. Due to the impact of presence of water at the nanotube-nanotube interface in ambient, the measured shear strength is 2 orders of magnitude larger than reported [113]. Kis and coworkers [95] performed a experiment to measure interlayer force during prolonged, cyclic telescoping motion of a multiwall carbon nanotube. The force acting between the core and the outer casing is modulated by the presence of stable defects and generally exhibits ultralow friction, below their measurement limit of 1.4×10^5 N/atom and total dissipation cycle lower than 0.4 meV/atom. This is more than an order of magnitude lower than the previous estimate of 2.3×10^{-14} N/atom on the interlayer friction [100] and lower than the observed friction for one of the least dissipative nanoscale interfaces—the incommensurate contact between C_{60} islands and NaCl [114]. They found that intentionally introduced defects in the form of dangling bonds lead to temporary mechanical dissipation, but the innate ability of nanotubes to self heal rapidly optimizes the atomic structure and restores smooth motion. Their measurement give a new sight into the fundamental properties of interlayer action in MWNTs, defects that are inevitably brought during synthesis process can strongly modulate the van der Waals force between the inner layer and the outer layer of the nanotube, yet the motion exhibits ultraslow friction. Ke et al. [115] provided

a in situ mechanical peeling test to probe the property of SWNT bundles without compromising the property of material. They presents a in situ peeling method to study adhesive interactions between SWNTs by using a high resolution scanning electron microscope (HRSEM), they mechanically peel a single SWNT bundle from the bundle of SWNT, they clearly reveal the process of stripping off of the bundle in a nano manipulation technique. A nonlinear elastic theory is used to interpret the measured deformation curves and to compute the adhesive force as well as adhesive energy quantitively.

Besides, several hundreds or thousands year ago, when the people see the geckos can run rapidly on walls and ceilings freely attribute it to the special structure of its toes. The extraordinary capabilities of geckos triggered great interests of people to investigate the mechanism of the adhesive toe, which contains steal arrays consisting of hundreds of spatulae on each seta, which allows intimate contact between the spatulae and nearly any kind of surfaces, rough or smooth, hydrophilic or hydrophobic. This biological adhesion is revealed conducting through van der Waals force with various surfaces [116, 117, 118, 119]. Study to the friction and adhesion of this kind of phenomenon can give potential guideline to fabricate dry adhesives. Nanotubes have the similar adhesive property as gecko toes that have been probed to help understand the mechanism of dry adhesives. Wang and co-workers [120] created a gecko-foot dry adhesives using a special carbon nanotube array that with a straight aligning body and a curly entangled end segment at the top, which gives a macroscopic adhesive force of ~ 100 newtons per square centimeter, it is nearly 10 times larger than that of a gecko foot, the strong interaction between the nanotubes and the surface shows a very strong shear force much larger than the normal direction force, which allows strong binding along the shear direction and easy lifting in the normal direction. This CNT-based dry adhesives can be alternatively binding on and lifting off over many surfaces to mimic the movement of a living gecko .

For most of the experiments, one usually get access to either intrinsic properties of the CNT, or its interaction with the outside environment, using hypotheses on the other properties. Direct measurement of the force of adhesion can overcome this obstacle and offer quantitative measurement of several properties in a single test, which is our interest to probe in this thesis.

Recently, peeling test at nanoscale offered a potentially powerful tool to characterize the adhesion properties of CNT or nanowires on various substrates. A number of experiments have been performed trying to find a way to measure the adhesion force of the CNT [121, 122, 115, 103, 123], however, it is still challenging due to complex comparison with numerical simulation that are needed to obtain quantitative description of the nanointeraction. In this chapter, we will propose a simple protocol to conduct peeling test, with which we access direct quantitative characterization of the adhesion property of CNT.

4.2 Experimental approach

In our experiment, single wall carbon nanotube (SWNT) are grown by the CVD method. Its schematic diagram is shown in figure 4.4 : the reaction chamber is a quartz tube, with a length of 130 cm and diameter of 6 cm. During the growth process, the tube is heated up to 900°C and this temperature is stable and controllable over a distance of few tens of centimeters in the middle of the tube. In addition, its inside is absolutely isolated from the atmosphere, because any oxygen leak can cause an explosion in the tube. Reactants are fed from the gas cabinets into the reaction chamber through a gas circuit that controls the flow of each species and provides safety arrangements for usage of the highly explosive gases : in CVD synthesis of carbon nanotubes, usually explosive gases are used at temperature well above their autoignition temperature and safety regulations need to be carefully considered. The most important part usually used are a water bubbler and paraffin trap at the exhaust to cool and neutralize the exhaust gases to prevent the flash back of gases to the cylinders and thus the spreading of explosive to them.

Before the growth, the target cantilevers (CONT20, *NANOWORLD*, Ltd.) were dipped into a ferric nitrate-IPA (isopropyl alcohol) solution with a concentration of 200 μg/ml for 10 seconds, and then were dipped into n-hexane for 10 seconds for rinsing and dried in air in the end. Here, ferric nitrate is used as catalyst for the growth, the solution was prepared one night before the growth, and kept being stirred until to the growth. The as-prepared micro cantilevers were put onto a silicon wafer substrate with theirs tip upright to the top (see figure 4.4), then were placed in the center of the tube. The tube chamber was heated to 900°C under argon atmosphere with a flow of argon (600 sccm) and hydrogen (400 sccm). After 10 mins of stabilization, CNT's synthesis was carried out for another 10 mins by adding methane (CH_4, 1200 sccm), ethylene (C_2H_4, 26 sccm), hydrogen (H_2, 500 sccm) while the argon source was turned off. The reaction chamber was cooled down over a half-day with argon flows on and the cantilevers were brought out when the chamber's temperature was below 200°C.

The yield of the growth is about 30% : one every three cantilevers has a nanotube that has been grown on its tip. An example of a successfully grown SWNT with a length of 400 nm on the tip of the AFM cantilever, is imaged by Scanning Electron Microscopy (SEM) in figure 4.5. This vertically grown nanotube is then pushed to a flat surface to conduct a series of experiments. All these preparation, growth and SEM imaging are performed in the LPMCN, Lyon 1 university, in collaboration with Athony Ayari.

4.2.1 Adhesion force measurement

To probe the adhesion properties of nanotubes, we measure their adhesion force on a substrate. To measure this force, we need to know the spring constant k of the cantilever. In conventional AFM setup, the calibration of the spring constant implies a hard contact process, in which the cantilever tip is pushed onto a hard surface to

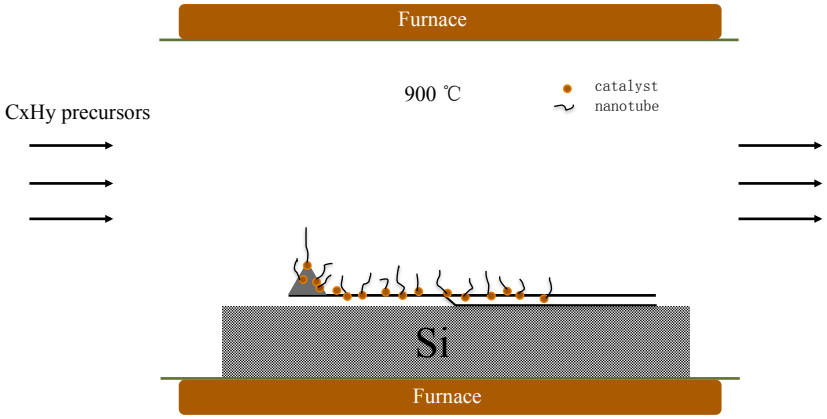

FIGURE 4.4 – Schematic diagram of CVD reaction chamber. Nanotubes grow everywhere on the cantilever and tip from the catalyst nanoparticles

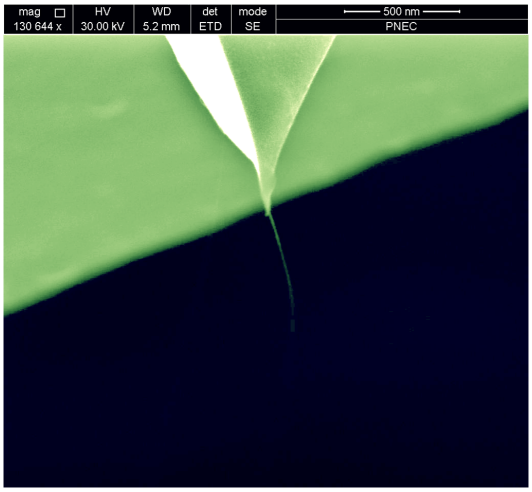

FIGURE 4.5 – Scanning electron micrograph (SEM) of a SWCNT with a length of 400 nm grown directly on an AFM tip. In experiment, it is pushed almost perpendicularly against a flat surface to perform a series of peeling tests.

calibrate the sensitivity of the photodiode. In our case, on the tip of the cantilever is grown a nanotube, the hard contact calibration is thus not applicable, it would be harmful to the nanotube. However, in our setup, we can calibrate the cantilever by thermal noise as presented in detail in the chapter 3 with our quadrature phase interferometer : when the cantilever is in equilibrium with the environment, the thermal induced fluctuations can be described by $k_B T/2 = k \langle d^2 \rangle /2$, this thermal excitation operates like a random force (white noise) on the cantilever. Using our quadraphase interferometer, we record with high resolution the deflexion fluctuation d of cantilever, we can compute the power spectrum density (PSD) of the deflexion d. As shown in figure 4.6, the first resonant peak of PSD is well described by the simple harmonic oscillator model (SHO model) (as discussed in the chapter 3). By fitting the first resonance, we easily get the dynamic spring constant k of the first mode of the cantilever. For the cantilever being probed here, $k_1 = 0.1\,\mathrm{N/m}$. According to the description of Euler Bernoulli [40], the static spring constant of the cantilever can thus be derived by $k = 0.97 k_1 = 0.097\,\mathrm{N/m}$. That is to say, our way to calibrate the cantilever is fully contact-less, the commercial AFM counterpart requires however a hard contact force curve to get precise calibration, during which a conversion factor from Volt to meter is involved. In our case, what the interferometer measures here is the actual deflexion of the cantilever without needing any conversion factor. When the interaction between the nanotube and the surface can be supposed to be quasi-static and the interaction force vertically applied on the tip, as illustrated in figure 4.7, the adhesive force of the nanotube can be given with derived static spring constant by $F = -kd/\cos(\theta_{\mathrm{AFM}})$, where $\theta_{\mathrm{AFM}} = 15°$ is the inclination of the cantilever with respect to horizontal direction.

In the experiment, we push the nanotube against the substrate (graphite, mica, ...) and retract it away. During approach, the induced increasing bending of the nanotube becomes strong enough to cause part of the tube to adsorb to the surface, retracting the nanotube leading thus to a peeling with respect to the substrate. The process of absorption of nanotube is used to extract information about its adhesion and the intrinsic properties. Our tricky approach differs largely with the other existing peeling tests in the orientation of the nanotube : it is nearly perpendicular (see figure 4.7) to the flat surface while other peeling tests mostly choose a parallel configuration or large peeling angle [121, 122, 123, 124].

The instrument has been already introduced in chapter 2 in detail, in order to offer a general understanding to readers the train of though of our work, I still want to mention some key characteristics before introducing static force curve. The vertical position z_s of the flat surface is controlled by a piezo translation platform that works in closed loop, with a resolution of 0.3 nm rms. The precise measurement of the deflexion d is realized with our home made quadraphase interferometic setup that reaches an intrinsic background noise level lower than $10^{-27}\,\mathrm{m^2/Hz}$. The advantage of our setup not only lies in the quite low background noise but also in its intrinsic calibration for the measurement of the deflexion d. Using calibrated d and z_s, we can thus compute easily at any time the compression of the nanotube by $z_c = z_s - d\cos(\theta_{\mathrm{AFM}})$. θ accounts for the 15° inclination of the AFM cantilever with

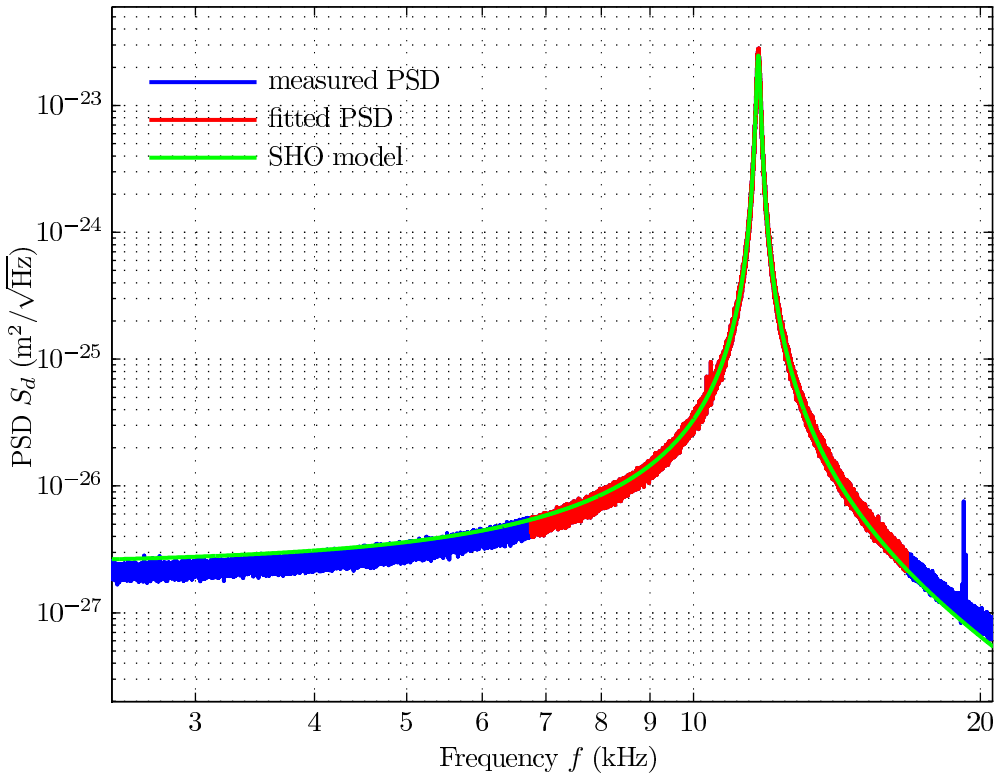

FIGURE 4.6 – PSD of mechanical thermal noise of a *Nanoworld* CONT20 cantilever, the first resonant frequency is fitted by SHO model to get the spring constant of the first mode : k_1 =0.1 N/m. The derived static spring constant $k = 0.97k_1$ is : 0.097 N/m.

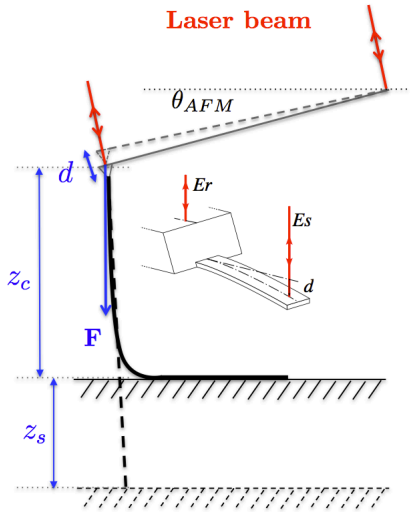

FIGURE 4.7 – Schematic diagram of adsorption of the nanotube : the nanotube is pushed perpendicularly against the flat substrate. The deflexion of the cantilever d is recorded in real time by the interferometer as a function of the position of the surface z_s, the adhesive force F is thus computed by $F = -kd/\cos(\theta_{\mathrm{AFM}})$.

respect to the horizontal direction of the sample (see figure 4.7). The origin of z_c is defined as the last contact point of the nanotube with respect to the substrate, in the case of strong interaction, this points corresponds to a fully extended nanotube with a zero compression.

With the measured deflexion d and recorded substrate position z_s, we plot an example of measured force F as a function of compression z_c on graphite, as shown in figure 4.8. Three approach-retract cycles are overlapped, implying the force curve is quite reproducible, the measured forces reflect thus the intrinsic structure of the nanotube.

During approach, when the compression $z_c > 210\,\mathrm{nm}$, nanotube snaps into contact with the substrate, leading to a slight adhesion in the force curve. As the approach continues, the nanotube undergoes a little increased force and a small plateau. After a big jump, it faces a increasing repulsive force until the maximum compression corresponding to the largest extension in the ramp of the piezo (red curve). The compression range where the force is none zero during retraction is around 600 nm which is longer than that of approach, this corresponds to extension of nanotube during retraction. The origin of z_c relates to the last contact point of a fully extended nanotube. The retraction force presents a similar characteristic as approach : a big and a small jump locate at 480 nm and 300 nm, a plateau force in between. In addition, the retraction curves present a strong hysteresis over the most range of retraction with respect to the approach one, indicating that an attractive force is always sensed by the tip during retraction.

The different behaviors of the force curve reflects the intrinsic structure of the nanotube, as the force curve is highly reproducible, the jump at 480 nm and 300 nm

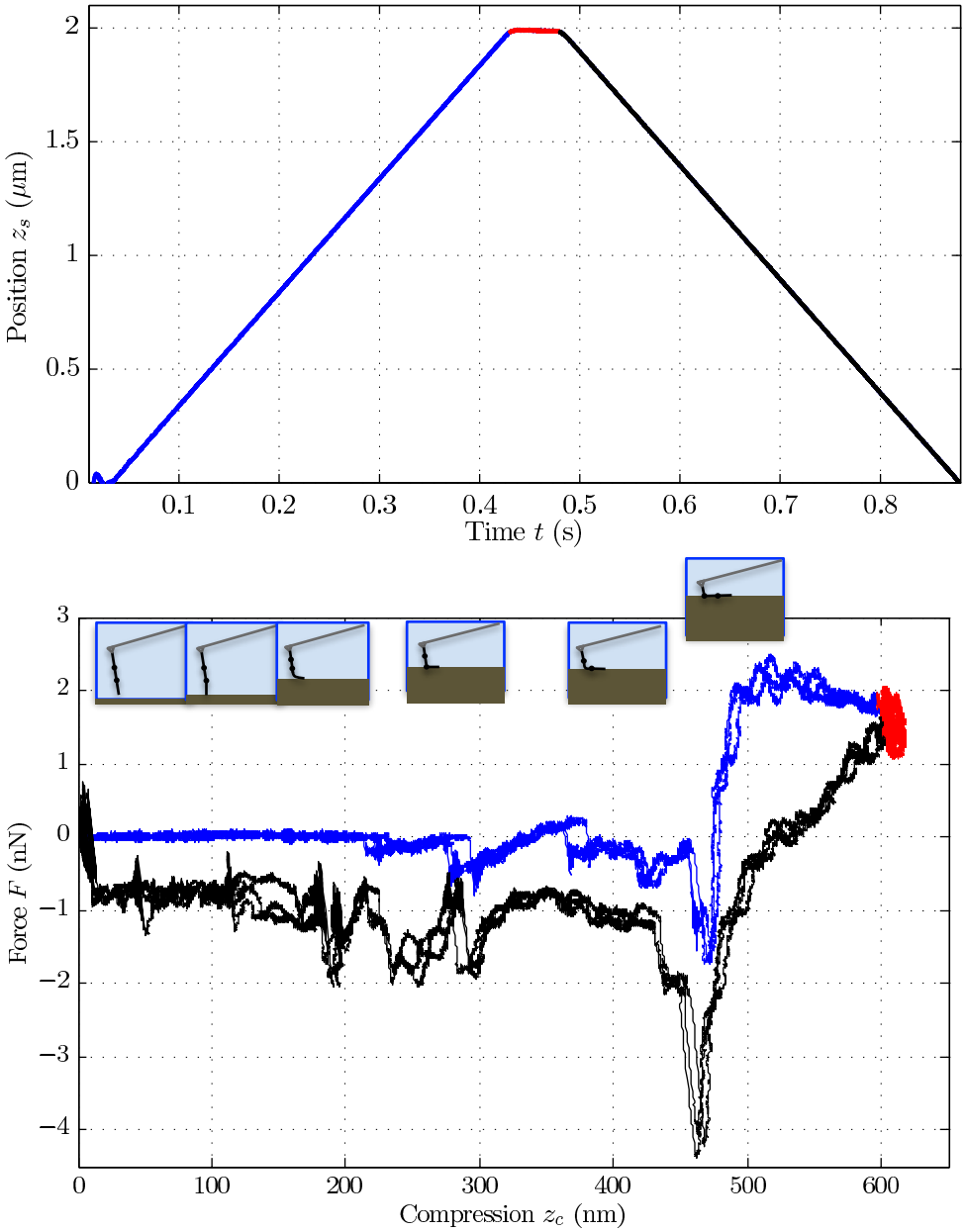

FIGURE 4.8 – Time trace of piezo on a normal ramp (top) and force curve as a function of compression on graphite (bottom). Blue, red, and black curve link to approach, rest, retraction of the piezo. Three approach-retract cycles are overlapped. The measured force curves are quite reproducible, indicating they reflect the intrinsic structure of the nanotube. The sketches in the force curves give a possible scenarios of interaction of the nanotube and its defects with the substate.

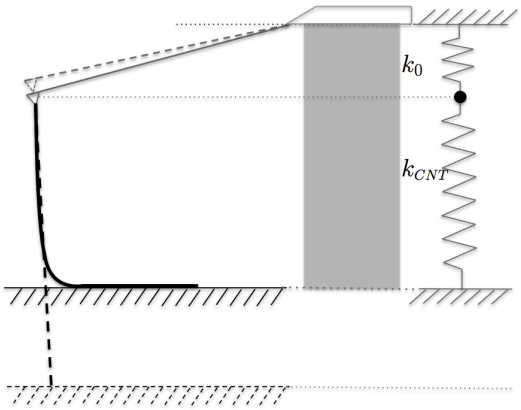

FIGURE 4.9 – The scheme shows that the spring constant of the cantilever shifts to an effective value : $k_0 + k_{\mathrm{CNT}}$ when the nanotube get into contact with the substrate. The stiffness of the cantilever when in contact is $k_0 + k_{\mathrm{CNT}}$ rather than $\frac{k_0 k_{\mathrm{CNT}}}{k_0 + k_{\mathrm{CNT}}}$, this is because the cantilever and the nanotube are connected in parallel rather than in series, since we monitor the thermal noise driven deflexion when the position of the sample is fixed.

correspond to two defects of the nanotube. In section 4.3.2, I will explain precisely the peeling mechanism of two nanotube parts that are connected by a defect, which is leading to a big negative force.

4.2.2 Time-frequency analysis

If the speed of the translation of the piezo is sufficiently low, it allows us stay long enough at any portion along the nanotube during the compression, so that we can compute the power spectrum density (PSD) of the deflection of the cantilever that is excited by thermal noise. Here, the force sensed by the cantilever not only comes from the cantilever itself, but also from the contribution of the adsorbed nanotube touching with the substrate. In this configuration, the effective spring constant of the mechanical system is $k_0 + k_{\mathrm{CNT}}$: the cantilever is just modeled as an harmonic oscillator with a static spring constant k_0, effective mass m_0, and resonant repulsion ω_0, the contact of the nanotube with the surface add a extra stiffness k_{CNT}, as shown in figure 4.9. The resonant frequency in contact thus presents a shift with respect to that in free standing state (out of contact).

We plot the relative PSDs of deflexion d in a 20 ms window for the two states, in contact and out of contact of the nanotube in figure 4.10. The cantilever's resonant frequency is clearly shifted. For a harmonic oscillator :

$$\begin{cases} \omega_0^2 & = & \frac{k_0}{m_0} \\ \omega_{\mathrm{CNT}}^2 & = & \frac{k_0 + k_{\mathrm{CNT}}}{m_0} \end{cases} \tag{4.2}$$

The equation 4.2 gives the peeling stiffness of the nanotube in contact :

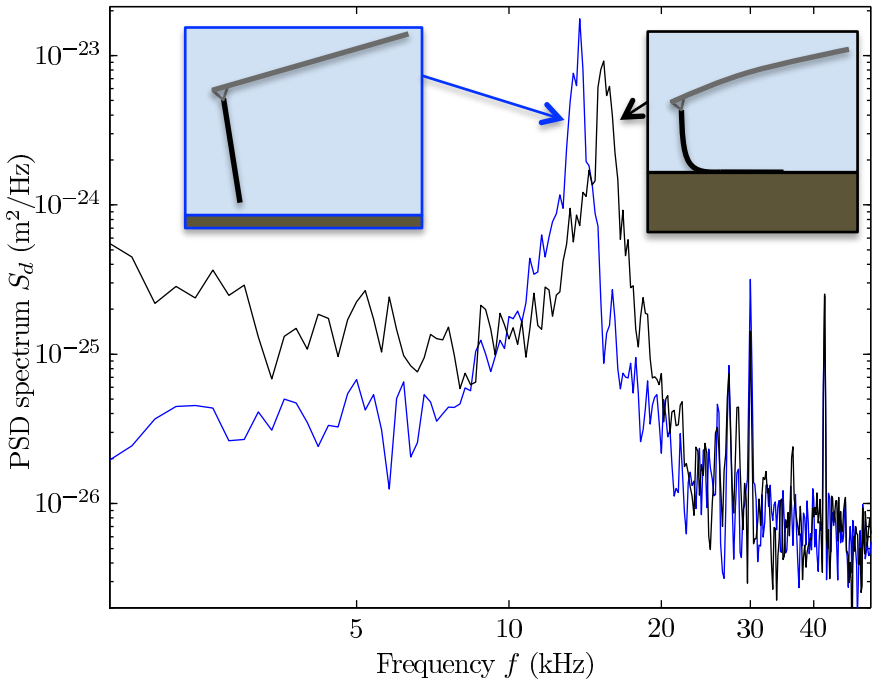

FIGURE 4.10 – Power Spectrum Density (PSD) of the deflexion signal computed in a 20 ms interval before (blue) and during (black) contact. During the absorption of the nanotube, the resonant frequency of PSD in contact is clearly shifted with respect to that out of contact (free standing state).

$$k_{\mathrm{CNT}} = k_0 \left[\left(\frac{f_{\mathrm{CNT}}}{f_0} \right)^2 - 1 \right] \tag{4.3}$$

where f_0 and f_{CNT} are the resonant frequency of out of contact and in contact of the cantilever oscillator system.

When taking into account of the 15° inclination of the cantilever, the equation 4.3 is modified slightly into :

$$k_{\mathrm{CNT}} = \frac{k_0}{\cos^2 \theta_{\mathrm{AFM}}} \left[\left(\frac{f_{\mathrm{CNT}}}{f_0} \right)^2 - 1 \right] \tag{4.4}$$

The time interval used to compute PSD from the deflexion is critical to the precision of the estimated stiffness of the nanotube. In the experiment, in order to probe the stiffness of an adhered nanotube at any time, we restrict this interval to 5 ms. From the frequency shifts in a small time interval, we can estimate the peeling stiffness of the nanotube, this is the main purpose of time-frequency analysis method.

We perform this analysis of the deflexion of the cantilever during a slow translation of the piezo. The shifted resonant frequency (see equation 4.4) can be used to access to k_{CNT} at each time as long as f_{CNT} can be identified easily on each PSD $S_d(t, f)$. 5 ms time interval corresponds to 5 nm translation of the piezo since its speed is around 1 µm/s. Any characteristics of nanotube longer than 5 nm can be detected, thus giving a highly sensitive way in exploring peeling stiffness of the tube.

The computed PSD is plotted in figure 4.10, due to very short time (20 ms is used here) window, it is very noisy, it is thus hard to read a precise value of f_{CNT}, the frequency resolution is only 200 Hz. We compare the PSD deduced from 5 ms window and from 100 ms figure 4.12, it is clear that the PSD computed in 100 ms window is smoother to be fitted by SHO model to refine the resonant frequency, wheres the PSD in 5 ms one is too noisy to be fitted. As the ramp time (see figure 4.11 (**(a)**)) spans only 0.5 s, the adhesion time (the nanotube is being adhered to the substrate) is even shorter around 0.15 s, the fit of PSD in 100 ms window is evidently not enough for the ramp used here. In Chapter 6, we will focus on a specially designed ramp, where the nanotube can stay or undergo a slow speed of ramp that leaves us longer time to perform time-frequency analysis to the data. In order to estimate the resonant frequency at each small time interval, we use the following estimator :

$$f_{\mathrm{CNT}}(t) = \frac{\int_{\Delta f} f S_d(t, f)\, \mathrm{d}f}{\int_{\Delta f} S_d(t, f)\, \mathrm{d}f} \tag{4.5}$$

where Δf is an adequate frequency interval centered on f_{CNT} (self adapting procedure). By this trick, we can identify easily the f_{CNT} on a noisy PSD.

We plot the results of time-frequency analysis to the deflexion in figure 4.11 (**c**) : Before the nanotube gets into contact with the substrate, the resonant frequency of the mechanical oscillate system obviously equals to the resonant frequency of the free standing cantilever : $f_{\mathrm{CNT}} - f_0 = 0$ before $t < 0.17$ s. From $t = 0.17$ s to $t = 0.37$ s, the nanotube is in contact with the substrate and the f_0 shifts to a larger

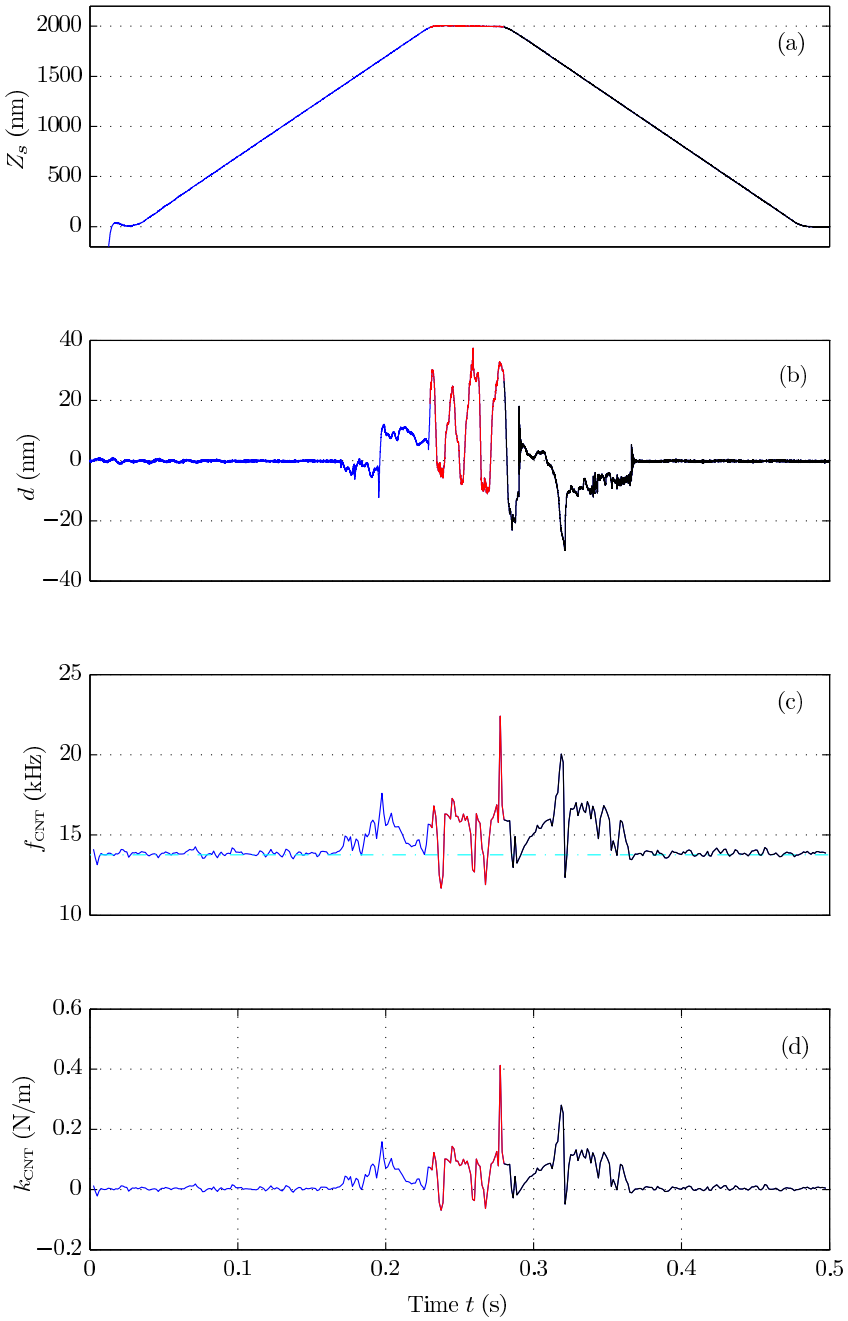

FIGURE 4.11 – Time trace of the substrate position z_s (**a**), deflexion d (**b**), resonant frequency f_0 (**c**), dynamic stiffness of nanotube k_{CNT} (**d**) during an approach-retract cycle. The color blue, red, and black lines indicates the approach, rest, retract translation of the piezo. The dotted cyan line in (**c**) indicates the resonant frequency of the cantilever in out of contact state to give a comparison with f_{CNT}. Thermal induced fluctuations excite the AFM cantilever, the first mode resonant frequency shift implies a changed stiffness of this small mechanical oscillator that is composed of AFM cantilever, nanotube and the substrate (see figure 4.9). We compute the PSD of the deflexion of the cantilever d for every 5 ms time window. In the case of with very short time interval, it is hard to fit the PSD by SHO model, however, with an estimator 4.5, we can still access at each time to the dynamic stiffness of nanotube by equation 4.4 with a high precision.

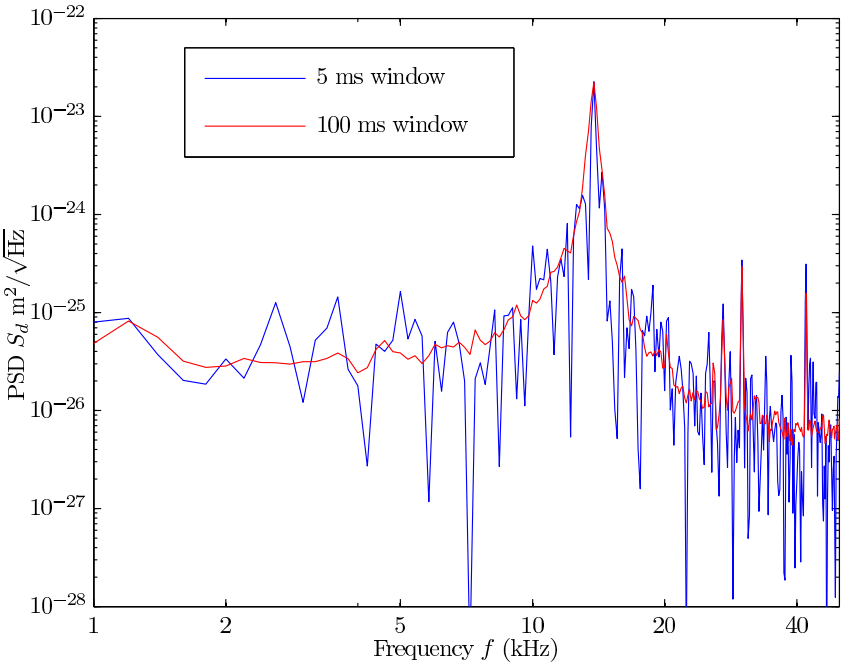

FIGURE 4.12 – The comparison of PSDs computed in 5 ms window and in 100 ms window. The spectrum of 5 ms is much noisier than that of 100 ms. The resonant frequency estimated by equation 4.5 matches with a trustable precision with the value from the averaged curve that is fitted by a simple harmonic oscillator model (SHO).

value that corresponds to f_{CNT}. When $t > 0.37\,\mathrm{s}$, the stiffness of the nanotube goes back to 0, which corresponds to the recovery of the nanotube to out of contact state, implying the nanotube gets away from the surface. In figure 4.11 (d), we plot the deduced stiffness of the nanotube in contact k_{CNT}.

The time-frequency analysis is thus a useful way to access to the dynamic stiffness of nanotube at each time during the peeling test. The thermal induced fluctuations are strong enough to excite the cantilever, giving possibility of determining the resonance of the cantilever through an estimator. The dynamic stiffness of nanotube during the contact corresponds to the response of nanotube when it undergoes random excitations at fast time scale. It gives us a value of the dynamic stiffness k_{CNT}, and by conducting the time-frequency analysis on the force plateau, it leads to the proposal of questions about the dynamic peeling stiffness of the nanotube in section 6.3.

4.3 Description of carbon nanotube : Elastica

In this section, we will explain our model describing the nanotube when it is approached perpendicularly against to a flat surface. This part is strongly inspired by references [125, 29].The nanotube here is modeled as an elastic line, it is not compressible along its length, and we assume the surface can not be deformed (infinitely stiff) when it is in interaction with the nanotube. As figure 4.13 illustrates, the approached nanotube is described by a parameter curve with coordinates $x(s)$ and $z(s)$, where s is the arc length along the nanotube. We define the **O** as the origin of the nanotube ($s = 0$), it is the tip of the cantilever holding the nanotube, the point **L** as the first contact point ($s = L$) of the nanotube with the surface, where L is the length of the free standing part of the nanotube. Thus, the coordinate of L can be given as :

$$X = \int_0^L \sin\theta \, ds \tag{4.6}$$

$$Z = \int_0^L \cos\theta \, ds \tag{4.7}$$

where $\theta(s)$ is the local slope.

We assume that there is no external force applied along the nanotube length, except at the two extremities $s = 0$ and $s = L$. When the nanotube lies in equilibrium, the force acting on the two extremities should present the same absolute value but opposite directions, as indicated in the figure 4.13. The same arguments hold for every part of CNT, thus the force is constant along the nanotube. We also assume that the horizontal force $F_x\mathbf{e_x} = 0$ as if the first contact point $s = L$ can freely slide on the surface, thus the sensored force at the origin ($s = 0$) is vertical : $\mathbf{F} = F\mathbf{e_z}$.

The bending moment M at each point along the nanotube length can be linked to its local curvature :

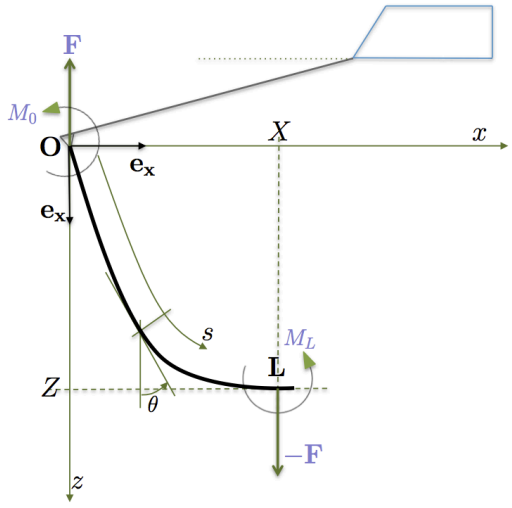

FIGURE 4.13 – The nanotube we approach against to the substrate is described by a parametric curve with its coordinates $x(s)$ and $z(s)$ as sketched, s is the arc length from the origin **O** to the first contact point **L** of the nanotube with the substrate. When part of the nanotube is adsorbed on the substrate, the free standing part length L is always smaller than the total length of the nanotube L_{total}.

$$M = EI\frac{d\theta}{ds} = EI\theta' \tag{4.8}$$

where E is the Young's modulus and I the quadratic moment of the nanotube. In equilibrium, the sum of the moments applying on an infinitesimal element should be zero, this leads to the expression of the elastica [126] :

$$\frac{\mathrm{d}M}{\mathrm{d}s} = EI\frac{\mathrm{d}^2\theta}{\mathrm{d}s^2} = EI\theta'' = -F\sin\theta \tag{4.9}$$

$F < 0$ corresponds to an attracting force at the extremity $s = 0$ while $F > 0$ corresponds to a repulsive force.

By integrating equation (4.9), we get the first invariant expression of the Elastica :

$$EI(\theta'(s) - \theta'(0)) + Fx(s) = 0 \tag{4.10}$$

Multiply equation (4.9) by $\mathrm{d}\theta$ and integrating, we obtain the second invariant expression of the Elastica :

$$\frac{1}{2}EI\theta'(s)^2 - F\cos\theta(s) = \text{Constant} \tag{4.11}$$

Two boundary conditions are needed to get the solution of the expression (4.10) and (4.11) since they are second order differential equations. The classical boundary condition at the origin is $\theta = \theta_{\text{AFM}}$ or $\theta' = 0$, corresponding to 'clamped hypothesis'

and 'torque free hypothesis', respectively. In the latter part 4.3.2, we will present which hypothesis is more realistic to describe our measurements.

4.3.1 Force plateau

We study in this section the case of a nanotube partially adsorbed on the substrate. It implies that the length L of the free standing part of the nanotube is smaller than the total length of the CNT L_{total}, and that the final slope of the nanotube is horizontal : $\theta(L) = \frac{\pi}{2}$. The interaction between the nanotube and the substrate is mainly due to the van der Waals force, a short-range force that can be lost as soon as the distance between the nanotube and substrate is larger than a few nanometers. In our research, we focus on the pure contact case which means that the van der Waals force disappears as soon as the nanotube is peeled away from the surface. E_a is defined as the adhesion energy per unit length of the nanotube.

For a given shape of the nanotube, the curvature energy is :

$$E_c = \int_0^L \frac{1}{2} EI\theta'(s)^2 \mathrm{d}s \tag{4.12}$$

The total energy of the nanotube E_{total} is the sum of the curvature energy E_c which is due to the deformation of the nanotube and the adhesion energy E_a which is due to the partially adsorbed nanotube on the surface, we have :

$$E_{\text{total}} = E_c(Z, L) - L_c E_a \tag{4.13}$$

where L_c is defined as $L_c = L_{\text{total}} - L$, the length of the nanotube in contact with the substrate. For a given distance Z between the origin and the surface, the length L of the free standing part of the nanotube adjusts itself by minimizing the total energy in order to get to a stable state. In equilibrium, the adhesion energy of the nanotube is given by [127, 128] :

$$E_a = -\left.\frac{\partial E_c}{\partial L}\right|_Z = \frac{1}{2} EI\theta'(L)^2 \tag{4.14}$$

I would like to refer the interested reader to Appendix C for more details of (4.14). It can also be rewrote as :

$$\theta'(L)^2 = {\theta'_L}^2 = \frac{2E_a}{EI} = \frac{1}{R_a^2} \tag{4.15}$$

where we defined the natural radius of curvature R_a for the first contact point.

As soon as the nanotube is partially adsorbed on the surface, the system tends to minimize its total energy by maximizing the absorbed length L_c. However, this change of the CNT increases the bending of the free standing part of the nanotube and thus its curvature energy $E_c(Z, L)$. The adsorbed length will thus be a balance between the bending and the adhesion. If the free standing part of the nanotube is long compared to its natural radius of curvature R_a, its shape does not change much when it is peeled from the surface. The vertical displacement δz needed to

peel a small length δl is in first approximation $\delta z \simeq \delta l$. The work produced as we are peeling with a force F is $F\delta z$ while the energy released during the peeling is $-E_a\delta l$, it is directly leading to $F \simeq -E_a$: peeling the nanotube will result in a flat force-compression curve.

Figure 4.15 shows the numerical integration of the elastica, for a total length $L_{\text{total}} = 5R_a$ [29]. When $z_c > R_a$ and $z_c < 3R_a$, the adhesion force is clearly equivalent to the adhesion energy $F = -E_a$. The result is also valid with different clamping conditions at the origin as will illustrate in section 4.3.2. This force plateau is clearly seen in our measured force curves, as shown in the figure (4.8). More obvious force plateaux are illustrated in section 4.3.2 in figure 4.16 : about 4 plateaux are clearly found in the force curve, the large negative peak in the force curve will be reasonably understood with torque free boundary condition.

4.3.2 Clamped origin or torqued free origin ?

In previous section, under the condition of large length of the adsorbed nanotube compared to the radius of curvature, when it is peeled off from the substrate, we show that the force measured by the cantilever is equivalent to the adhesion energy E_a per unit length. However, the question comes when the limit condition is not met, that is to say, compression is large and the free standing length of the nanotube is small, as shown in the figure 4.15. The boundary at the origin can play an important role in behaviors of the adhesive force, it has to be therefore carefully considered as well.

When the nanotube is approached against or pulled off from the substrate, we have two possible boundary conditions to describe the extremity of the nanotube, one is clamped origin : the origin is clamped (see figure 4.15), the nanotube is not allowed rotating but keep a fixed inclination with the AFM cantilever [1].

$$\theta(0) = \theta_0 = \theta_{AFM} \tag{4.16}$$

Another simple boundary condition is the torque free origin (see figure 4.17) :

$$\theta'(0) = \theta'_0 = 0 \tag{4.17}$$

In the torque free origin hypothesis, the origin can be rotated freely (θ can be any angle). We will demonstrate next that the two different boundary conditions present almost opposite force behaviors. Note that the clamped origin discussed here is natural to describe the connection between the nanotube and the tip of the cantilever since the elastica model we used is a defect-free line. For the experimental synthesized nanotube, however, defects are hard to avoid to obtain an ideal tube, the concept of origin is linked to the first defect found after leaving the surface.

1. θ_{AFM} is the angle that the AFM cantilever present with respect to the surface, it is designed in the setup so that the cantilever can image various samples especially those with uneven morphology. When the nanotube grows along the tip, the inclined tip gives the nanotube almost the same angle with the vertical direction, as shown in the figure 4.5 and 4.13.

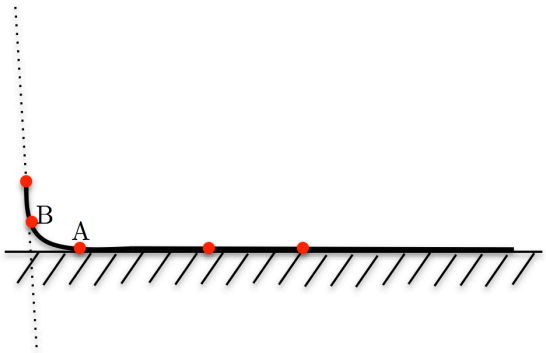

FIGURE 4.14 – Boundary condition in limiting case at the origin : clamped origin

Could this defect can be freely rotated ? We will compare the measurement with the proposed two boundary conditions to discuss the actual force behavior induced by the defects.

Clamped origin :

We define s_{max} correspond to the coordinate of the maximum value of θ', we have :

$$\frac{1}{L}(\theta_L - \theta_0) = \frac{1}{L}\int_0^L \theta'(s)\mathrm{d}s \leqslant \theta'(s_{\max}) \tag{4.18}$$

Injecting $s = L$ and $s = s_{max}$ into the second invariant expression (4.11) and combining with the results (4.15), we get :

$$\frac{1}{2}EI\theta'(s_{\max})^2 - F\cos\theta(s_{\max}) = \frac{1}{2}EI{\theta'_L}^2 = E_a \tag{4.19}$$

By deforming, we thus have :

$$F = \frac{E_a}{\cos\theta(s_{\max})}\left(R_a^2\theta'(s_{\max}^2) - 1\right) \geqslant \frac{E_a}{\cos\theta(s_{\max})}\left(\frac{R_a^2}{L^2}(\theta_L - \theta_0)^2\right) \tag{4.20}$$

The limiting value when $L \to 0$ is thus [29] :

$$\lim_{L/R_a \to 0} F = +\infty \tag{4.21}$$

That is to say, when a small length of the elastic is peeled off, the force presents a diverging value with the clamped boundary condition. This result is easy to understand : as the free standing part become shorter and shorter, the different slopes of the two boundaries lead to a more and more diverging curvature. Numerical integration of partially adsorbed elastica was conducted [29]. The results are plotted in the figure 4.15, the force exhibits an adhesion plateau between the compression range $z_c < 3R_a$ and $z_c > R_a$, it however diverges to strong repulsive forces for large compressions. It is not in line with the measured experimental force curves in figure 4.8, where force plateau usually ends with large attractive forces at large

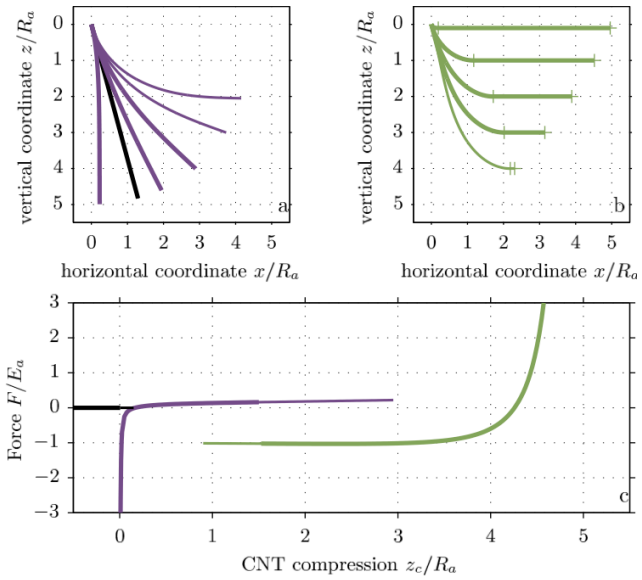

FIGURE 4.15 – Numerical integration of nanotube compression for $L = 5R_a$ with clamped boundary condition. Fundamental and metastable states are described by thick and thin lines, respectively. **(a)** shape for the point contact, **(b)** shape for adsorbed state, and **(c)** force F are illustrated as a function of compression z_c [29].

compression. This is even more obvious in figure 4.16 where a nanotube with much more defects is peeled from the surface, an large attractive force can be seen at each defect.

Torque free origin : In the case of a torque free origin, we can rewrite the first invariant equation of the elastica with boundary condition $\theta'_0 = 0$ and combining the results 4.15, we have :

$$EI\theta'_L + FX = 2E_aR_a + FX = 0 \tag{4.22}$$

With coordinate $X \leqslant L$:

$$\lim_{L/R_a \to 0} F \leqslant \lim_{L/R_a \to 0} -2E_a \frac{R_a}{L} = -\infty \tag{4.23}$$

That is to say, when the nanotube is approached in a limit case $L \to 0$, the torque free boundary condition gives a diverging attractive force. As illustrated in figure 4.18. From the numerical simulation, the force presents a plateau between the compression range $z_c < 3R_a$ and $z_c > R_a$. The curve ends with a diverging attractive force for large compressions ($z_c > 3R_a$). It is clearly more in line with the experimental data plotted in figure 4.16. Let choose the defect located at the compression 130 nm for example, the force jumps from previous plateau at F =0.5 nN, via "$-\infty$", to the next plateau at F =0.3 nN. The observed 4 plateaux are easy to interpret : the synthesized nanotube is composed of several segments linked with defects. When the peeling of the nanotube begins with a defect, the defect act like

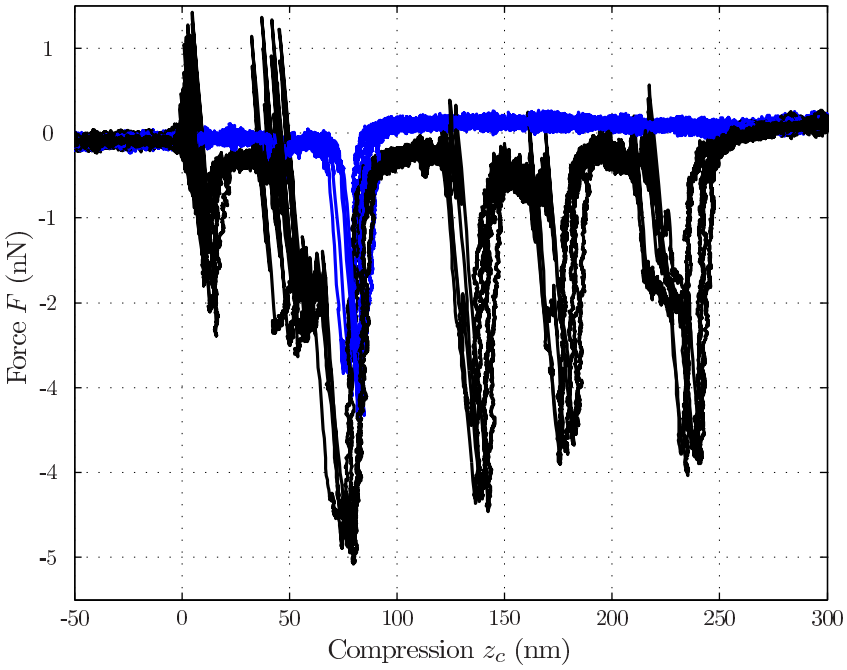

FIGURE 4.16 – Force curve of a nanotube as a function of compression on graphite, it owns more defects than the previous one. Blue and black curve correspond to the approach and the retraction, respectively. For the compression, there are 4 obvious defects can be found along the adsorbed length, they locate at the compression 230 nm, 175 nm, 75 nm and 80 nm, respectively. Four force plateau are also clear at the compression of 190 nm–230 nm, 150 nm–170 nm, 80 nm–120 nm, and 20 nm–40 nm.

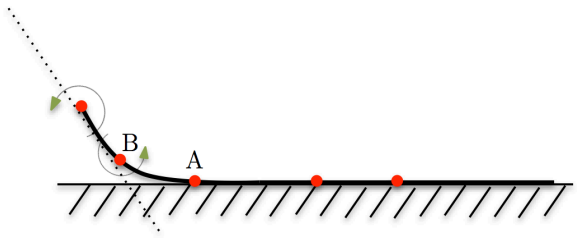

FIGURE 4.17 – Boundary condition in limiting case at the origin : torque free origin

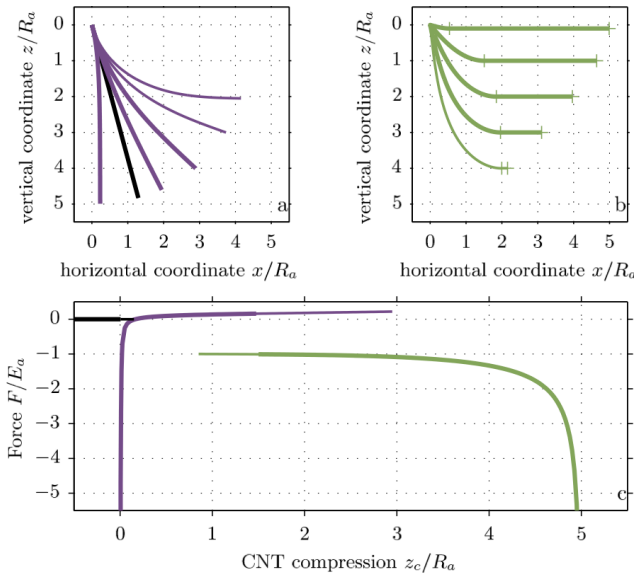

FIGURE 4.18 – Numerical integration of nanotube compression for $L = 5R_a$ with torque free boundary condition. Fundamental and metastable states are described by thick and thin lines, respectively. **(a)** shape for the point contact, **(b)** shape for adsorbed state, and **(c)** force F are illustrated as a function of compression z_c [29].

a torque free origin since its linkage with the next defect can be rotated easily, the force presents thus a infinite attractive force.

Indeed, if we want to peel a totally adsorbed nanotube from the surface, the vertical distance changes by $Z \propto X^2/R_a$ with a minimum part X being peeled off (R_a being the radius curvature at the detachment point). The energy released is $E_a X$, the work needed in this peeling is $W = FZ$, in equilibrium, we have $F \propto -E_a R_a/X$. The adhesion force should thus present a negative divergence when the part of the nanotube that includes a defect is peeled off.

4.3.3 From adhesion energy to mechanical property

Let us first rewrite the two invariants of the elastica (4.10) and 4.11 using the boundary condition of torque free origin (4.17), adsorbed end $\theta_L = \pi/2$, we obtain directly :

$$EI\theta'_L = -FX \tag{4.24}$$

$$\frac{1}{2}EI{\theta'_L}^2 = -F\cos\theta_0 \tag{4.25}$$

Injecting the definition (4.15) into the equation (4.24) and (4.25), we have :

$$F = -\frac{E_a}{\cos\theta_0} \tag{4.26}$$

$$X = 2R_a \cos\theta_0 \tag{4.27}$$

In the case of large seperation of the nanotube, It is demonstrated in the section 4.3.1 that the pulling force presents a constant value equals to adhesion energy per unit length E_a, this implies the spring contant of the nanotube is zero ($k_{\text{CNT}} = \mathrm{d}F/\mathrm{d}z_c$). However, if we suppose that the adhesion process is slow, the nanotube behaves as if the its length L is fixed and can not adjust to balance the adsorption. We will however stay in slow time scale (low peeling frequency) with respect to the dynamics of the free standing part of the nanotube, in this case, we can still use the elastica to compute the dynamic stiffness of the nanotube k_{CNT} :

$$k_{\text{CNT}} = -\left.\frac{\partial F}{\partial Z}\right|_L \tag{4.28}$$

Note that, if the adhesion process is not completely in slow time scale we are measuring, the measured stiffness is expected to be some value between slow and high time scale. We derive the equation (4.24) and (4.25) by Z :

$$EI\frac{\partial \theta'_L}{\partial Z} = k_{\text{CNT}}X - F\frac{\partial X}{\partial Z} \tag{4.29}$$

$$EI\theta'_L\frac{\partial \theta'_L}{\partial Z} = k_{\text{CNT}}\cos\theta_0 + F\sin\theta_0\frac{\partial \theta_0}{\partial Z} \tag{4.30}$$

Note that θ'_L is not perfectly constant anymore since equilibrium with adhesion is not assured at fast time scales. By injecting the solution (4.15), we get :

$$k_{\text{CNT}}(X - R_a\cos\theta_0) = F\left(\frac{\partial X}{\partial Z} + R_a\sin\theta_0\frac{\partial \theta_0}{\partial Z}\right) \tag{4.31}$$

We rewrite the equation (4.31) in the limit of large separation ((4.26) and (4.27)) :

$$k_{\text{CNT}}^{\text{peeling}} = -\left.\frac{E_a}{R_a}\frac{\partial X}{\partial Z}\right|_L (\theta_0 \to 0) \tag{4.32}$$

To describe $\partial X/\partial Z$, we need recall the equation (4.34) and (4.33) :

$$\mathrm{d}s = R_a\left(1 + \frac{F}{E_a}\cos\theta\right)^{-1/2}\mathrm{d}\theta \tag{4.33}$$

$$L = \int_0^L \mathrm{d}s = R_a\int_{\theta_0}^{\pi/2}\left(1 + \frac{F}{E_a}\cos\theta\right)^{-1/2}\mathrm{d}\theta \tag{4.34}$$

thus :

$$\begin{aligned} L - Z &= \int_0^L (1-\cos\theta)\mathrm{d}s \\ &= R_a\int_{\theta_0}^{\pi/2}(1-\cos\theta)\left(1 + \frac{F}{E_a}\cos\theta\right)^{-\frac{1}{2}}\mathrm{d}\theta \end{aligned}$$

As large separation always obeys the limit $Z \geq R_a$, $F \simeq -E_a$, plus the boundary condition $\theta_0' = 0$:

$$L - Z \simeq R_a \int_0^{\pi/2} (1 - \cos\theta)^{\frac{1}{2}} \mathrm{d}\theta = 2(\sqrt{2} - 1)R_a \tag{4.35}$$

With the description (4.25), we thus have :

$$L - Z = 2(\sqrt{2} - 1)R_a = (\sqrt{2} - 1)X \tag{4.36}$$

The equations above leads to :

$$\left.\frac{\partial X}{\partial Z}\right|_L (\theta_0 \to 0) = -1 - \sqrt{2} \tag{4.37}$$

The dynamic stiffness of the nanotube can be written as :

$$k_{\mathrm{CNT}}^{\mathrm{peeling}} = (1 + \sqrt{2})\frac{E_a}{R_a} \approx 2.4\frac{E_a}{R_a} \tag{4.38}$$

The equation (4.38) demonstrates that the dynamic stiffness of the nanotube is also a constant value, it is linked to the adhesive energy per unit length E_a and the radius curvature R_a. The value of the dynamic stiffness can further give us access to the bending stiffness EI of the nanotube :

$$EI = 2E_a R_a^2 = (6 + 4\sqrt{2})\frac{E_a^3}{k_{\mathrm{CNT}}^{\mathrm{peeling}\,2}} \tag{4.39}$$

The quadratic moment I is a function of the geometry of the nanotube [126] :

$$I = \frac{\pi D_{\mathrm{CNT}}^3 t_{\mathrm{CNT}}}{8} \tag{4.40}$$

where D_{CNT} is the diameter of the nanotube, t_{CNT} the wall thickness (for a single wall carbon nanotube, it is around 0.34 nm [97]). For a given value E =1 TPa, we can extract the geometric information of the nanotube by measuring the adhesion energy per unit length E_a and the peeling stiffness of the nanotube $k_{\mathrm{CNT}}^{\mathrm{peeling}}$. In chapter 5, I will present that though the adhesion energy per unit length varies on different surfaces, the inferred diameters of the nanotube is of the same order.

4.4 Summary

Let us summarize the main points of this chapter : we perform a series of experiments where a single wall carbon nanotube is pushed perpendicularly against a surface, we record the adhesion force as a function of the compression. A main feature that the force curves presents is it exhibits a plateau at some range of compression. We propose a time-frequency analysis method by monitoring the resonant frequency shift of the cantilever, this allows accessing to the peeling stiffness of the nanotube at any compression during retraction process.

Elastica model is used to described the adsorbed nanotube on substrate, adhesion energy per unit length E_a is used to describe the strong interaction between the nanotube and the surface, R_a the radius of curvature of the first contact point during a nanotube's adsorption is also defined. Theoretical description of the adsorption of nanotube is used. It illustrates that the measured force plateau is equivalent in the absolute value to the adhesion energy per unit length E_a. Two boundary conditions are proposed to described the peeling mechanism of the peeling point : torque free origin and clamped origin. The following numerical simulations indicate that the two boundary conditions exhibit opposite force behaviors at the defect where the nanotube is peeled. The experimental measurement of the adhesive force valid the torque free origin being a more realistic condition to describe the adhesion where the peeled part of nanotube include defects.

The adhesion energy per unit length E_a is measured from the force plateau, the peeling stiffness $k_{\mathrm{CNT}}^{\mathrm{peeling}}$ is obtained by time-frequency analysis method. The mechanical properties of the nanotube is then inferred by E_a and $k_{\mathrm{CNT}}^{\mathrm{peeling}}$: R_a, EI, and diameter of peeled nanoutbe D_{CNT} .

Chapitre 5

Substrate dependence of adhesion energy E_a

Contents

5.1 Questions to probe

As discussed in chapter 4, during the peeling of a single walled carbon nanotube, measuring the adhesion force and the derived peeling stiffness $k_{\mathrm{CNT}}^{\mathrm{peeling}}$ can provide access to the intrinsic properties of the nanotube. On various surfaces, is there any difference in the adhesion energy ? Are the inferred intrinsic properties of the nanotube independent of the substrate ? We will focus on answering these questions in this chapter.

5.2 Substrate preparation

For the substrates, graphite and mica are first chosen as candidates as a fresh layer is always easy to be cleaved before the test. The interaction between the layers is dominated by Van der Waals forces. For the other substrates, we will choose several metallic surfaces of gold (Au), aluminum (Al), silicium (Si), and platinum (Pt) to conduct the peeling test to investigate relative adhesion energies.

For the adsorption of the nanotube on substrate, a very flat surface is indispensable in order to get rid of the impact from the morphology of the surface. We choose to work on the chip of commercial AFM cantilevers coated with Au, Al, Pt, and without any coating (thus Si). In the test, we approach the nanotube to the chip of the chosen cantilevers. Their millimetric surface is flat and clean to test the adhesive peeling. Before the test, all metallic samples undergo a treatment in an ultrasound

cleaner in ethanol for 10 mins, isoproponal for 10 mins, then in a plasma cleaner (medium power) for 10 mins to avoid any contamination from outside environment. Then are kept in clean and dry containers for 6 hours to decrease the surface impact that might be changed by the cleaning process.

5.3 Force measurement

On graphite, we record the force as a function of compression by approaching and retracting the nanotube, the measured force curve is plotted in figure 5.1. Blue, red, and black curve correspond to approach, retract, and standstill state of the piezo. An obvious hysteresis due to the adhesive force can be noticed. The interaction is mostly attractive, hinting at an adhesive force dominated peeling process. In the figure, we can easily read out two long force plateaus around 300 nm$< z_c <$550 nm, another one around 100 nm $< z_c <$ 250 nm with a smaller value. This value of the force plateau is equivalent to adhesion energy per unit length E_a according to the previous discussion. The different values of the plateau detected here link to different segments of the nanotube with different diameters (e.g. a loop from each side for this nanotube).

The piezo ramp used here is specially designed compare to a normal ramp : normal approach but slow retraction, this leads to a very high resolution of attractive force curve. This special ramp allows us to perform time-frequency analysis thereafter to obtain more precise information about the dynamic stiffness of the tube. One defect located at around z_c =630 nm can be figured as at this compression the force exhibits a big negative force, the feature measured here once again valid the fact that torqued free origin describes the adsorption of nanotube in a more realistic manner.

With this special ramp of the piezo, we can stay a sufficient time at any compression to perform a precise time-frequency analysis for this CNT on graphite. The results are plotted in figure 5.2. The resonance frequency of the cantilever is obviously shifted on the plateau 300 nm$< z_c <$550 nm during the retraction of the piezo (the cyan dotted line indicates the resonant frequency f_0 of the cantilever before contact). The corresponding dynamic stiffness of the nanotube on this plateau is clearer than that in figure 4.11. The long plateau (as black arrow indicates in the figure) allows us to compute easily the averaged dynamic stiffness to a more trustable level with respect to that of used normal ramp (figure 4.11) : k_{CNT} =0.46±0.05 N/m.

We plot a typical force curve on substrates of graphite, Pt mica, Au, Al, and Si in figure 5.3 : the features of the force curves tend to be similar though on different surfaces. It is reasonable since the measured force curve reflects the intrinsic structure of the nanotube, and always the same nanotube is used in these tests. The value of the force plateau on these substrates is different, that is to say, the adhesion energy per unit length E_a depends on the substrate. The measured adhesion energy and the inferred dynamic stiffness k_{CNT} on these 6 surfaces are listed in details in table 5.1 : the adhesion energy per unit length E_a for various substrates is of the

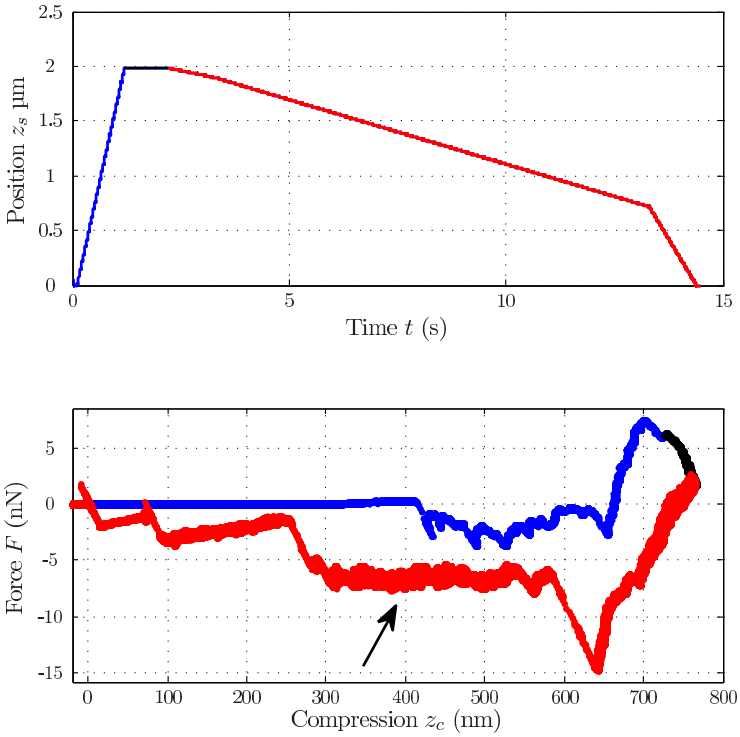

FIGURE 5.1 – Measured force curve (down) F vs. compression z_c on a graphite substrate. The strong hysteresis due to the adhesion can be noticed between approach (blue curve) and retraction (red curve). The black arrow indicates the longest force plateau from 300 nm to 550 nm on the force curve.

same order of magnitude though the value for graphite, Au, mica are generally larger than that for Al, Pt, and Si. Note that, E_a for graphite is around 1.6 times larger than that for mica, which is almost in line with our previous measurement [125] (2 times larger). The absolute value though is different since it corresponds to different growth conditions (previous nanotubes were prepared by A. M. Bonnot in Grenoble).

Substrate	graphite	mica	Au	Al	Pt	Si
E_a (nJ/m)	6.60±0.39	4.20±0.40	5.07±0.76	3.77±1.04	3.22±0.39	3.05±0.48
$k_{\mathrm{CNT}}^{\mathrm{peeling}}$ (N/m)	0.46±0.05	0.28±0.04	0.40±0.08	0.26±0.07	0.21±0.03	0.21±0.04
R_a (nm)	34±4.3	36±6.1	30±7.5	35±13.6	37±6.8	35±8.7
EI (10^{-24} Jm)	15.8±4.5	11.0±4.4	9.5±5.7	9.2±9.2	8.8±4.0	7.5±4.6
D_{CNT}(nm)	4.9±0.8	4.4±1.0	4.1±1.4	3.8±1.3	4.0±1.0	3.8±1.3

TABLE 5.1 – Measured values of the adhesion energy per unit length E_a, dynamic stiffness of the nanotube $k_{\mathrm{CNT}}^{\mathrm{peeling}}$, natural radius of curvature R_a, bending modulus EI, and inferred diameter R_a of the adsorbed nanotube.

According to the discussion (4.38), from the inferred dynamic stiffness and the adhesion energy, we can estimate directly the radius curvature R_a and the bending

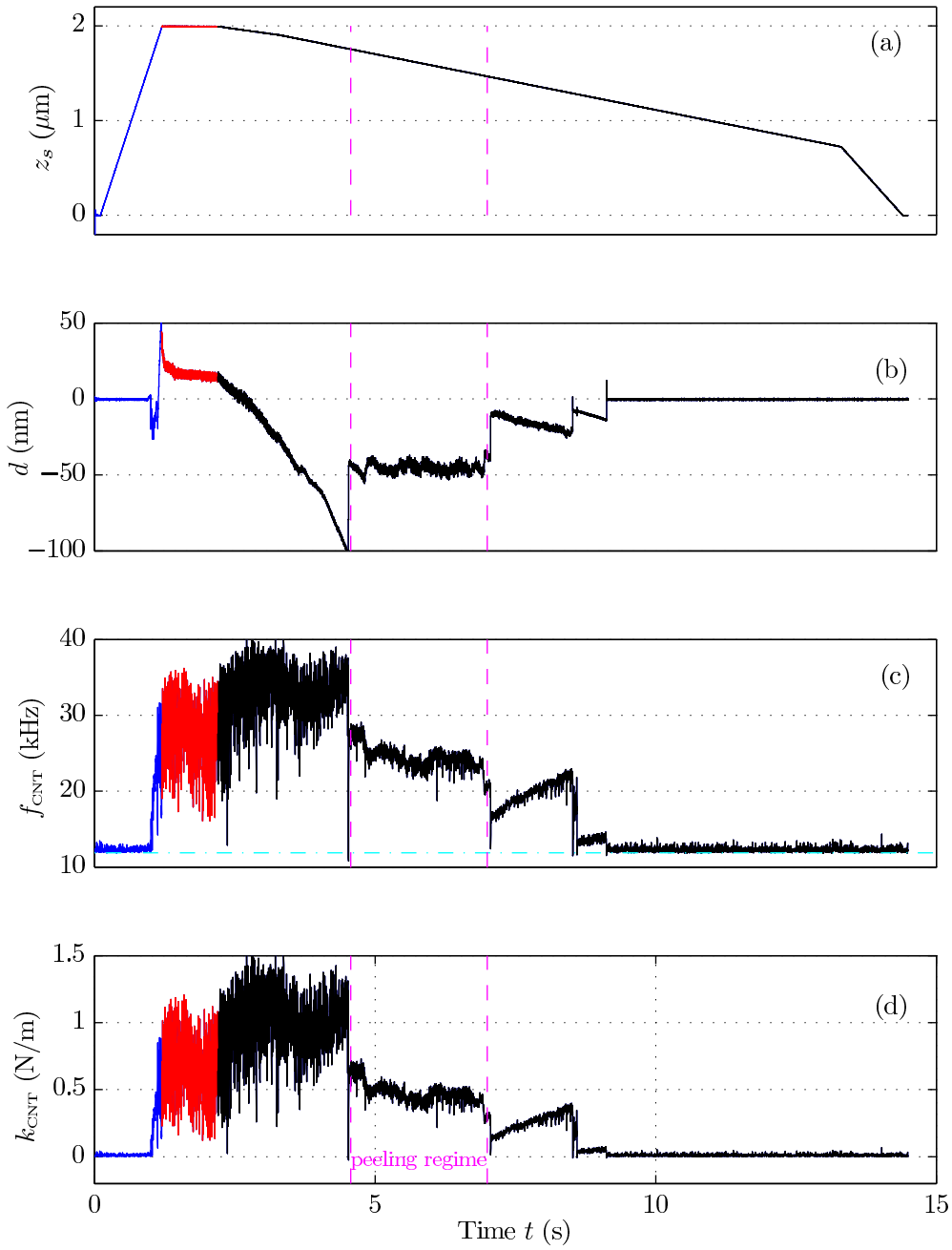

FIGURE 5.2 – Time evolution of the piezo position z_s (**a**), deflexion d (**d**), resonant frequency f_{CNT} (**c**) and dynamic stiffness of CNT k_{CNT} (**d**) during a specially designed approach-retract cycle. The color blue, red, and black lines indicates the approach, rest, retract translation of the piezo. The dotted cyan line in (**c**) indicates the resonant frequency of the cantilever in out of contact state to give a comparison with that in contact f_{CNT}. The longest plateau of figure 5.1 corresponds to the time interval 4.5 s-7 s, which we use to compute the adhesion and intrinsic properties of the nanotube in the peeling regime.

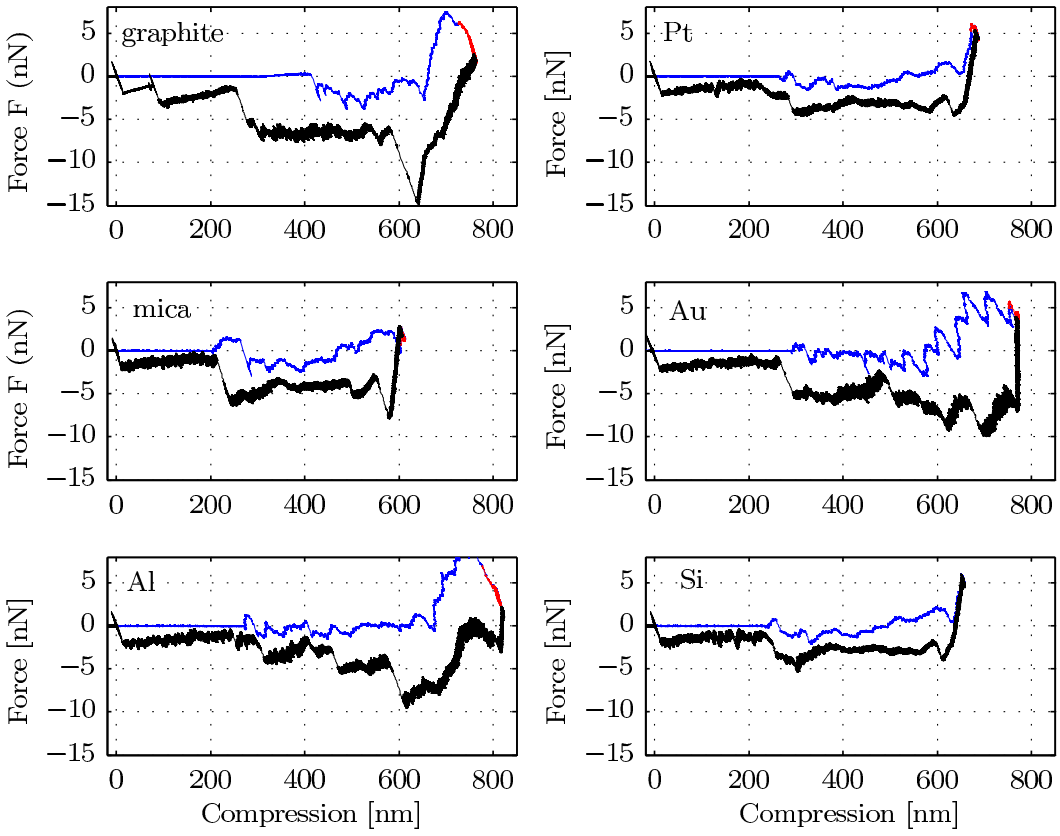

FIGURE 5.3 – Measured force curves on various substrates : graphite, Pt, mica, Au, Al, and Si as a function of compression. We compute the value of E_a from the longest force plateau, around 300 nm to 500 nm.

stiffness EI of the nanotube when it is being peeled, we estimate in the end the diameter of the peeled CNT by equation (4.40). For all of the substrates, even though the adhesion energy and the dynamic stiffness varies, we obtain similar diameters of the nanotube on these substrates.

In the table 5.1 and figure 5.4, we report the adhesion energy and inferred diameters of the nanotube on these surfaces. Standard error bars are computed in different approach-retraction cycles on the same plateau. From the figure, we can clearly see that for these surfaces, the nanotube presents different amplitude of adhesion forces, specially for the graphite and the mica which differs by a factor of 1.6. However, the inferred diameters are 4.9 ± 0.8 nm for graphite, 4.4 ± 1.0 nm for mica. This is evidently in accordance with the independence on the substrates. Measuring the adhesion force and peeling stiffness allows access to the mechanical properties of the nanotube, this experimental data gives thus direct support to our previous discussion about the peeling process of the nanotube in the chapter 4.3.3.

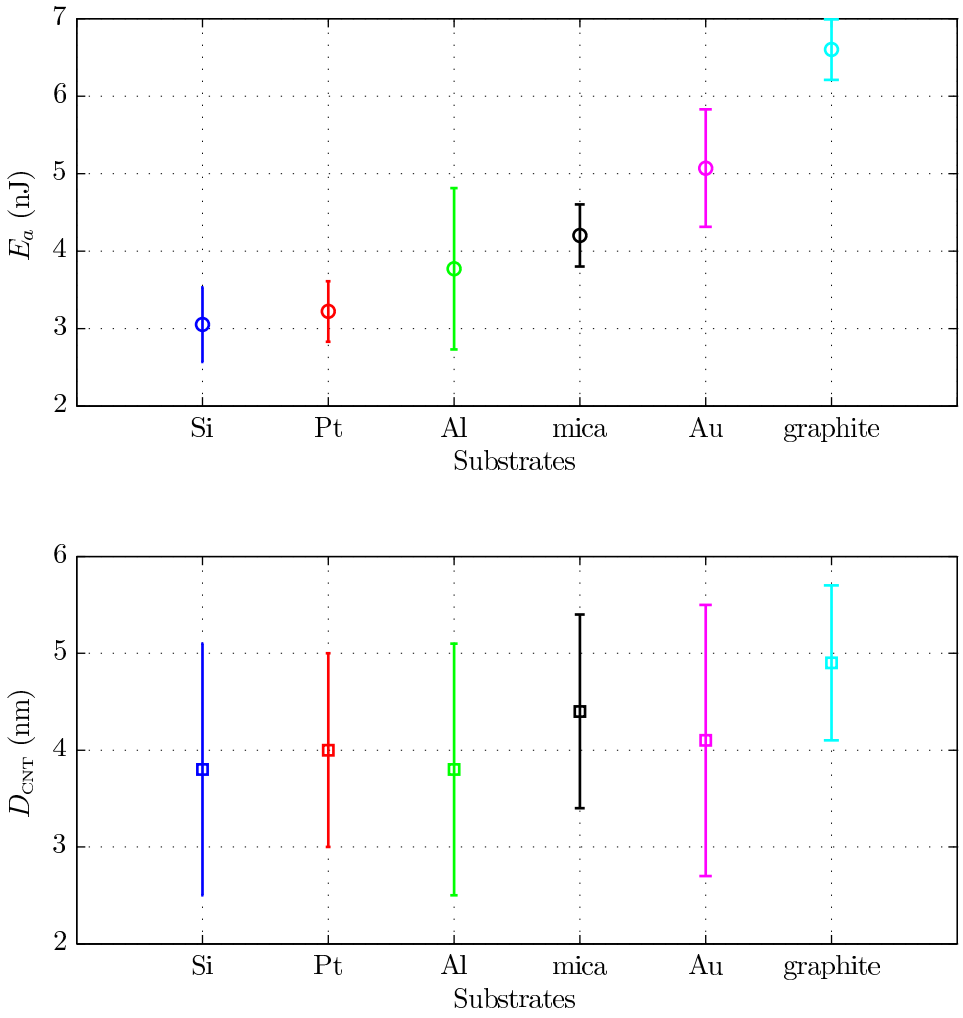

FIGURE 5.4 – The value of the force plateau on substrates (top) : graphite, mica, Pt, Au, Al and Si and (bottom) the inferred diameter of the peeled CNT by (4.38) and (4.40). The adhesion energy for various substrates differs, but the inferred diameters tend to be similar. This fully validates our previous discussion about the absorption of the CNT : we access both to its measured adhesion energy and to its mechanical properties. Error bars correspond to the stand deviation of the mean value of the plateau.

5.4 Calibration of the deflexion

As described in chapter 2, our home-made quadrature phase interferometric AFM is working with the sensing beam reflected on the free end of the cantilever and the reference beam on its flat base (figure 2.1). To make sure the sensing beam is always right on the tip, we scan the cantilever in a 2D map of reflected intensity with a interval of 10 µm in two directions of the cantilever plane (along and across the cantilever).

However, in some cases, the cantilever can be contaminated by materials that is less reflective, specially in the case of growing the nanotube on the cantilever by CVD, the by-products of the growth—amorphous graphite for instance, would decrease the reflectivity of the surface of the cantilever. It is thus usually hard to find precisely the end of the cantilever. Using the model presented in chapter 2, the cantilever is described in the Euler Bernoulli frame work. According to the solution of the equation of motion, the displacement of the tip is mode dependent : the deflexion d is changing according to the position of the laser spot with respect to the position of the nodes and antinodes of the mode. Therefore, the position of the laser spot can have an impact that is not negligible on the deflexion measurement, thus the force measurement. Related corrections should be taken into account, we present here two simple methods that are usually used for correction :

5.4.1 hard contact

When the cantilever is in hard contact with the substrate, the deflexion d should be equivalent to the translation of the surface linked to the piezo. That is to say, we will get a line with a slope equals to 1 in the plot of deflexion d vs. z_s. In case of the laser spot is not exactly on the end, the measured deflexion d is expected to have a smaller value, as indicated in figure 5.5. Let us define $d' = \alpha d$, the parameter α can be directly measured from the fit of blue (approach) or red (retract) line on the force curve of figure 5.6. The real deflexion of the tip is thus $d = d'/\alpha$, as plotted in black line in the figure. That means, the nearer to the tip, the closer the measured deflexion d' is to the real deflexion d.

The inset figure in the figure 5.6 illustrates the behavior of the zoomed deflexion, it is noticeable that there is an obvious 'jump' when the tip get or loose contact with the surface, which implies an adhesive force exists. This adhesive force is due to the interaction between the tip and the surface. The interaction leads to an small hysteresis during the retraction. With parameter α being subtracted, the real deflexion of the tip can be compensated as plotted in black line in the figure 5.6.

Using the hard-contact trick to calibrate the cantilever is common for commercial AFM setup, it is also used in our next chapter (chapter 6) when we want to calibrate a piezo that is used to apply excitation to the nanotube. However, as in this method we need to push the tip against to the surface, in the case of a functionalized tip with a single wall carbon nanotube, the hard contact has thus the risk of harming the nanotube, for this reason, I would like to introduce another safer calibration way by using the normal modes according to the description of Euler Bernoulli.

5.4.2 stiffness

The measured force is computed by multipling the stiffness with the deflexion of the cantilever : $F = kd$. If the laser spot is not focus right on the end, the estimated force is $F' = k'd'$. Let us recall the equipartition theorem, when the cantilever is in equilibrium with the outside environment, the energy stored in the spring is in

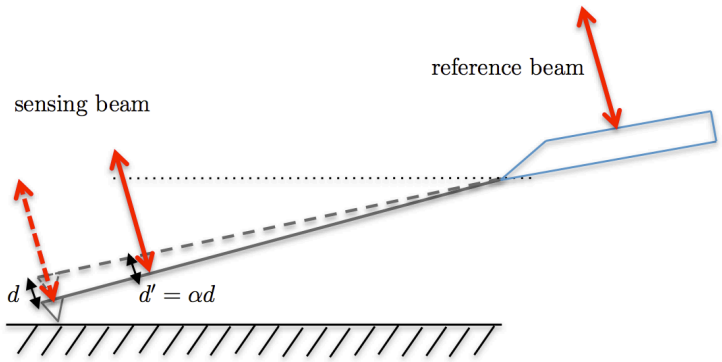

FIGURE 5.5 – Schematic diagram of cantilever in hard contact.

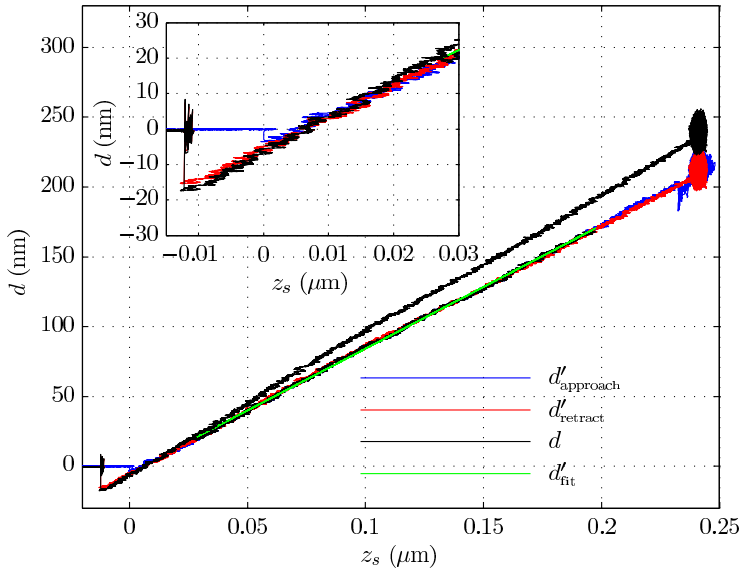

FIGURE 5.6 – Deflexion d as a function of the position of piezo z_s in hard contact, the inset figure illustrates the area where the cantilever tip get and loose contact with the surface. By fitting the curve (red), the real deflexion of the cantilever can be given by $d = d'/\alpha$.

average equal to the thermal noise :

$$\frac{1}{2}k\left\langle d^2\right\rangle = \frac{1}{2}k_B T \tag{5.1}$$

where k is the spring constant of the cantilever, $\left\langle d^2\right\rangle$ the mean quadratic deflexion, k_B the Boltzmann constant and T the temperature. We have been using this formula to calibrate the cantilever's stiffness according to the FDT.

For the laser spot positions right in the end (deflexion d) and not (deflexion d'), we have according to our calibration procedure :

$$\frac{1}{2}k\left\langle d^2\right\rangle = \frac{1}{2}k_B T = \frac{1}{2}k'\left\langle d'^2\right\rangle \tag{5.2}$$

We thus have :

$$k' = k\left(\frac{\Phi_1(L)}{\Phi_1(x)}\right)^2 \tag{5.3}$$

The true (d) and measured deflexion (d') are linked to the shape $\Phi_1(x)$ first mode of oscillation of the cantilever considered here :

$$d' = d \times \left(\frac{\Phi_1(x)}{\Phi_1(L)}\right) \tag{5.4}$$

where x is the coordinate of the laser spot on the cantilever. It leads to :

$$F' = k'd' = k\left(\frac{\Phi_1(L)}{\Phi_1(x)}\right)^2 \frac{\Phi_1(x)}{\Phi_1(L)}d \tag{5.5}$$

thus,

$$F = F'\sqrt{\frac{k'}{k}} \tag{5.6}$$

The true stiffness k is calibrated before the growth of the nanotube. By measuring the force F' at position x and the corresponding stiffness k', we can thus estimate the real force F that could be measured if the laser spot was right on the end of the cantilever. This calibration is critical when one wants to compare the adhesion energies on various substrates, this is because when we change the substrate from one to another, slight shifts on the laser position on the cantilever are introduced even with very careful manipulation. In addition, the value of adhesion energy among various substrates are on the same order of amplitude, any tiny fluctuation in stiffness can cause incorrect results of the comparison. By such calibration, we can get a reliable comparison of the forces on these substrates. The force measured in figure 5.4 has been calibrated by this method.

5.5 Summary

We measure the adhesion force when a single wall carbon nanotube is approached perpendicularly against and retracted off a flat surface on various substrates. With

a specially designed ramp (normal approach but slow retraction), we have sufficient time to perform precise time-frequency analysis of the deflexion of the cantilever, and get access to the dynamics stiffness of the nanotube during the peeling test. In the force curve, a long force plateau presents the most striking feature of the curve, the value of which is equivalent to the adhesion energy per unit length. It exhibits substrate dependence.

Within the framework previously discussed, measuring the adhesion energy per unit length and the peeling stiffness of the nanotube lead directly to the mechanical property of the nanotube. We measured the adhesion energy on substrates of graphite, mica, Au, Al, Pt and Si, the results unveil that the E_a for graphite, mica and Au are generally larger than for Al, Pt, and Si. The adhesion energy on the graphite is twice larger than that on Si. After performing time-frequency analysis of the measured deflexion for all of the substrates, we go further to estimate the diameters of as peeled nanotube : though the adhesion energy differs on substrates, the estimated diameters are similar, all in accordance with the fact that the same nanotube is peeled in these tests.

Chapitre 6

Dynamic peeling stiffness of CNTs

Contents

As presented in chapter 4, the measured force plateau F directly gives the adhesion energy per unit length E_a, combining with the peeling stiffness $k_{\mathrm{CNT}}^{\mathrm{peeling}}$, we can get access to the mechanical properties of the nanotube (EI, D_{CNT}). In chapter 5, adhesion energy E_a of a peeled nanotube on various substrates are measured, the results shows that E_a is surface dependent.

6.1 Peeling stiffness of CNT

In this chapter, we will focus our investigation on the peeling stiffness of the nanotube when it is retracted away from the surface. We plot the force curve of one of the grown nanotube as a function of compression z_c in approach-retract cycle in the figure 6.1. The force curve exhibits an obvious long force plateau for compressions from $z_c = 70\,\mathrm{nm}$ to $220\,\mathrm{nm}$. This flat force plateau lead thus to zero peeling stiffness of the nanotube since it implies :

$$\mathrm{d}F/\mathrm{d}z_c = 0 \tag{6.1}$$

Even if we take into account the details of the force plateau (which is not perfectly flat), we have an upper limit around 10^{-2} N/m for the static stiffness.

When we apply time-frequency analysis of the deflexion by equation (4.3) as we did in the figure 4.10, and plot the results in figure 6.2. The peeling stiffness is obviously a non-zero value : $k_{\mathrm{CNT}}^{\mathrm{peeling}}$ is around $0.06\,\mathrm{N/m}$. The question soon arises :

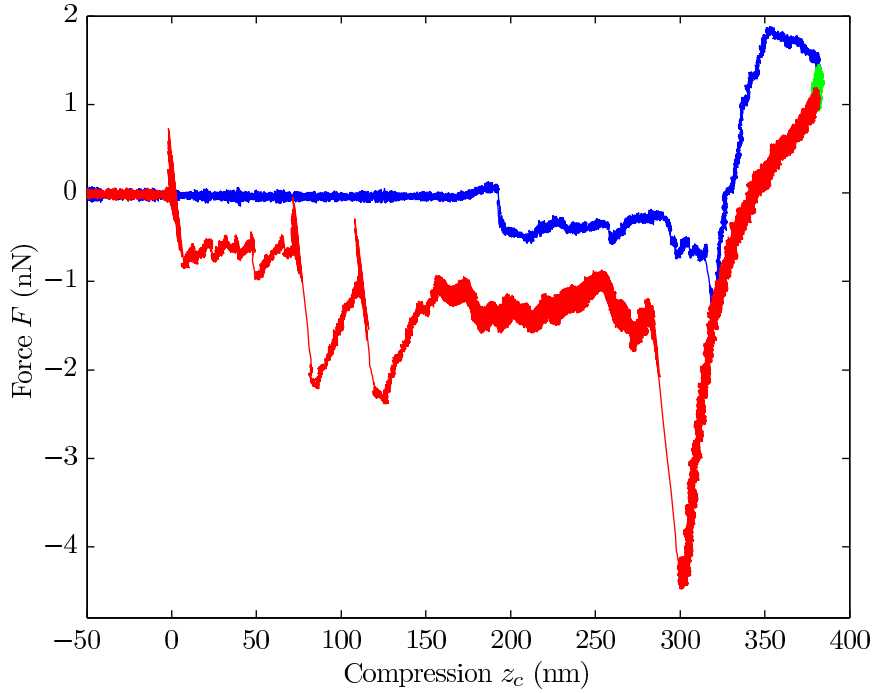

FIGURE 6.1 – Forve curve vs. compression z_c of a nanotube with few defects.

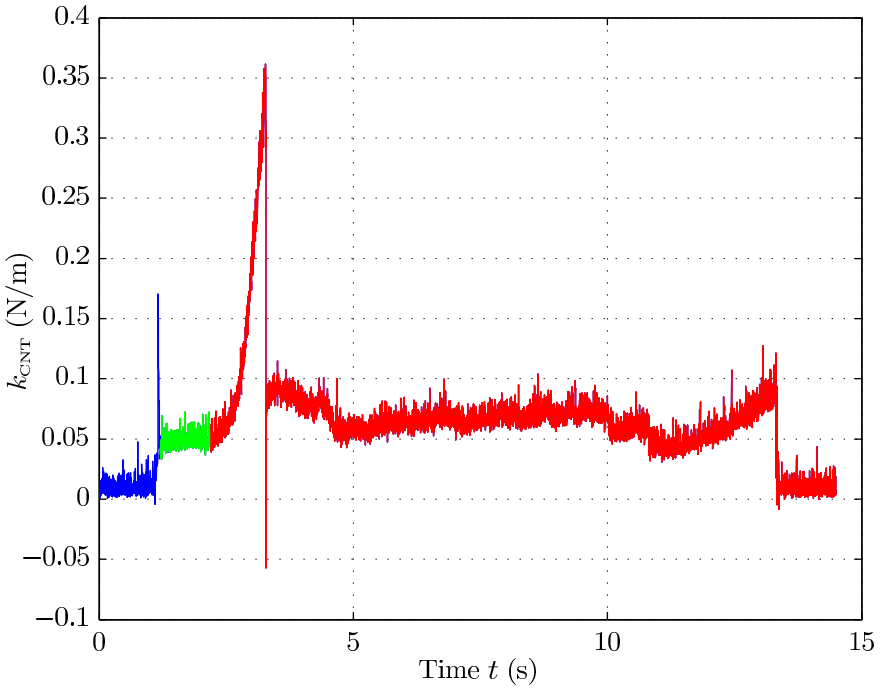

FIGURE 6.2 – Dynamic stiffness of the nanotube estimated by time-frequency analysis of the deflexion of the cantilever. On the force plateau, the peeling stiffness is obviously a non zero value.

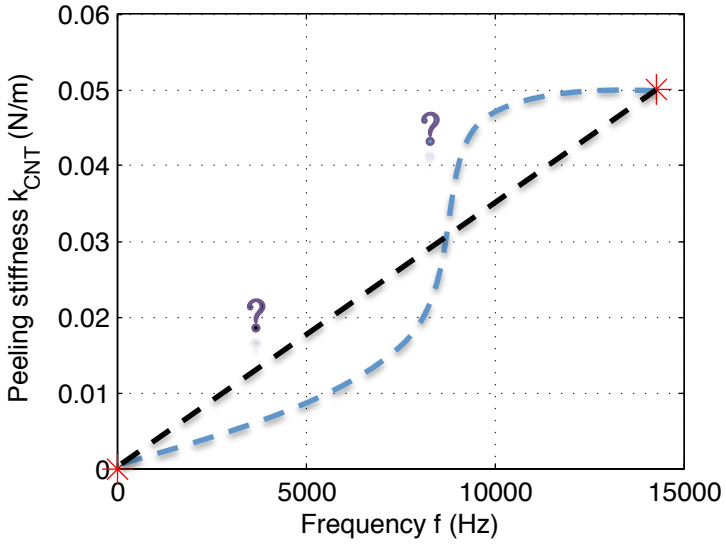

FIGURE 6.3 – The question being probed in this chapter : the characteristic of the peeling stiffness from low frequency to high frequency.

Why does the peeling stiffness of the CNT exhibit different behaviors using different estimation method ? Is this a contradiction ?

Let us go back to recall the computation process of the $k_{\mathrm{CNT}}^{\mathrm{peeling}}$: the resonant frequency of the power spectrum density (PSD) of fluctuation is used to compute the frequency shift : $f_0 \rightarrow f_{\mathrm{CNT}}$ from out of contact to in contact. They are measured in frequency range of $(10 - 15)$ kHz on PSD of thermal noise induced deflections. The answer might be like : the adhesion can be a slow process, high frequency thermal noise will only probe the response of the free standing part of the nanotube, the adsorbed length acting like a rigid clamping at fast time scales. With such an assumption, questions are further proposed as shown in figure 6.3 : how does the peeling stiffness depend on the probing frequency ? Is there any characteristic time scale ? What is dissipation like during this adhesive process ? It is undoubtly interesting to probe this dynamic peeling stiffness of the nanotube and its relative dissipation process at different time scales.

6.2 Experiment configuration

The configuration of the experiment is shown in figure 6.4. Besides the piezo (1) that is used to perform the normal ramp, a new piezo (piezo (2)) is added to the setup. It is mounted on top of the support by a metallic plate, magnetically connected. A fresh cleaved mica substrate is then carefully mounted on the top side of the piezo. An elastic fork is designed to supply a uniform force to push the mica and piezo on both sides to the metallic plate. The reason why we choose this complicated configuration rather than using directly an double sided adhesive tape

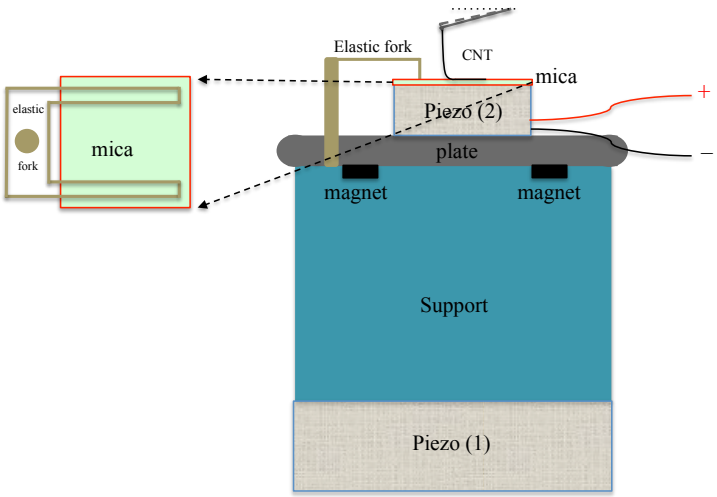

FIGURE 6.4 – Scheme of excitation experiment (right) and the top view of the substrate mica (left). The mica and the piezo are strongly pushed by a designed elastic fork to the metallic plate, without any adhesive tape that might be add inertia is involved.

to link the mica and the piezo or the piezo and the metallic plate is that the adhesive tape acts as an additional spring. It can reduce the response of the piezo, especially at high frequency in our case, thus getting rid of it in this small response system is critical to get a response at high frequency. Due to the similar reason, we use the piezo(2) rather than the piezo(1) to add the excitation because of the huge mass of the support the piezo (1), causing too much inertia to reach high frequencies. Piezo (2) needs of course to be calibrated to get its response before being used. In this chapter, I will introduce a simple way to conduct the calibration.

We use the similar calibration process of the photodiode sensitivity : to calibrate the piezo, we just need to push a normal cantilever without nanotube against to the substrate, then we apply the same voltage as we are going to apply for peeling test.

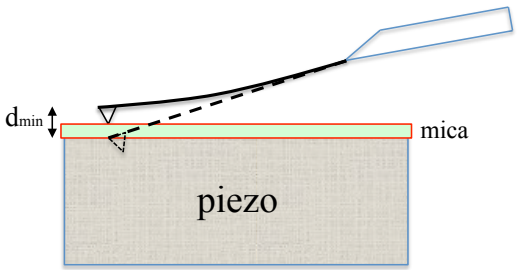

FIGURE 6.5 – The schematics of calibration of piezo by hard contact. To avoid being lagged by the displacement of the piezo at high frequency, the cantilever is pushed by a minimum distance $d_{\min}$ which is determined by the resonant frequency f_0 of the cantilever and upper bond of the frequency one wants to probe.

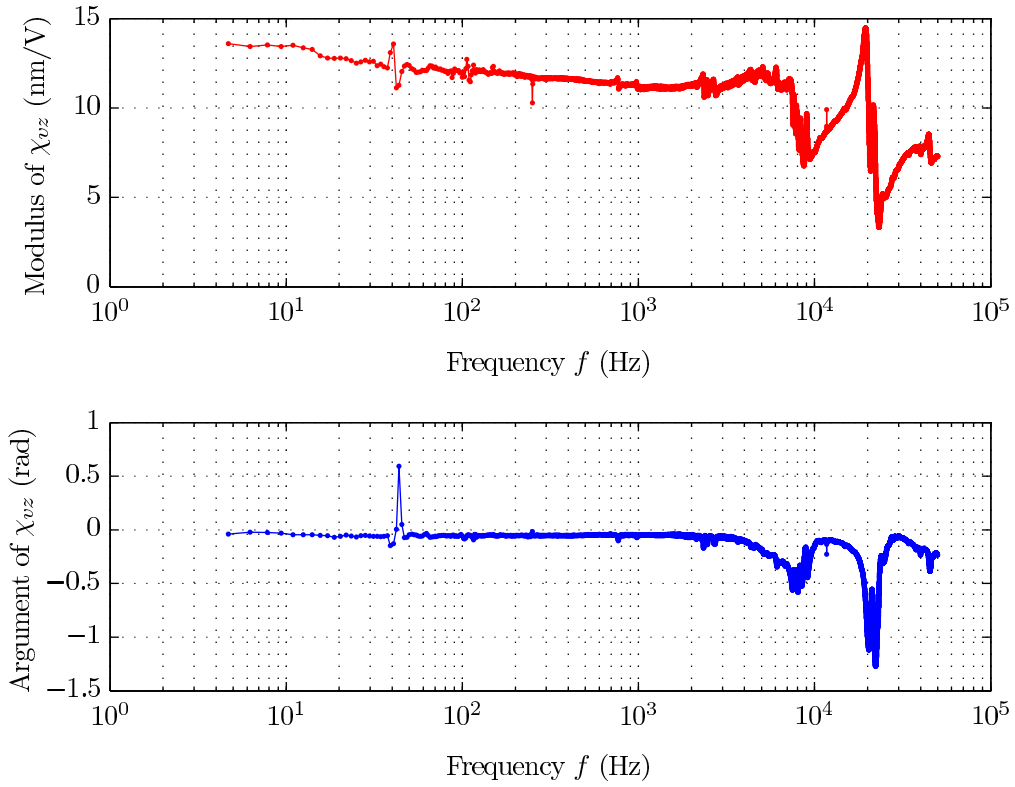

FIGURE 6.6 – Modulus and argument of transfer function χ_{vd} when mica layer, piezo, and the support are connected by double sided adhesive tape. The adhesive tape in between behaves as a spring leading to less response of the piezo at high frequency (f>2 kHz).

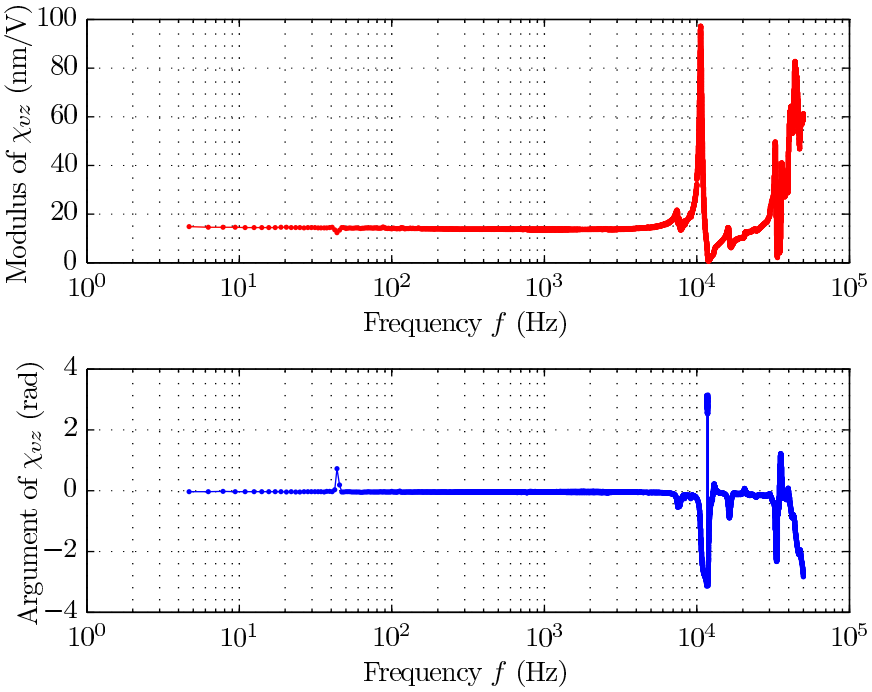

FIGURE 6.7 – Modulus and argument of transfer function χ_{vd} when using the designed fork. The response is flat up to 6 kHz.

As the tip of the cantilever is in hard contact with the surface, any movement of the surface can be directly followed by the tip, and recorded by the interferometer : $z_s = d\cos\theta_{\text{AFM}}$. With a minimum push distance $d_{\min}$, we measure this way the response of that piezo with respect to the excitation voltage.

Note that using a minimum pushing distance $d_{\min}$ (illustrate in figure 6.5) is important to calibrate the piezo by hard contact since at very high frequency, the tip of the cantilever may not follow the displacement of the piezo due to lack of enough acceleration. The minimum value of distance $d_{\min}$ can be simply computed when the acceleration of the excitation signal is equivalent to that of the tip. Supposing the excitation signal we use is $z_s = A\sin(\omega t)$, then $\ddot{z_s} = -A\omega^2\sin(\omega t)$, where A is the amplitude of the signal. For the tip, according to Newton's second law, the maximum acceleration provided by the cantilever is $\ddot{d} = F_0/m = F_0\omega_0^2/k = d_0\omega_0^2$, where d_0 is the average deflexion. We therefore get the minimum pushing distance d_{min}, it is related to amplitude of excitation, resonant frequency of the cantilever and the upper bond of the frequency one wants to probe :

$$d_{\min} = A\frac{\omega^2}{\omega_0^2} \tag{6.2}$$

For example, using a cantilever with a resonant frequency around 80 kHz, with a amplitude of excitation A =20 nm and a pushing distance of 70 nm, we can probe frequencies up to 150 kHz. To avoid large deflections, usually a cantilever with a large

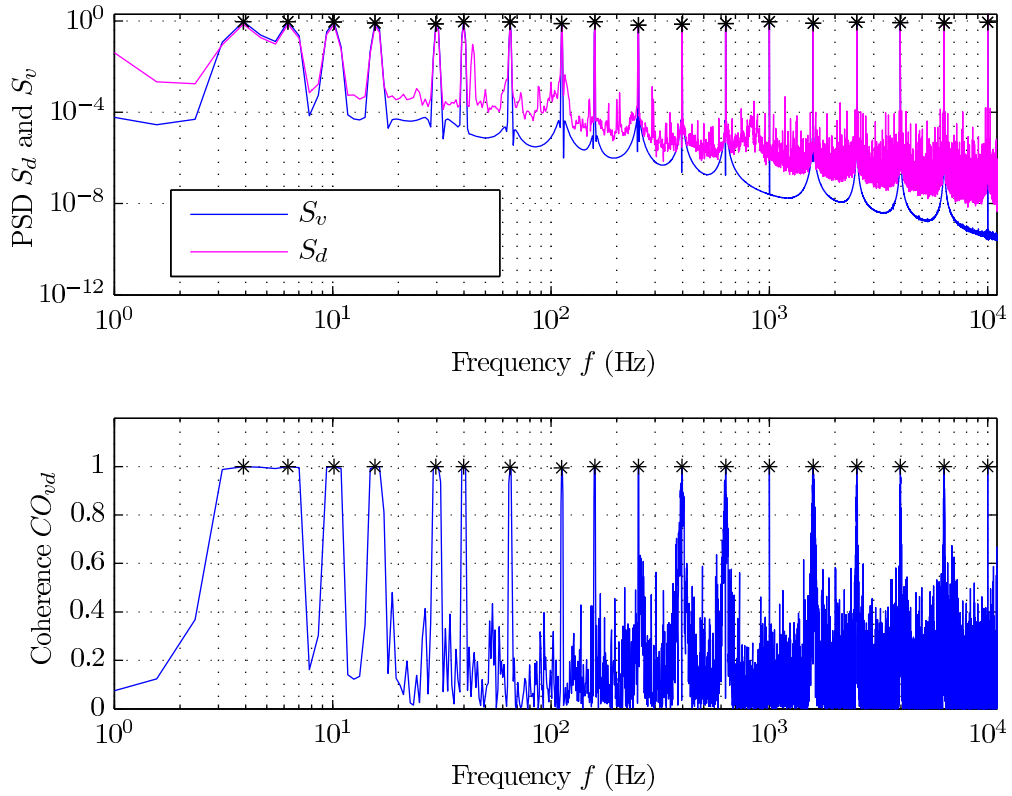

FIGURE 6.8 – (top) Power Spectrum Density (PSD) of the excitation signal v and the corresponding PSD of the deflexion d of the cantilever. (bottom) Coherence spectrum of the input 'excitation signal (v)' and the output 'deflexion of the cantilever (d)'. The black stars mark the frequencies that we use to perform the excitation.

spring constant is favorable to perform the calibration. As illustrated in figure 5.6, from the position where the tip get into contact with the piezo, a distance around 250 nm is further pushed to avoid any hysteresis with respect to the movement of the piezo at fast time scale.

In figure 6.8, we plot the Power Spectrum Density (PSD) of the excitation signal (v) and the deflexion of the cantilever (d) in hard contact. The discrete frequencies at f =4 Hz, 6 Hz, 10 Hz, 16 Hz, 30 Hz, 40 Hz, 65 Hz, 112 Hz, 158 Hz, 251 Hz, 398 Hz, 631 Hz, 1000 Hz, 1585 Hz, 2512 Hz, 3981 Hz, 6310 Hz, 10 000 Hz are chosen to conduct the excitation, these frequencies are also the ones we will use later to excite the carbon nanotube. As it can be seen in the figure, the piezo can well respond to the applied signal up to 10 kHz. The absolute value of the coherence function between the input 'excitation signal (v)' and the output 'deflexion of the cantilever (d)' is close to 1, as is shown in the figure (bottom), indicating high consistently between the input and the output signal. The transfer function from excitation to the deflexion can thus be expressed as :

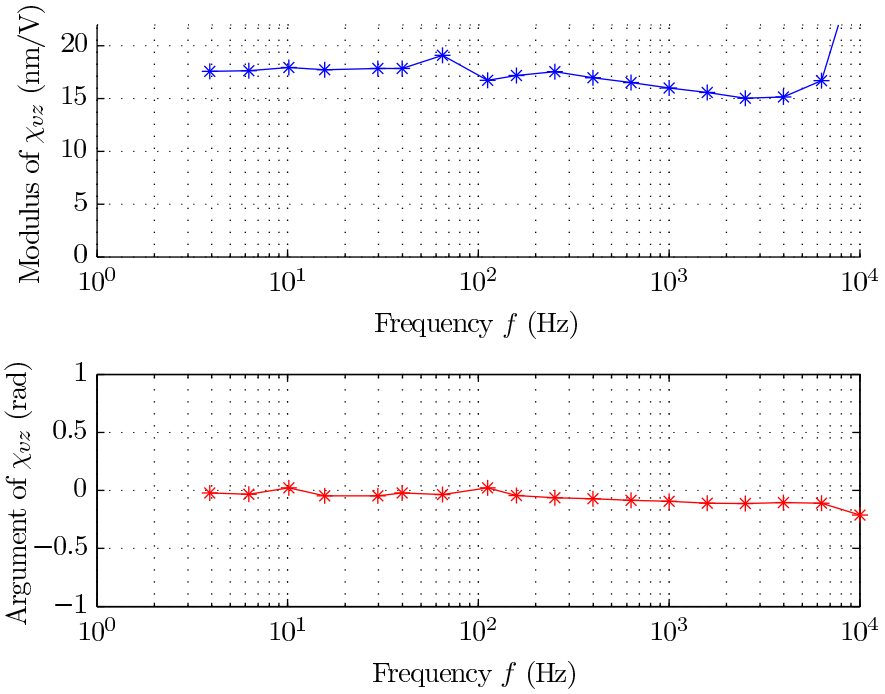

FIGURE 6.9 – The modulus of the transfer function χ_{vz} (up) and corresponding phase (down), probed on discrete frequencies.

$$\chi_{vz}(\omega) \equiv \frac{\hat{z_s}(\omega)}{\hat{v}(\omega)} = \frac{d(\omega)}{v(\omega)} \cos\theta_{\text{AFM}} \tag{6.3}$$

where $\hat{z_s}(\omega)$ and $\hat{v}(\omega)$ are the transformation in Fourier space of the excitation $z_s(t)$ and $v(t)$.

We plot the modulus of the transfer function χ_{vz} (up) and its phase (down) in figure 6.6, 6.7 and 6.9. In figure 6.6 and 6.7, we use a chirp for the driving voltage $v(\omega)$, leading to a continuous measurement of χ_{vz}. In figure 6.9, we use a sum of discrete frequencies to measure χ_{vz}, corresponding to the signal we use later to measure the dynamic peeling stiffness. Before the frequency attains 10 kHz, the piezo can respond to the excitation with the amplitude close to 20 nm/V and the phase close to 0, showing it is being a little lagged with respect to the driving signal, that means the hard contact exhibit a trustable way to calibrate the actual response of the piezo to the voltage excitation.

Figure 6.6 and 6.7 indicates the difference in transfer function χ_{vd} from excitation v to deflexion d of the cantilever in the case of with and without adhesive tape. The figure 6.6 shows a gradually decreased amplitude of χ_{vd} with the increased of frequency, and shows a sign of lack of response when the frequency above 2 kHz. The similar thing is found in its argument when the frequency is above 2 kHz which means a larger hysteresis between the piezo and the cantilever. While for the piezo without tape as shown in the figure 6.7, the amplitude and the argument of χ_{vd} are

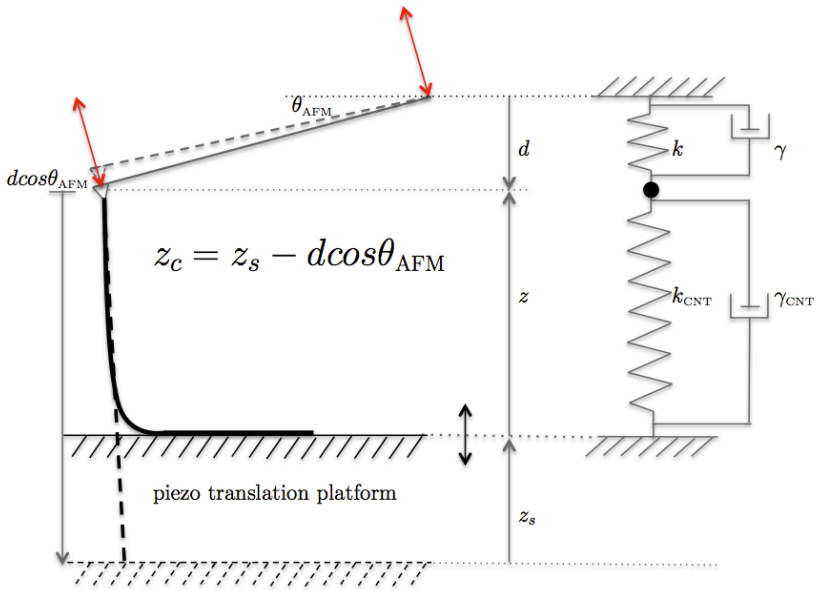

FIGURE 6.10 – Schematic diagram of the cantilever and the nanotube in contact when applying an excitation. The cantilever and the nanotube are modeled as two simple harmonic oscillators with spring constants k and k_{CNT}, and damping coefficients γ and γ_{CNT}.

flat up to 6 kHz.

6.3 Transfer function $\chi_{zd}(\omega)$

Since the zero peeling stiffness is derived from a quasi stationary process (peeling speed is around 10 nm/s), we can increase artificially the peeling frequency by adding a small amplitude oscillation to the sample position.

Before describing the measurement of the dynamic peeling stiffness of carbon nanotube, I want to introduce first the model that we use to describe the peeling test, where the cantilever tipped with a nanotube is peeled perpendicularly away from surface while an excitation is applied. The schematic diagram is shown in figure 6.10. The cantilever and the nanotube are modeled as two linked simple harmonic oscillators with spring constant k and k_{CNT}, damping coefficient γ and γ_{CNT}. k_{CNT} and γ_{CNT} describe the peeling stiffness and the dissipative process of the nanotube during the adhesive contact with the surface.

The equation of motion of the tip is written as :

$$m\ddot{d} = -kd - \gamma\dot{d} + \cos\theta_{\text{AFM}}(k_{\text{CNT}}z_c + \gamma_{\text{CNT}}\dot{z_c}) \tag{6.4}$$

where m is the effective mass of the cantilever and the tip, d the deflexion of the cantilever that can be directly recorded by the setup, z_c the compression of the nanotube : $z_c = z_s - d\cos\theta_{\text{AFM}}$, and θ_{AFM} the inclination of the AFM cantilever.

Since what we are interested in is the frequently response of the system when the nanotube is being peeled, we rewrite the equation (6.4) in Fourier space :

$$-m\omega^2 d = -kd - i\omega\gamma d + \cos\theta_{\mathrm{AFM}}[k_{\mathrm{CNT}}(z_s - d\cos\theta_{\mathrm{AFM}}) + i\omega\gamma_{\mathrm{CNT}}(z_s - d\cos\theta_{\mathrm{AFM}})] \tag{6.5}$$

As z_s and d can be directly measured in the setup, it is natural that we introduce the transfer function χ_{zd} of the system, it is defined as $\chi_{zd} = \hat{d}(\omega)/\hat{z_s}(\omega)$. we have thus the expression of χ_{zd} in the Fourier space :

$$\chi_{zd}(\omega) = \frac{K_{\mathrm{CNT}}(\omega)\cos\theta_{\mathrm{AFM}}}{K(\omega) + K_{\mathrm{CNT}}(\omega)\cos^2\theta_{\mathrm{AFM}}} \tag{6.6}$$

where K_ω and K_{CNT} are defined as :

$$\begin{cases} K(\omega) = k\left[1 - (\omega/\omega_0)^2\right] + i\omega\gamma \\ K_{\mathrm{CNT}}(\omega) = k_{\mathrm{CNT}}(\omega) + i\omega\gamma_{\mathrm{CNT}}(\omega) \end{cases} \quad with \;\; \omega_0 = \sqrt{\frac{k}{m}} \tag{6.7}$$

we simply rewrite the equation (6.6), and get the expression of K_{CNT} by :

$$K_{\mathrm{CNT}}(\omega) = k_{\mathrm{CNT}}(\omega) + i\Gamma_{CNT}(\omega) \tag{6.8}$$

$$= \frac{1}{\cos\theta_{\mathrm{AFM}} - \cos^2\theta_{\mathrm{AFM}}\chi_{zd}(\omega)} \tag{6.9}$$

The real part $k_{\mathrm{CNT}}(\omega)$ and the imaginary part $\Gamma_{\mathrm{CNT}}(\omega) = \omega\gamma_{\mathrm{CNT}}(\omega)$ of 6.9 are the peeling stiffness and the dissipation of the nanotube during the peeling process. Therefore, by measuring the transfer function of the system χ_{zd}, we can get access to the information about the peeling stiffness and the related dissipation of the nanotube during a peeling process.

6.4 Transfer function $\chi_{vd}(\omega)$

In the section 6.2, we presented a way to calibrate the piezo from our setup using hard contact. We obtain the transfer function from the excitation voltage v to the position z_s of the piezo χ_{vz}. When the CNT is in contact with substrate, the peeling stiffness and the dissipation of the nanotube are linked to the real part and the imaginary part of the transfer function χ_{zd} that we would like to measure. We excite piezo(2) with the same driving voltage as the previous section, but now with the nanotube in contact.

The corresponding deflexion of the cantilever is recorded, we get easily the transfer function from the excitation to the deflexion χ_{vd} :

$$\chi_{vd}(\omega) \equiv \frac{\hat{d}(\omega)}{\hat{v}(\omega)} \tag{6.10}$$

We plot in figure 6.11, the PSD of the excitation signal (top, blue curve) and the corresponding PSD of the deflexion of the cantilever (top, purple curve) that

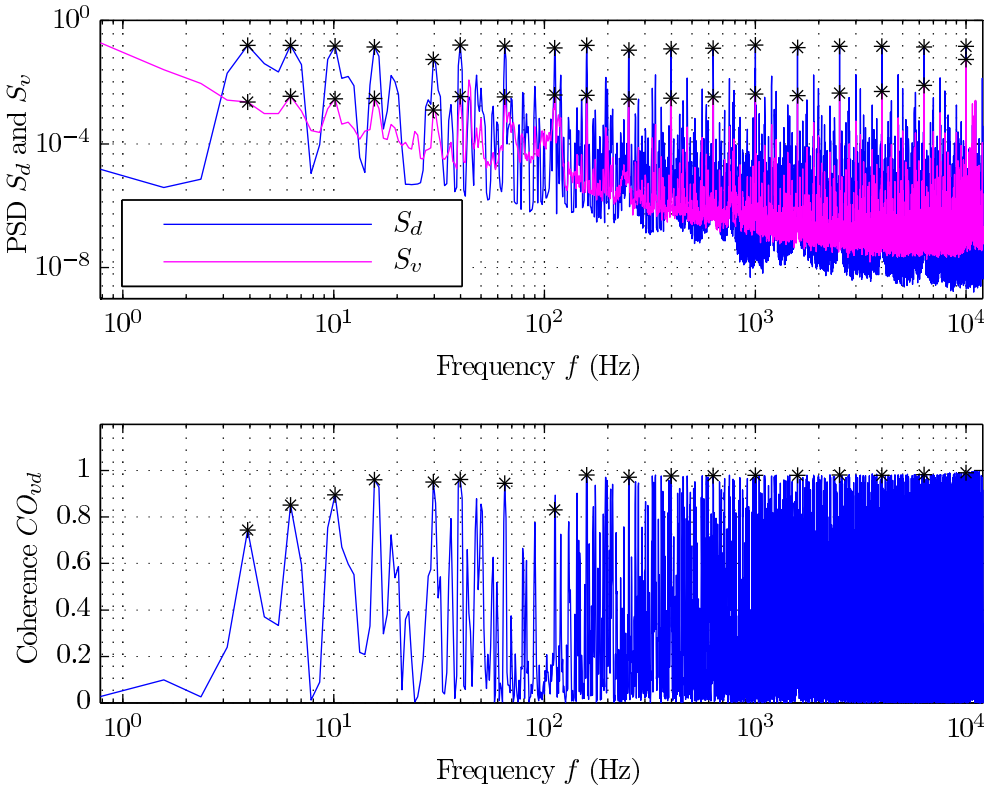

FIGURE 6.11 – Power Spectrum Density (PSD) of the excitation signal (top, blue curve) and the corresponding PSD of the deflexion for the cantilever (top, purple curve) that get in adhesion through the CNT. Coherence of the system with the input 'excitation signal' and the output 'deflexion of the cantilever' (bottom) . The black stars mark the frequencies that are used to perform the excitation.

gets in adhesion through the CNT, and the coherence of the system (bottom) with the input 'excitation signal' and the output 'deflexion of the cantilever'. Though it suffers some lost in amplitude, the coherence of the two signals still presents a high level. The black stars mark the discrete frequencies that we use to perform the excitation.

Therefore, combing with (6.3) and (6.10), the transfer function from displacement of surface z to the deflexion d of the cantilever is obtained by a simple division of the two expressions :

$$\chi_{zd} = \frac{\hat{d}(\omega)}{\hat{z}(\omega)} = \frac{\hat{d}(\omega)}{\hat{v}(\omega)} \frac{\hat{v}(\omega)}{\hat{z}(\omega)} = \frac{\chi_{vd}}{\chi_{vz}} \tag{6.11}$$

Reporting this measured value in equation (6.9) directly leads to the response of the contact $K_{\mathrm{CNT}}(\omega)$.

6.5 Dynamic peeling stiffness and dissipation of CNT

When the nanotube is pushed against and retracted away from the substrate, instead of using only a very slow peeling ramp (movement of piezo (1)), we add an excitation voltage with frequencies listed in the section 6.2 to piezo (2). Here, we choose to apply the voltage while the nanotube is being peeled rather than do it with a standstill nanotube is because the adhered part of the nanotube can easily drift during the experiment.

We therefore apply the excitation and perform the peeling test simultaneously. This way, we can extract the interesting information for every part of the nanotube, even including the part where defects exist.

In figure 6.12, we plot the time trace of the position of piezo (1), in parallel with the excitation voltage of piezo (2). We design a slow peeling ramp from $t = 3.3\,\mathrm{s}$ to $13.3\,\mathrm{s}$, where we peel the nanotube by only $100\,\mathrm{nm}$ in this example. The excitation voltage is the sum of 20 sinusoidal signals from $4\,\mathrm{Hz}$ to $100\,\mathrm{kHz}$, each having the same amplitude. The total amplitude of v is normalized in order to have a final peak-peak displacement of $20\,\mathrm{nm}$ for piezo (2). The corresponding force curve with excitation is plotted in figure 6.13.

We record the deflexion of the cantilever d during the excitation, we can compute the transfer function χ_{vd}. By equation (6.11), we obtain the transfer function from the displacement of the substrate to the response of the cantilever χ_{zd} (plus nanotube in contact). Using equation (6.9) finally, we compute the peeling stiffness and its dissipative part, that we will discuss in section 6.6. Since we perform this measurement during a very slow peeling ramp, we can even take small subsets of the ramp, and study the response at different location on the nanotube.

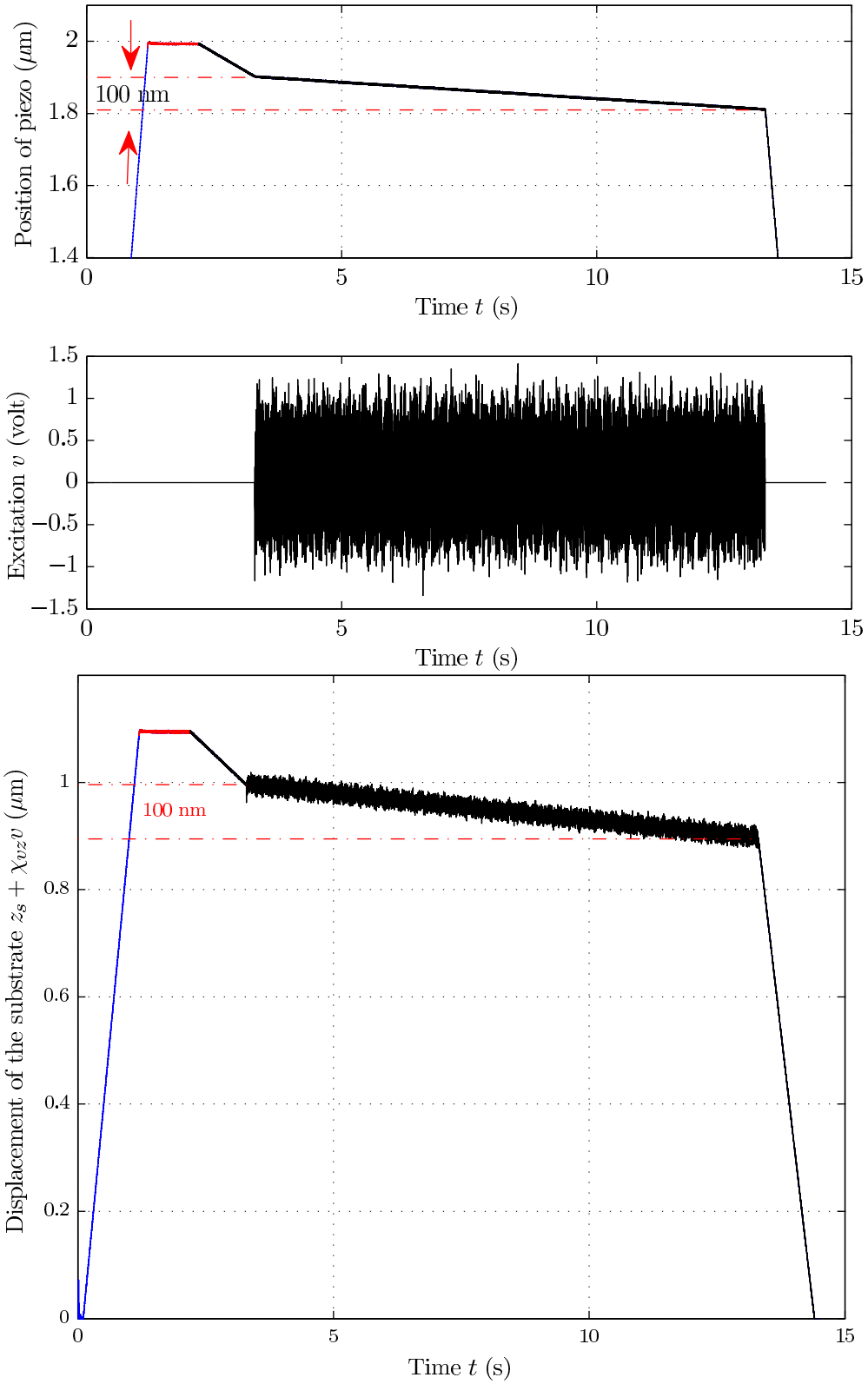

FIGURE 6.12 – Time trace of piezo (1) (top) : blue line, red line and black line are correspond to approach, rest and retraction process, respectively. (middle) the excitation signal as a function of time t. The excitation is applied only during the slow peeling process from 3.3 s to 13.3 s in time, around 100 nm in length of nanotube. (bottom) combination of time trace of piezo (1) and excitation signal as a function of time. Two signals are added by converting the unit of excitation to micrometer.

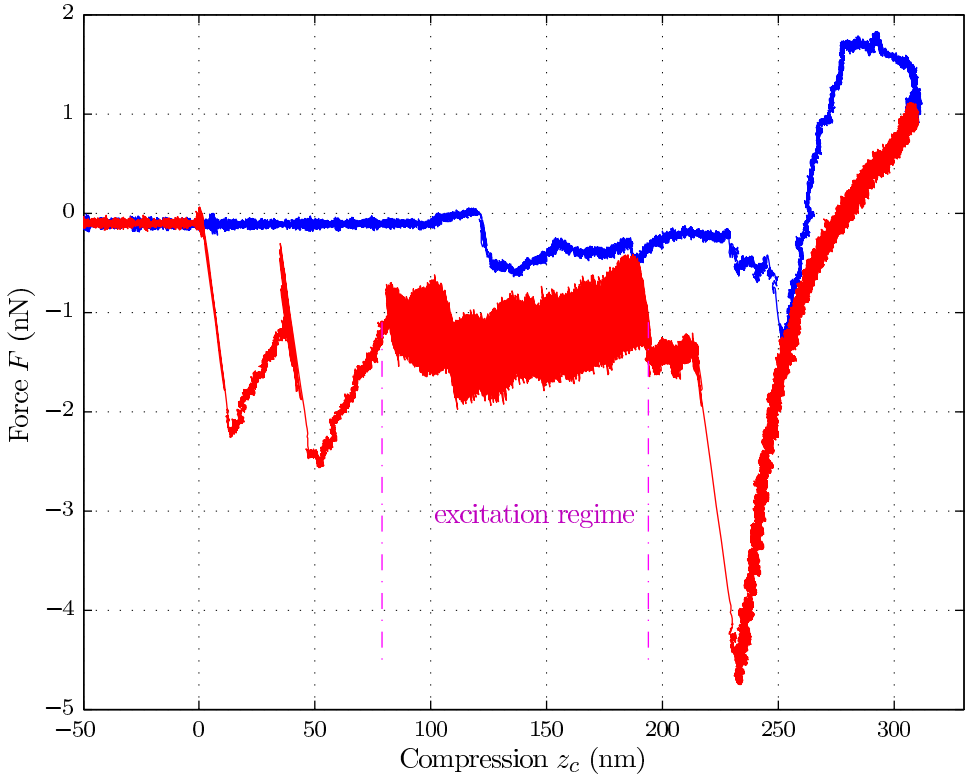

FIGURE 6.13 – Force curve as a function of compression with an excitation applied on the plateau of the nanotube. The length of excited plateau is around 100 nm.

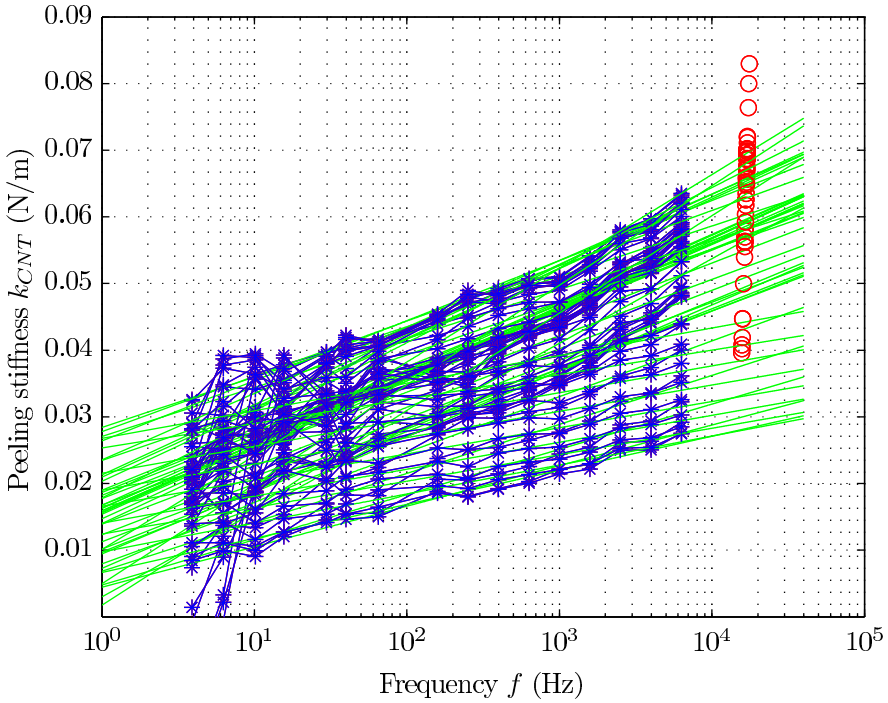

FIGURE 6.14 – Peeling stiffness of the CNT as a function of frequency for different position along the nanotube. k_{CNT} increases slowly with frequencies $f = 4\,\mathrm{Hz}$ to $f = 10\,\mathrm{kHz}$. The red circles mark the stiffness of the CNT computed by the time-frequency analysis of the deflexion of the cantilever driven by thermal noise.

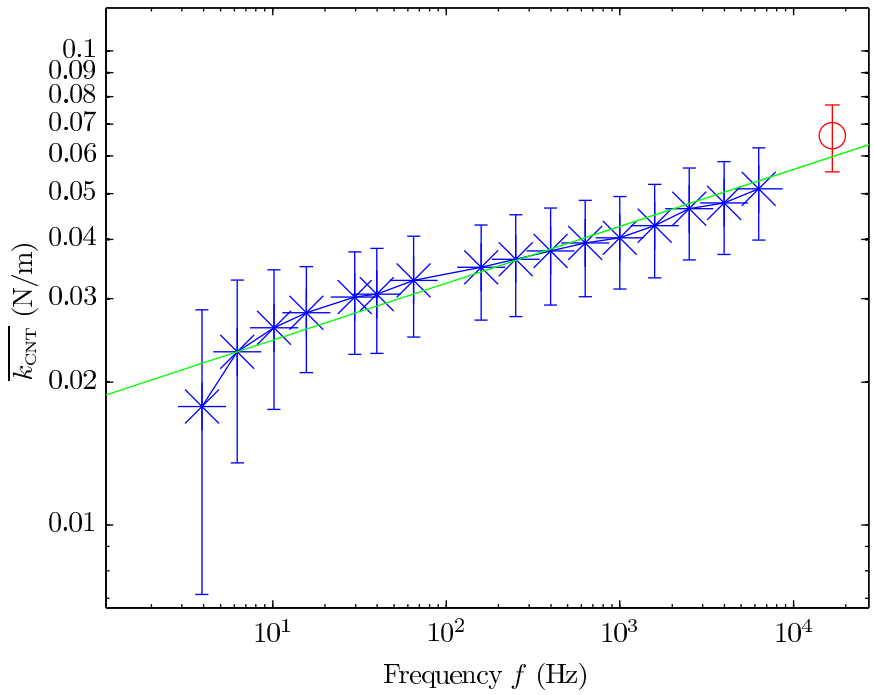

FIGURE 6.15 – Mean value of peeling stiffness $\overline{k_{CNT}}$ of every probed position on the nanotube as a function of excitation frequency f. By fitting the data, a power law with a small exponent with respect to the excitation is proposed to describe the dependence of the peeling stiffness : $\overline{k_{CNT}} = \overline{k^0_{CNT}} f^{0.12}$ with $\overline{k^0_{CNT}}$ =0.0185 N/m and f in Hz. The red circles correspond to the peeling stiffness inferred from thermal noise analysis.

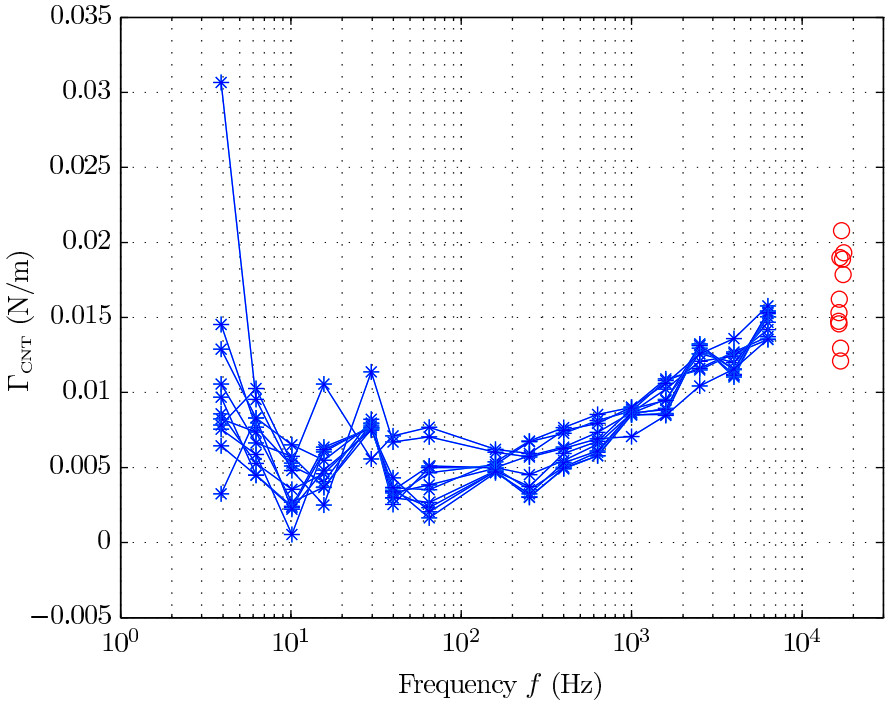

FIGURE 6.16 – Dissipation as a function of frequency at various positions along the nanotube while it is being peeled from the surface with the excitation applied by the piezo. The red circles correspond to the dissipation inferred from the time-frequency analysis of the thermal noise.

6.6 Results and discussions

6.6.1 Peeling stiffness

In the figure 6.14, we plot the real part of the peeling stiffness $k_{\mathrm{CNT}} = \mathrm{Re}(K_{\mathrm{CNT}})$ as a function of frequency, for various positions along the nanotube. k_{CNT} is obviously frequency dependent, it follows a linear relation with the logarithm of frequency. We plot the mean value of peeling stiffness $\overline{k_{\mathrm{CNT}}}$ of the nanotube for every probed length as a function of excitation f in figure 6.15. By fitting the data, we find that above 10 Hz, the averaged peeling stiffness follows a power law with a small exponent with respect to the excitation : $\overline{k_{\mathrm{CNT}}} = \overline{k^0_{\mathrm{CNT}}} f^{0.12}$ with $\overline{k^0_{\mathrm{CNT}}}$ =0.0185 N/m and f in Hz.

In figure 6.14 and 6.15, the red circles mark the peeling stiffness of the CNT calculated by the time-frequency analysis method applied to the thermal noise driven deflexion. Now we can answer to the question of section 6.3 : $\mathrm{k_{CNT}}$ increases to the peeling stiffness which is excited naturally by thermal noise induced deflexion following a simple power law in frequency. No saturation or characteristic time scale can be seen on these measurements. This result presents a novel finding about the adhesion property of the CNT with the environment.

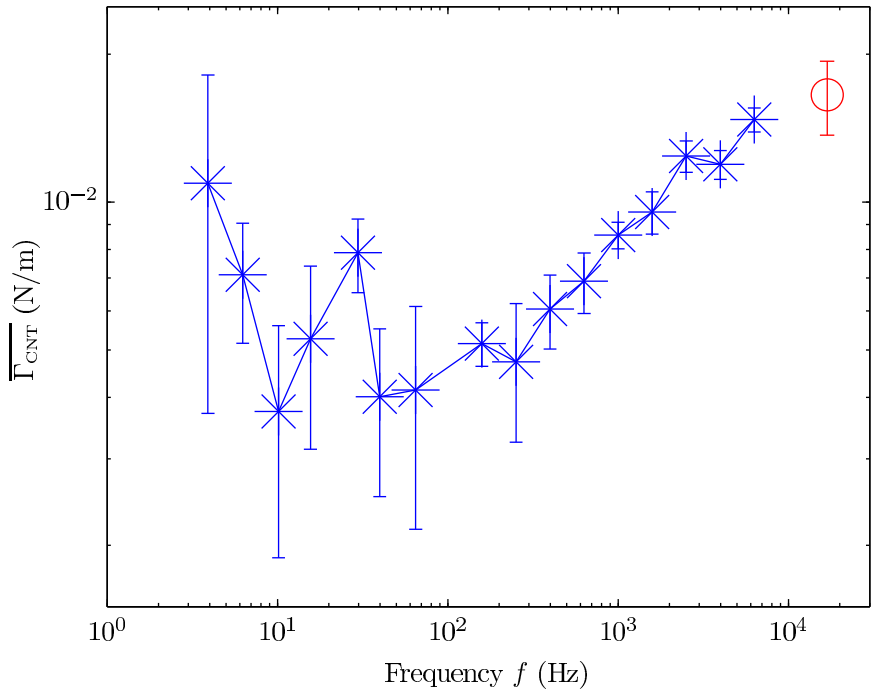

FIGURE 6.17 – The mean value of dissipation Γ_{CNT} of every probing length of the nanotube as a function of excitation frequency f.

6.6.2 Peeling dissipation

When the cantilever anchored with a nanotube is approached against a surface, the first mode of the cantilever experience an effective stiffness $k + k_{\mathrm{CNT}}$, which shifts the resonant frequency of the cantilever from f_0 to f_{CNT}, this gives us a way to compute the peeling stiffness of the nanotube around resonant frequency, it constitutes a base line for the time-frequency analysis method. Here, we can infer a similar expression to estimate the dissipation when the nanotube is being peeled. In the free standing state (out of contact), for a simple harmonic oscillator, we have :

$$\frac{1}{Q_0} = \frac{\gamma\omega_0}{k} \tag{6.12}$$

where Q_0 is the quality factor of the resonance. After the nanotube is being absorbed, we have :

$$\frac{1}{Q_{\mathrm{CNT}}} = \frac{(\gamma + \gamma_{\mathrm{CNT}})\omega_{\mathrm{CNT}}}{k + k_{\mathrm{CNT}}} \tag{6.13}$$

where Q_{CNT} the quality factor with the nanotube in contact.

The dissipation of the nanotube in contact is thus :

$$\Gamma_{\mathrm{CNT}} = \gamma_{\mathrm{CNT}}\omega_{\mathrm{CNT}} \tag{6.14}$$

$$= \frac{k}{\omega_0^2}\left(\frac{\omega_{\mathrm{CNT}}}{Q_{\mathrm{CNT}}} - \frac{\omega_0}{Q_0}\right) \tag{6.15}$$

We can thus estimate the dissipation of the nanotube Γ_{CNT} when it is being peeled without excitation from the surface as there is always thermal noise exciting the nanotube. We plot this dissipation in figure 6.16 in red circles, for various peeling positions.

Now let us focus on the dissipation of the nanotube Γ_{CNT} during the excitation process, it is deduced from the transfer function χ_{zd}. We plot this value as a function of the exciting frequency in figure 6.16. Though the dependence is not as clear as that of the peeling stiffness, we can see a tendency to increase for Γ_{CNT} with the increase of the exciting frequency, except below 30 Hz : where the curve is noisy and rather flat. Dissipation deduced from thermal noise analysis is in line with the frequency response measurement. We plot in figure 6.17 the mean value of the dissipation for all the peeling positions probed, the data as only a weak frequency dependence overall. It hints at a dissipation process that we studied for coated cantilevers in chapter 3, where internal damping processes were implied. It may come from inter-nanotube friction/interaction we may have.

Several CNTs with smaller diameter that are hard to see in SEM, entangle or bundle with the one we are peeling. These smaller nanotubes are hard to avoid in a CVD growth. During a cycle of test (approach and retract), the nanotube is reversibly attached and detached through the zipping-unzipping mechanism at entangled sites, such a zipping-unzipping process can dissipate energy, since plenty of energy is consumed to overcome the VdW attractions between the nanotubes during this unzipping process [129].

6.6.3 Nanotube defects

Another possible source of damping could be an amorphous carbon layer around the nanotube resulting from the growth process or the SEM imaging. In figure 6.19, we plot peeling stiffness of CNT k_{CNT} and the measured force F as a function of compression. We can see that during the peeling, the k_{CNT} and the measured force F present corelated changes : the higher the adhesion (larger $|F|$), the larger the stiffness. The variations are not negligible, showing that the nanotube properties are changing along its length. This is further illustrated in figure 6.19 and 6.20, where we plot the dynamic stiffness as a function of the peeling position for various frequencies (as a 3D plot in figure 6.20).

It vividly shows the relation of the 3 parameters. Along the compression, the change of peeling stiffness reflects the intrinsic property of the peeled nanotube : 3 segments linked by 2 defects can be clearly noticed, at low frequency, at compression around $z_c = 180 \rightarrow 200$ nm and $z_c = 220$ nm. Intrinsic defects during the CVD growth, or linked to an amorphous carbon layer, could be involved to explain this behavior.

6.7 Summary

Let us summarize the main points presented in this chapter :

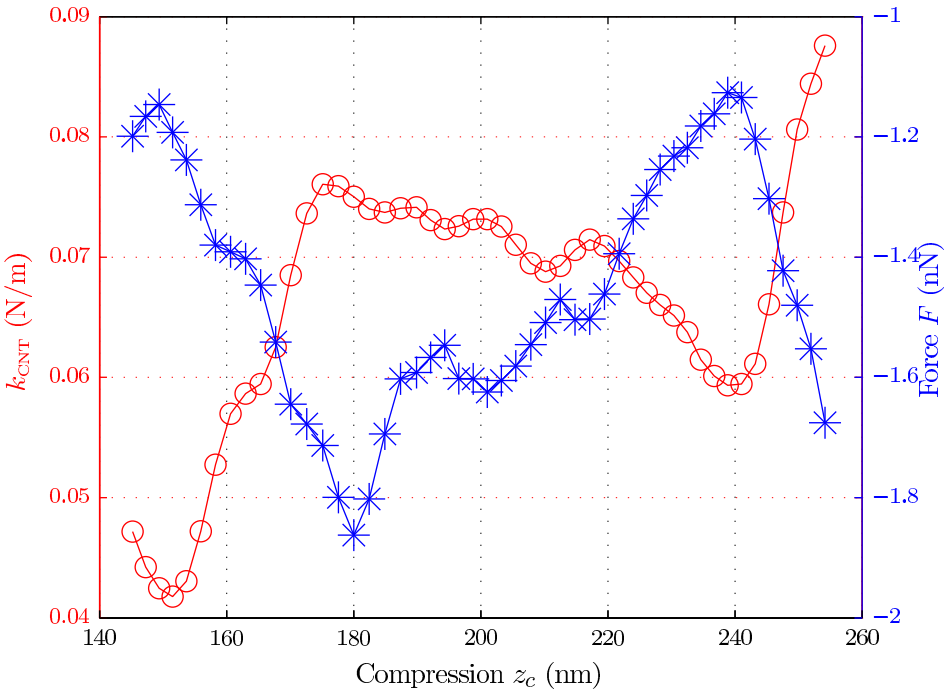

FIGURE 6.18 – Peeling stiffness of the nanotube k_{CNT} (red circle) measured through thermal noise, and quasi-static adhesion force F (black star) as a function of the CNT compression z_c.

We approach and retract a nanotube against a flat surface, and record the force as a function of the compression. We find that for some portion of the nanotube, the force curve exhibits a force plateau, which means the quasi-static peeling stiffness of the nanotube is zero since the force does not change with compression. However, when we apply a time-frequency analysis to the deflexion of the cantilever, we find that the resonant frequency of the cantilever is shifted when the nanotube is in contact with the surface with respect to the resonant frequency out of contact. This implies that a dynamic peeling stiffness of the nanotube can be computed and it presents a non zero value. Considering that this method is based on resonance shift above 10 kHz, whereas the force plateau is in a low time scale, the hypothesis is that the peeling stiffness of the nanotube depends on the frequency. When the nanotube adhere to the surface, the random thermal noise only probes the free standing part of the nanotube, the adhered part behaves like a rigid clamping.

To further test this hypothesis, when the nanotube is peeled away from the surface, we artificially apply an excitation composed of various frequencies from 4 Hz to 10 kHz. We propose a simple model for the contact, and link the peeling stiffness and the dissipation of the nanotube in contact to the transfer function from the displacement of the surface z to the deflexion of the cantilever χ_{zd}. With a specially designed scheme and a simple calibration of the piezo, we obtain the expression of peeling stiffness and the dissipation of the peeled nanotube. Power law describes

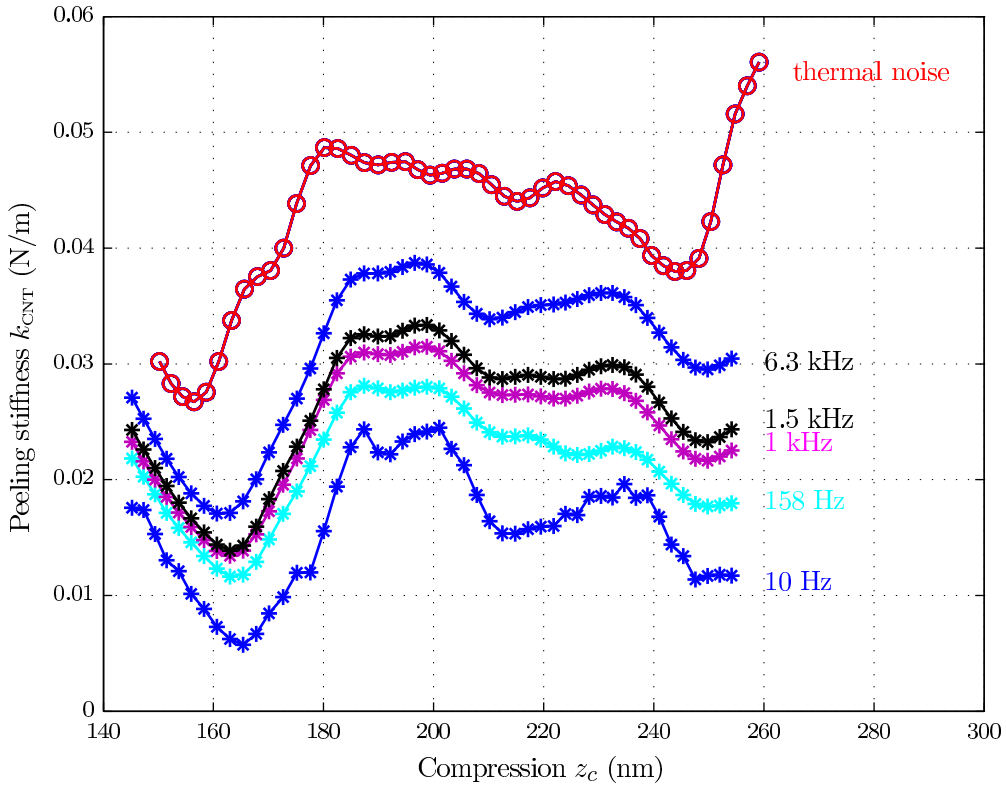

FIGURE 6.19 – Peeling stiffness k_{CNT} as a function of the compression of the nanotube for various frequencies. The obvious tendency of k_{CNT} to increase with the frequency can be found. The shape of those curves implies that the mechanical properties of the CNT are not uniform as it is being peeled with a compression from $z_c = 270\,\text{nm}$ to $140\,\text{nm}$.

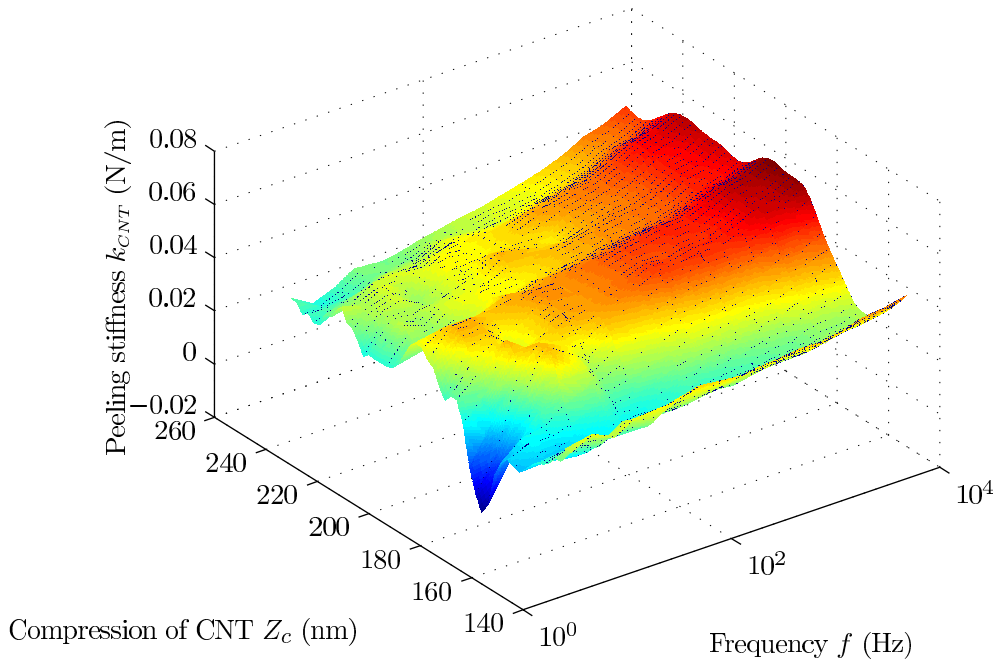

FIGURE 6.20 – 3D plot of peeling stiffness of the nanotube k_{CNT} as a function of frequency f and compression of nanotube z_c.

the frequency dependance of the average nanotube peeling stiffness : $\overline{k_{\mathrm{CNT}}} = \overline{k_0} f^{0.12}$ with $\overline{k_0} = 0.0185\,\mathrm{N/m}$ and f in Hz. The dissipation as well presents little frequency dependance. This hints at a dissipation process with no characteristic time scale, which could result from an amorphous carbon layer around the nanotube or internal friction in nanotube bundles. Heterogeneity along the nanotube for its adhesion and mechanical properties are illustrated in our experiments.

Chapitre 7

Conclusion and perspectives

I would like to give a conclusion of the thesis :

I present firstly our innovative atomic force microscope (AFM) which detection process is based on a quadrature phase differential interferometer. We measure the difference of phase between the reference beam and the sensing beam, which leads to the measurement of the deflexion of the cantilever with an outstanding resolution. We get a detection of the deflexion with a background noise down to $2 \times 10^{-14}\,\mathrm{m}/\sqrt{\mathrm{Hz}}$. This enables us to measure the power spectrum density of thermal noise driven fluctuations on a wide frequency range. The ultra low background noise give a way to observe the behaviors of the spectrum at low frequency which is related to internal dissipation of a metallic coated cantilever.

We then record the PSD of thermal induced fluctuations of the cantilever. Thanks to our highly sensitive interferometer and low background noise level, the spectrum spans on a wide frequency range from 2 Hz to 20 kHz which is far beyond the capability for commercial AFM setup. By such, we get a full view on the behaviors of the spectrum : in vacuum, the trends of the cantilever of silicon and gold coated are clearly different, slowly increasing spectrum for silicon cantilever and a $1/f$ like trend for the gold coated one. This special trend is seen as the signature of the internal damping of the cantilever. The as used SHO model is not enough for us to describe the dissipation of a cantilever with a metallic coating.

To go further, using Fluctuation-Dissipation Theorem (FDT) and the Kramers-Kronig relations, we rebuild the response function G of the cantilever from the measured PSD, any modification of the cantilever can be directly reflected on the response function. The $1/f$ like trend is related to the internal damping of the cantilever—viscoelasticity. By decreasing the air pressure in which the cantilever is working, we restrict only our focus on the viscoelastic damping since the viscous effect from the air is largely limited.

The derived viscoelastic damping $\phi(\omega)$ presents a material and frequency dependence. A simple power law ω^{α} with a small exponent α is used to characterize the damping up to 4 decades in frequency. We compute the viscoelasticity as a function of gold coating with various thicknesses, we find that a linear relation of viscoelasticity with respect to the thickness. After discussing various possible damping mechanism that have been proposed up to date, we attribute the origin of this damping to the bulk of the coating rather than to interface or the surface effects.

The result fully unveil the dissipation process to us, it shows that the choice of the

coating material is critical with respect to internal dissipation in micro-cantilevers. The commonly used gold coating is not the best choice according to this criterion, if it is the material that can not be replaced for chemical requirements, using the smallest thickness of gold is a wise way to largely minimize the damping. Our characterization procedure features an excellent resolution with measurement of overall mechanical loss tangents down to 10^{-4}. This way, the viscoelasticity due to the coating can be accurately quantified and our measurements should be useful in the perspective of testing models of internal friction, eventually leading to improved coating procedures and better performance of cantilever based sensors.

We perform a series of experiments where a single wall carbon nanotube is pushed perpendicularly against a surface, we record the adhesion force as a function of the compression. A main feature that the force curves presents is it exhibits a plateau at some range of compression. We propose a time-frequency analysis method by monitoring the resonant frequency shift of the cantilever, this allows accessing to the peeling stiffness of the nanotube at any compression during retraction process.

Elastica model is used to described the adsorbed nanotube on substrate, adhesion energy per unit length E_a is used to describe the strong interaction between the nanotube and the surface, R_a the radius of curvature of the first contact point during a nanotube's adsorption is also defined. It illustrates that the measured force plateau is equivalent in the absolute value to the adhesion energy per unit length E_a. Two boundary conditions are proposed to described the peeling mechanism of the peeling point : torque free origin and clamped origin. The following numerical simulations indicate that the two boundary conditions exhibit opposite force behaviors at the defect where the nanotube is peeled. The experimental measurement of the adhesive force validate the torque free origin being a more realistic description of the adhesion where the peeled part of nanotube include defects.

The adhesion energy per unit length E_a is measured from the force plateau, the peeling stiffness $k_{\mathrm{CNT}}^{\mathrm{peeling}}$ is obtained by time-frequency analysis method. The mechanical properties of the nanotube is then inferred by E_a and $k_{\mathrm{CNT}}^{\mathrm{peeling}}$: R_a, EI, and diameter of peeled nanoutbe D_{CNT} .

We then measure the adhesion force on various substrates. With a specially designed ramp (normal approach but slow retraction), we have sufficient time to perform precise time-frequency analysis of the deflexion of the cantilever, and get access to the dynamics stiffness of the nanotube during the peeling test. In the force curve, a long force plateau presents the most striking feature of the curve, the value of which is equivalent to the adhesion energy per unit length. It exhibits substrate dependence.

Within the framework previously discussed, measuring the adhesion energy per unit length and the peeling stiffness of the nanotube lead directly to the mechanical property of the nanotube. We measure the adhesion energy on substrates of graphite, mica, Au, Al, Pt and Si, the results unveil that E_a for Au, mica and graphite are generally larger than for Al, Pt, and Si. The adhesion energy on graphite is twice larger than that on Si. After performing time-frequency analysis of the measured deflexion for all of the substrates, we go further to estimate the diameters of as

peeled nanotube : though the adhesion energy differs on substrates, the estimated diameters are similar, all in accordance with the fact that the same nanotube is peeled in these tests.

The force curve exhibits a force plateau, which means the quasi-static peeling stiffness of the nanotube is zero since the force does not change with compression. However, when we apply time-frequency analysis of the deflexion of the cantilever, we find that the resonant frequency of the cantilever is shifted when the nanotube is in contact with the surface with respect to the resonant frequency out of contact, this implies that a dynamic peeling stiffness of the nanotube can be computed and it presents a non zero value. Considering that this method is based on resonance shift above 10 kHz, whereas the force plateau is in a low time scale, the hypothesis is that the peeling stiffness of the nanotube depends on the frequency. When the nanotube adhere to the surface, the random thermal noise only probes the free standing part of the nanotube, the adhered part behaves like a rigid clamping.

To further test this hypothesis, when the nanotube is peeled away from the surface, we artificially apply an excitation composed of various frequencies from 4 Hz to 10 kHz. We propose a simple model for the contact, and link the peeling stiffness and the dissipation of the nanotube in contact to the transfer function from the displacement of the surface z to the deflexion of the cantilever χ_{zd}. With a specially designed scheme and a simple calibration of the piezo, we obtain the expression of peeling stiffness and the dissipation of the peeled nanotube. Power law describes the frequency dependance of the average nanotube peeling stiffness : $\overline{k_{\mathrm{CNT}}} = \overline{k_0} f^{0.12}$ with $\overline{k_0} = 0.0185\,\mathrm{N/m}$ and f in Hz. The dissipation as well presents little frequency dependance. This hints at a dissipation process with no characteristic time scale, which could result from an amorphous carbon layer around the nanotube or internal friction in nanotube bundles. Heterogeneity along the nanotube for its adhesion and mechanical properties are illustrated in our experiments.

In this thesis, we use an unique tool to measure the thermal noise. The ultra low background noise, as well as its intrinsic calibration are central in our experiments. The access to the thermal noise spectrum outside resonances is a key point in the evaluation of the dissipation processes of cantilevers. Using the same geometries, this method could be applied to other materials or environmental conditions, to gather data of interest for technological applications of cantilever based sensors or nanotubes and nanowires. In the study of adhesion property of nanotubes, the innovative tool provides a direct measurement of force-distance profiles for the two interacting surfaces. Combing with the full spectrum in frequency range, it allows us access to the peeling stiffness and energy dissipation when a nanotube is in contact with the surface. This offers robust suggestions in the fabrication process of nano-systems.

Lots of questions need to be further investigated. For instance, the peeling stiffness of the nanotube presents a weak power law dependance with respect to the frequency, what is the behavior when we use horizontal rather than vertical oscillations ? Does the friction coefficient between the nanotube and the substrate obeys a similar trend with frequency ? The energy dissipation follows a weak frequency

dependance for the nanotube, what is the mechanism involved ? what role do the defects play in this process ? Answering these questions will give clearer understanding of the adhesion and dissipation at nanoscales.

Besides, investigation about the adhesion force of nanotube in a multi-field is being a new and hopeful direction as carbon nanotube is used more and more as part of micro-electromechanical systems (MEMS) or nano-electromechanical systems (NEMS), where not only is Van der Waals force involved, other complicated energy conversion (mechanical energy to thermal energy or optical energy, etc.) in the nanotube is very likely to be seen. These energy conversion can largely impact the performance of these devices. Characterizing this nano-scale energy conversion will thus result in more challenging questions in the future.

Annexe A

Kramers-Kronig relation

---

function KKreconstuct.m

```
function G=KKreconstruct(sp,fs,T)

% G=KKreconstruct(sp,fs,T)
%
% This program computes a response function starting from the noise power
% spectrum density, using Fluctuation-Dissipation Theorem (FDT) and Kramers
% Kronig (KK) relations.
%
% Input variables are :
%   sp : power spectrum density (units U^2/Hz)
%   fs : sampling frequency (Hz)
%   T  : temperature (K) (if omitted, the default value is 295K)
%
% Ouput variable is G : response function, (units U/q, where q is the unit
% of the conjugate variable of U)
%
% FDT reads : sp=4 kB T Im(G) / omega
% where kB is the Boltzmann constant and omega = 2 pi f is the pulsation
% corresponding to frequency f. The knowlegde of Sp thus leads to Im(G),
% and KK relations lead to Re(G).
%

if (nargin<3)
    kT=1.38e-23*295;
else
    kT=1.38e-23*T;
end

% number of point of input spectrum
npt=length(sp);

% round number of point to nearest power of 2
npt=2^floor(log2(npt));
```

```
% define frequency vector
f=(0:npt)/(npt)*fs/2;

% compute Im(G) from FDT
imG=sp/4/kT*2*pi.*f;

% define Im(G) for negative frequencies for FT
imG=[imG(1:npt+1) -imG(npt:-1:2)];

% compute inverse FT of Im(G) (Im(G) is an odd function, its FT is supposed
% to be purely imaginary, thus we take only the imaginary part of the
% result)
imG_t=imag(ifft(imG));

% we compute the direct FT of sign_t*imG_t (FT of an even function is
% supposed to be purely real, so we keep ony the real part)
sign_t=[0 ones(1,npt) -ones(1,npt-1)];
reG=real(fft(sign_t.*imG_t));

% limit the result to positive frequencies
G=reG(1:npt+1)+1i*imG(1:npt+1);

return
```

Annexe B

Datasheets of Au coated cantilever

Budget Sensors

AFM probe Model: ContGB-G

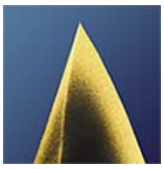

This probe has alignment grooves on the backside of the holder chip.

- Contact Mode and Special Applications
- Rotated Monolithic Silicon Probe Symmetric Tip Shape
  Chipsize: 3.4 x 1.6 x 0.3 mm
- Coating: Overall gold coating with a nominal thickness of 70nm on both sides of the cantilever. This coating also enhances the laser reflectivity of the cantilever.
- This probe uses an “on scan angle” symmetric tip to provide a more ymmetric representation of features over 200 nm.

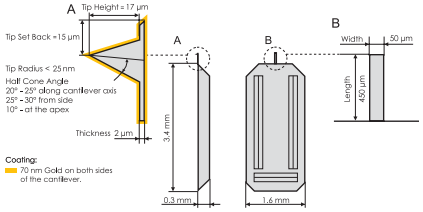

	Typical Values	Range
Resonant Frequency	13 kHz	+/- 4 kHz
Force Constant	0.2 N/m	0.07 - 0.4 N/m
Cantilever Length	450 µm	+/- 10 µm
Mean Width	50 µm	+/- 5 µm
Thickness	2 µm	+/- 1 µm
Tip Height	17 µm	+/- 2 µm
Tip Set Back	15 µm	+/- 5 µm
Tip Radius	< 25 nm	
Coating	Overall Gold Coating	
Half Cone Angle	20° - 25° along cantilever axis 25° - 30° from side 10° at the apex	

Order Code	Units in Package	Coating	Price
ContGB-G-10	10 pieces	overall Gold coating	$240
ContGB-G-50	50 pieces	overall Gold coating	$1000

Annexe C

Adsorbed Elastica

The validity of the equation (4.14) is validated by [29] as follows :

$$\begin{aligned}
E_a &= -\left.\frac{\partial E_c}{\partial L}\right|_Z \\
&= -\frac{1}{2}EI\frac{\partial}{\partial L}\int_0^L \left(\frac{\partial\theta(s,L)}{\partial L}\right)^2 \mathrm{d}s \\
&= \frac{1}{2}EI{\theta'_L}^2 - \frac{1}{2}\int_0^L \frac{\partial}{\partial L}\left(\frac{\partial\theta(s,L)}{\partial s}\right)^2 \mathrm{d}s \\
&= \frac{1}{2}EI{\theta'_L}^2 - EI\int_0^L \frac{\partial^2\theta(s,L)}{\partial L\partial s}\frac{\partial\theta(s,L)}{\partial s}\,\mathrm{d}s \\
&= \frac{1}{2}EI{\theta'_L}^2 - EI\left[\frac{\partial\theta(s,L)}{\partial L}\frac{\partial\theta(s,L)}{\partial s}\right]_0^L + EI\int_0^L \frac{\partial\theta(s,L)}{\partial L}\frac{\partial^2\theta(s,L)}{\partial s^2}\,\mathrm{d}s
\end{aligned}$$

The boundary term becomes zero when $s = 0$. In $s = L$ the boundary condition is sliding with L : $\theta(s = L, L) = \pi/2$, we have :

$$\frac{\mathrm{d}\theta(L,L)}{\mathrm{d}L} = 0 = \left.\frac{\partial\theta}{\partial s}\right|_L (L,L) + \left.\frac{\partial\theta}{\partial L}\right|(L,L)$$

$$\left.\frac{\partial\theta}{\partial L}\right|(L,L) = -\left.\frac{\partial\theta}{\partial s}\right|_L (L,L) = -\theta'_L$$

We rewrite the equation with the boundary term $-EI\theta'_L$, we have :

$$\begin{aligned}
E_a &= \frac{1}{2}EI{\theta'_L}^2 - \int_0^L \frac{\partial\theta(s,L)}{\partial L}Fsin\theta(s,L)\,\mathrm{d}s \\
&= \frac{1}{2}EI{\theta'_L}^2 + F\int_0^L \frac{\partial}{\partial L}cos\theta(s,L)\,\mathrm{d}s \\
&= \frac{1}{2}EI{\theta'_L}^2 + F\left(\frac{\partial}{\partial L}\int_0^L cos\theta(s,L)\,\mathrm{d}s - cos\theta_L\right) \\
&= \frac{1}{2}EI{\theta'_L}^2 + F\left(\frac{\partial Z}{\partial L} - cos\theta_L\right)
\end{aligned}$$

When the total energy of the CNT gets its minimization value, the coordinate of the last point Z is a constant value, and for the absorbed part of CNT, $\theta_L = \pi/2$, thus this leads $F\left(\frac{\partial Z}{\partial L} - cos\theta_L\right) = 0$. We thus have in the end :

$$E_a = \frac{1}{2}EI{\theta'_L}^2$$

Bibliographie

[1] G. Binnig, C. F. Quate, and C. Gerber, "Atomic force microscope," *Phys. Rev. Lett.*, vol. 56, pp. 930–933, Mar 1986. (Cited on page 3.)

[2] F. Hauquier, D. Alamarguy, P. Viel, S. Nol, A. Filoramo, V. Huc, F. Houz, and S. Palacin, "Conductive-probe afm characterization of graphene sheets bonded to gold surfaces," *Applied Surface Science*, vol. 258, no. 7, pp. 2920 – 2926, 2012. (Cited on page 3.)

[3] A. Sikora, M. Woszczyna, M. Friedemann, F. J. Ahlers, and M. Kalbac, "Afm diagnostics of graphene-based quantum hall devices," *Micron*, vol. 43, no. 2-3, pp. 479 – 486, 2012. (Cited on page 3.)

[4] L.-Y. Lin, D.-E. Kim, W.-K. Kim, and S.-C. Jun, "Friction and wear characteristics of multi-layer graphene films investigated by atomic force microscopy," *Surface and Coatings Technology*, vol. 205, no. 20, pp. 4864 – 4869, 2011. (Cited on page 3.)

[5] Y.-H. Ding, P. Zhang, H.-M. Ren, Q. Zhuo, Z.-M. Yang, X. Jiang, and Y. Jiang, "Surface adhesion properties of graphene and graphene oxide studied by colloid-probe atomic force microscopy," *Applied Surface Science*, vol. 258, no. 3, pp. 1077 – 1081, 2011. (Cited on page 3.)

[6] A. Winzer, C. Kraft, S. Bhushan, V. Stepanenko, and I. Tessmer, "Correcting for afm tip induced topography convolutions in protein-dna samples," *Ultramicroscopy*, vol. 121, no. 0, pp. 8 – 15, 2012. (Cited on page 3.)

[7] S. Oliveira, A. Chiorcea-Paquim, S. Ribeiro, A. Melo, M. Vivan, and A. Oliveira-Brett, "In situ electrochemical and afm study of thalidomide-dna interaction," *Bioelectrochemistry*, vol. 76, no. 1-2, pp. 201 – 207, 2009. <ce :title>Advanced design of electron-transfer pathways across biomolecular interfaces, Dedicated to Professor Lo Gorton</ce :title>. (Cited on page 3.)

[8] A. Sanchez-Sevilla, J. Thimonier, M. Marilley, JosRocca-Serra, and J. Barbet, "Accuracy of afm measurements of the contour length of dna fragments adsorbed on mica in air and in aqueous buffer," *Ultramicroscopy*, vol. 92, no. 3-4, pp. 151 – 158, 2002. (Cited on page 3.)

[9] S. Tabassum, G. C. Sharma, A. Asim, A. Azam, and R. A. Khan, "Chiral nano heterobimetallic dna receptors : Invitro binding studies, cleavage activity and dna condensation studies (tem and afm imaging)," *Journal of Organometallic Chemistry*, vol. 713, no. 0, pp. 123 – 133, 2012. (Cited on page 3.)

[10] K. E. Bremmell, A. Evans, and C. A. Prestidge, "Deformation and nano-rheology of red blood cells : An afm investigation," *Colloids and Surfaces B : Biointerfaces*, vol. 50, no. 1, pp. 43 – 48, 2006. (Cited on page 3.)

[11] Y. Yan, T. Sun, Y. Liang, and S. Dong, "Investigation on afm-based micro/nano-cnc machining system," *International Journal of Machine Tools and Manufacture*, vol. 47, no. 11, pp. 1651 – 1659, 2007. (Cited on page 3.)

[12] W. Liu, Y. Yan, Z. Hu, X. Zhao, J. Yan, and S. Dong, "Study on the nano machining process with a vibrating afm tip on the polymer surface," *Applied Surface Science*, vol. 258, no. 7, pp. 2620 – 2626, 2012. (Cited on page 3.)

[13] J. J. Fendley, "Measurement of refractive index using a michelson interferometer," *Physics Education*, vol. 17, no. 5, p. 209, 1982. (Cited on page 3.)

[14] A. J. den Boef, "Scanning force microscopy using a simple low-noise interferometer," *Applied Physics Letters*, vol. 55, no. 5, pp. 439–441, 1989. (Cited on page 3.)

[15] A. J. den Boef, "The influence of lateral forces in scanning force microscopy," *Review of Scientific Instruments*, vol. 62, no. 1, pp. 88–92, 1991. (Cited on pages 3 and 6.)

[16] P. J. Mulhern, T. Hubbard, C. S. Arnold, B. L. Blackford, and M. H. Jericho, "A scanning force microscope with a fiber-optic-interferometer displacement sensor," *Review of Scientific Instruments*, vol. 62, no. 5, pp. 1280–1284, 1991. (Cited on page 3.)

[17] D. Rugar, H. J. Mamin, R. Erlandsson, J. E. Stern, and B. D. Terris, "Force microscope using a fiber-optic displacement sensor," *Review of Scientific Instruments*, vol. 59, no. 11, pp. 2337–2340, 1988. (Cited on page 3.)

[18] D. Rugar, H. J. Mamin, and P. Guethner, "Improved fiber-optic interferometer for atomic force microscopy," *Applied Physics Letters*, vol. 55, no. 25, pp. 2588–2590, 1989. (Cited on page 3.)

[19] C. Schonenberger and S. F. Alvarado, "A differential interferometer for force microscopy," *Review of Scientific Instruments*, vol. 60, no. 10, pp. 3131–3134, 1989. (Cited on pages 3 and 4.)

[20] C. Pacholski, C. Yu, G. M. Miskelly, D. Godin, and M. J. Sailor, "Reflective interferometric fourier transform spectroscopy : a self compensating label free immunosensor using double layers of porous sio2," *Journal of the American Chemical Society*, vol. 128, no. 13, pp. 4250–4252, 2006. PMID : 16568999. (Cited on page 3.)

[21] J. D. Monnier, "Optical interferometry in astronomy," *Reports on Progress in Physics*, vol. 66, no. 5, p. 789, 2003. (Cited on page 3.)

[22] G. Meyer and N. M. Amer, "Novel optical approach to atomic force microscopy," *Applied Physics Letters*, vol. 53, no. 12, pp. 1045–1047, 1988. (Cited on page 3.)

[23] B. W. Hoogenboom, P. L. T. M. Frederix, D. Fotiadis, H. J. Hug, and A. Engel, "Potential of interferometric cantilever detection and its application for sfm/afm in liquids," *Nanotechnology*, vol. 19, no. 38, p. 384019, 2008. (Cited on page 3.)

[24] G. Jourdan, A. Lambrecht, F. Comin, and J. Chevrier, "Quantitative non-contact dynamic casimir force measurements," *EPL (Europhysics Letters)*, vol. 85, no. 3, p. 31001, 2009. (Cited on page 3.)

[25] H. J. Mamin and D. Rugar, "Sub-attonewton force detection at millikelvin temperatures," *Applied Physics Letters*, vol. 79, no. 20, pp. 3358–3360, 2001. (Cited on page 3.)

[26] L. Bellon, S. Ciliberto, H. Boubaker, and L. Guyon, "Differential interferometry with a complex contrast," *Opt. Commun.*, vol. 207, pp. 49–56, 2002. (Cited on pages 4, 6 and 10.)

[27] J. H. Dieterich and G. Conrad, "Effect of humidity on time- and velocity-dependent friction in rocks," *J. Geophys. Res.*, vol. 89, no. B6, pp. 4196–4202, 1984. (Cited on page 4.)

[28] (Cited on page 6.)
http ://micro.magnet.fsu.edu/primer/lightandcolor/prismsandbeamsplitters.html.

[29] L. Bellon, "Exploring nano-mechanics through thermal fluctuations," *Annexe-HDR-Bellon*, 2010. (Cited on pages 6, 67, 70, 71, 72, 74 and 119.)

[30] P. Paolino and L. Bellon, "Single beam interferometric angle measurement," *Opt. Commun.*, vol. 280, pp. 1–9, 2007. (Cited on page 6.)

[31] N. V. Lavrik, M. J. Sepaniak, and P. G. Datskos, "Cantilever transducers as a platform for chemical and biological sensors," *Review of Scientific Instruments*, vol. 75, no. 7, pp. 2229–2253, 2004. (Cited on pages 17 and 18.)

[32] E. Meyer, H. Josef Hug, and R. Bennewitz, *Scanning Probe Microscopy : The Lab on a Tip*. Springer, 2004. (Cited on page 17.)

[33] H.-J. Butt, B. Cappella, and M. Kappl, "Force measurements with the atomic force microscope : Technique, interpretation and applications," *Surface Science Reports*, vol. 59, pp. 1 – 152, 2005. (Cited on page 17.)

[34] T. E. Fisher, P. E. Marszalek, A. F. Oberhauser, M. Carrion-Vazquez, and J. M. Fernandez, "The micro-mechanics of single molecules studied with atomic force microscopy," *The Journal of Physiology*, vol. 520, no. 1, pp. 5–14, 1999. (Cited on page 17.)

[35] P. L. Frederix, P. D. Bosshart, and A. Engel, "Atomic force microscopy of biological membranes," *Biophysical Journal*, vol. 96, no. 2, pp. 329 – 338, 2009. (Cited on page 17.)

[36] M. M. Radmacher, "Studying the mechanics of cellular processes by atomic force microscopy," *Methods Cell Biol*, vol. 83, pp. 26–26, Jan. 2007. (Cited on page 17.)

[37] F. Sbrana, C. Sassoli, E. Meacci, D. Nosi, R. Squecco, F. Paternostro, B. Tiribilli, S. Zecchi-Orlandini, F. Francini, and L. Formigli, "Role for stress fiber contraction in surface tension development and stretch-activated channel regulation in c2c12 myoblasts," *American Journal of Physiology - Cell Physiology*, vol. 295, no. 1, pp. C160–C172, July 2008. (Cited on page 17.)

[38] B. Bhushan, X. Ling, A. Jungen, and C. Hierold, "Adhesion and friction of a multiwalled carbon nanotube sliding against single-walled carbon nanotube," *Phys. Rev. B*, vol. 77, p. 165428, Apr 2008. (Cited on pages 17, 53 and 54.)

[39] K. Y. Yasumura, T. D. Stowe, E. M. Chow, T. Pfafman, T. W. Kenny, B. C. Stipe, and D. Rugar, "Quality factors in micro- and submicro- thick cantilevers," *J. Microelectromech. Syst.*, vol. 9, pp. 117–125, 2000. (Cited on pages 17, 18 and 41.)

[40] H. J. Butt and M. Jaschke, "Calculation of thermal noise in atomic force microscopy," *Nanotechnology*, vol. 6, no. 1, p. 1, 1995. (Cited on pages 18 and 58.)

[41] Z. Djuric, "Mechanisms of noise sources in microelectromechanical systems," *Microelectronics Reliability*, vol. 40, no. 6, pp. 919 – 932, 2000. (Cited on page 18.)

[42] R. Lifshitz and M. L. Roukes, "Thermoelastic damping in micro- and nanomechanical systems," *Phys. Rev. B*, vol. 61, pp. 5600–5609, Feb 2000. (Cited on page 18.)

[43] F. Lochon, L. Dufour, D. Rebiere, U. Sampath, S. Heinrich, and F. Josse, "Effect of viscoelasticity on quality factor of microcantilever chemical sensors : optimal coating thickness for minimum limit of detection," in *Sensors, 2005 IEEE*, p. 4 pp., 30 2005-nov. 3 2005. (Cited on page 18.)

[44] P. R. Saulson, "Thermal noise in mechanical experiments," *Phys. Rev. D*, vol. 42, pp. 2437–45, 1990. (Cited on pages 18, 19 and 24.)

[45] G. I. Gonzalez and P. R. Saulson, "Brownian motion of a torsion pendulum with internal friction," *Physics Letters A*, vol. 201, no. 1, pp. 12 – 18, 1995. (Cited on page 18.)

[46] M. Kajima, N. Kusumi, S. Moriwaki, and N. Mio, "Wide- band measurement of mechanical thermal noise using a laser interferometer," *Phys. Lett. A*, vol. 263, pp. 21–6, 1999. (Cited on page 18.)

[47] K. Numata, M. Ando, K. Yamamoto, S. Otsuka, and K. Tsubono, "Wide-band direct measurement of thermal fluctuations in an interferometer," *Phys. Rev. Lett.*, vol. 91, p. 260602, 2003. (Cited on page 18.)

[48] S. Rowan, J. Hough, and D. Crooks, "Thermal noise and material issues for gravitational wave detectors," *Physics Letters A*, vol. 347, no. 1-3, pp. 25 – 32, 2005. <ce :title>Einstein Special Issue</ce :title> <ce :subtitle>Special Issue in celebration of this year's World of Physics and the centenary of Einstein's annus mirabilis</ce :subtitle> <xocs :full-name>Einstein Special Issue</xocs :full-name>. (Cited on page 18.)

[49] H. B. Callen and R. F. Greene, "On a theorem of irreversible thermodynamics," *Phys. Rev.*, vol. 86, pp. 702–710, Jun 1952. (Cited on page 18.)

[50] J. E. Sader, "Frequency response of cantilever beams immersed in viscous fluids with applications to the atomic force microscope," *Journal of Applied Physics*, vol. 84, no. 1, pp. 64–76, 1998. (Cited on pages 18, 19 and 31.)

[51] H. Hosaka, K. Itao, and S. Kuroda, "Damping characteristics of beam-shaped micro-oscillators," *Sensors and Actuators A : Physical*, vol. 49, no. 1–2, pp. 87 – 95, 1995. (Cited on pages 18 and 40.)

[52] R. Mihailovich and N. MacDonald, "Dissipation measurements of vacuum-operated single-crystal silicon microresonators," *Sensors and Actuators A : Physical*, vol. 50, no. 3, pp. 199 – 207, 1995. (Cited on page 18.)

[53] B. E. White and R. O. Pohl, "Internal friction of subnanometer a-sio2 films," *Phys. Rev. Lett.*, vol. 75, pp. 4437–4439, Dec 1995. (Cited on page 18.)

[54] C. P. Green and J. E. Sader, "Frequency response of cantilever beams immersed in viscous fluids near a solid surface with applications to the atomic force microscope," *Journal of Applied Physics*, vol. 98, no. 11, p. 114913, 2005. (Cited on pages 19 and 31.)

[55] C. A. V. Eysden and J. E. Sader, "Frequency response of cantilever beams immersed in viscous fluids with applications to the atomic force microscope : Arbitrary mode order," *Journal of Applied Physics*, vol. 101, no. 4, p. 044908, 2007. (Cited on page 19.)

[56] P. Paolino and L. Bellon, "Frequency dependence of viscous and viscoelastic dissipation in coated micro-cantilevers from noise measurement," *Nanotechnology*, vol. 20, no. 40, p. 405705, 2009. (Cited on pages 24 and 28.)

[57] S. R. de Groot and P. Mazur, *Non-equilibrium thermodynamics*. Dover, 1984. (Cited on page 29.)

[58] M. R. Paul and M. C. Cross, "Stochastic dynamics of nanoscale mechanical oscillators immersed in a viscous fluid," *Phys. Rev. Lett.*, vol. 92, p. 235501, Jun 2004. (Cited on page 31.)

[59] M. R. Paul, M. T. Clark, and M. C. Cross, "The stochastic dynamics of micron and nanoscale elastic cantilevers in fluid : fluctuations from dissipation," *Nanotechnology*, vol. 17, no. 17, p. 4502, 2006. (Cited on page 31.)

[60] A. Maali, C. Hurth, R. Boisgard, C. Jai, T. Cohen-Bouhacina, and J.-P. Aime, "Hydrodynamics of oscillating atomic force microscopy cantilevers in viscous fluids," *Journal of Applied Physics*, vol. 97, no. 7, p. 074907, 2005. (Cited on page 31.)

[61] S. Basak, A. Raman, and S. V. Garimella, "Hydrodynamic loading of microcantilevers vibrating in viscous fluids," *Journal of Applied Physics*, vol. 99, no. 11, p. 114906, 2006. (Cited on page 31.)

[62] M. K. Ghatkesar, T. Braun, V. Barwich, J.-P. Ramseyer, C. Gerber, M. Hegner, and H. P. Lang, "Resonating modes of vibrating microcantilevers in liquid," *Applied Physics Letters*, vol. 92, no. 4, p. 043106, 2008. (Cited on page 31.)

[63] C. Zener, "Internal friction in solids ii. general theory of thermoelastic internal friction," *Phys. Rev.*, vol. 53, pp. 90–99, Jan 1938. (Cited on page 41.)

[64] S. Vengallatore, "Analysis of thermoelastic damping in laminated composite micromechanical beam resonators," *Journal of Micromechanics and Microengineering*, vol. 15, no. 12, p. 2398, 2005. (Cited on page 41.)

[65] G. Sosale, S. Prabhakar, L. Frechette, and S. Vengallatore, "A microcantilever platform for measuring internal friction in thin films using thermoelastic damping for calibration," *Microelectromechanical Systems, Journal of*, vol. 20, pp. 764 –773, june 2011. (Cited on pages 41 and 42.)

[66] S. Iijima, "Helical microtubules of graphitic carbon," *Nature*, vol. 354, pp. 56–58, 1991. (Cited on pages 47 and 48.)

[67] X. Wang, Q. Li, J. Xie, Z. Jin, J. Wang, Y. Li, K. Jiang, and S. Fan, "Fabrication of ultralong and electrically uniform single-walled carbon nanotubes on clean substrates," *Nano Letters*, vol. 9, no. 9, pp. 3137–3141, 2009. PMID : 19650638. (Cited on page 47.)

[68] D. Qian, G. J. Wagner, W. K. Liu, M.-F. Yu, and R. S. Ruoff, "Mechanics of carbon nanotubes," *Applied Mechanics Reviews*, vol. 55, no. 6, pp. 495–533, 2002. (Cited on pages 48 and 53.)

[69] S. Iijima, "Single-shell carbon nanotubes of 1-nm diameter," *Nature*, vol. 363, pp. 603–605, 1993. (Cited on pages 48 and 49.)

[70] D. S. Bethune, C. H. Klang, M. S. de Vries, G. Gorman, R. Savoy, J. Vazquez, and R. Beyers, "Cobalt-catalysed growth of carbon nanotubes with single-atomic-layer walls," *Nature*, vol. 363, pp. 605–607, 1993. (Cited on pages 48 and 49.)

[71] A. Thess, R. Lee, P. Nikolaev, H. Dai, P. Petit, J. Robert, C. Xu, Y. H. Lee, S. G. Kim, A. G. Rinzler, D. T. Colbert, G. E. Scuseria, D. Tomanek, J. E. Fischer, and R. E. Smalley, "Crystalline ropes of metallic carbon nanotubes," *Science*, vol. 273, p. 483, 1996. (Cited on pages 48, 49 and 52.)

[72] M. Jose-Yacaman, M. Miki-Yoshida, L. Rendon, and J. G. Santiesteban, "Catalytic growth of carbon microtubules with fullerene structure," *Applied Physics Letters*, vol. 62, no. 2, pp. 202–204, 1993. (Cited on page 48.)

[73] T. W. Ebbesen and P. M. Ajayan, "Large-scale synthesis of carbon nanotubes," *Nature*, vol. 358, pp. 220–222, 1992. (Cited on page 49.)

[74] C. Journet, W. K. Maser, P. Bernier, A. Loiseau, D. M. L., S. Lefrant, P. Deniard, R. Lee, and J. E. Fischer, "Large-scale production of single-walled carbon nanotubes by the electric-arc technique," *Nature*, vol. 388, pp. 756–758, 1997. (Cited on pages 49 and 51.)

[75] J. Liu, A. G. Rinzler, H. Dai, J. H. Hafner, R. K. Bradley, P. J. Boul, A. Lu, T. Iverson, K. Shelimov, C. B. Huffman, F. Rodriguez-Macias, Y.-S. Shon, T. R. Lee, D. T. Colbert, and R. E. Smalley, "Fullerene pipes," *Science*, vol. 280, pp. 1253–1256, 1998. (Cited on page 51.)

[76] G. G. Tibbetts *J Cryst. Growth*, vol. 66, pp. 632–638, 1984. (Cited on page 51.)

[77] G. G. Tibbetts, "Vapor-grown carbon fibers : Status and prospects," *Carbon*, vol. 27, no. 5, pp. 745 – 747, 1989. (Cited on page 51.)

[78] G. G. Tibbetts, *Filaments and Composites in Carbon Fibers*. Kluwer Academic, Amsterdam 1990, 1990. (Cited on page 51.)

[79] G. G. Tibbe *J. Cryst. Growth*, vol. 73, pp. 431–438, 1985. (Cited on page 51.)

[80] G. Tibbetts, M. Devour, and E. Rodda, "An adsorption-diffusion isotherm and its application to the growth of carbon filaments on iron catalyst particles," *Carbon*, vol. 25, no. 3, pp. 367 – 375, 1987. (Cited on page 51.)

[81] R. Baker, "Catalytic growth of carbon filaments," *Carbon*, vol. 27, no. 3, pp. 315 – 323, 1989. (Cited on page 51.)

[82] L. L. M. R. T. K. Baker, *Novel materials in heterogeneous catalysis*. Washington, 1990. (Cited on page 51.)

[83] H. G. T. L. K. T. C. E. Snyder, W. H. Mandeville, "Hypersion catalysis international," 1989. (Cited on page 51.)

[84] H. G. Tennent, "Hyperion catalysis international," 1987. (Cited on page 51.)

[85] A. Maiti, C. J. Brabec, and J. Bernholc, "Kinetics of metal-catalyzed growth of single-walled carbon nanotubes," *Phys. Rev. B*, vol. 55, pp. R6097–R6100, Mar 1997. (Cited on page 53.)

[86] M. S. Dresselhaus, G. Dresselaus, and P. Avouris, *Carbon Nanotubes*. Springer Berlin, 2001. (Cited on page 53.)

[87] J. Y. Huang, B. Chen, Z. Q. Wang, K. Kempa, Y. M. Wang, S. H. Jo, G. Chen, M. S. Dresselhaus, and Z. F. Ren, "Superplastic carbon nanotubes," *Nature*, vol. 439, p. 281, 2006. (Cited on page 53.)

[88] H. Jiang, B. Liu, Y. Huang, and K. C. Hwang, "Thermal expansion of single wall carbon nanotubes," *Journal of Engineering Materials and Technology*, vol. 126, no. 3, pp. 265–270, 2004. (Cited on page 53.)

[89] J. Hone, M. Llaguno, M. Biercuk, A. Johnson, B. Batlogg, Z. Benes, and J. Fischer, "Thermal properties of carbon nanotubes and nanotube-based materials," *Applied Physics A*, vol. 74, pp. 339–343, 2002. (Cited on page 53.)

[90] D. Tasis, N. Tagmatarchis, A. Bianco, and M. Prato, "Chemistry of carbon nanotubes," *Chemical Reviews*, vol. 106, no. 3, pp. 1105–1136, 2006. (Cited on page 53.)

[91] H. G. Craighead, "Nanoelectromechanical systems," *Science*, vol. 290, no. 5496, pp. 1532–1535, 2000. (Cited on page 53.)

[92] B. Mahar, C. Laslau, R. Yip, and Y. Sun, "Development of carbon nanotube-based sensors mdash ;a review," *Sensors Journal, IEEE*, vol. 7, pp. 266 –284, feb. 2007. (Cited on page 53.)

[93] R. H. Baughman, A. A. Zakhidov, and W. A. de Heer, "Carbon nanotubes–the route toward applications," *Science*, vol. 297, pp. 787–792, 2002. (Cited on page 53.)

[94] O. Breuer and U. Sundararaj, "Big returns from small fibers : A review of polymer/carbon nanotube composites," *Polymer Composites*, vol. 25, no. 6, pp. 630–645, 2004. (Cited on page 53.)

[95] A. Kis, K. Jensen, S. Aloni, W. Mickelson, and A. Zettl, "Interlayer forces and ultralow sliding friction in multiwalled carbon nanotubes," *Phys. Rev. Lett.*, vol. 97, p. 025501, Jul 2006. (Cited on pages 53 and 54.)

[96] N. Peng, Q. Zhang, C. L. Chow, O. K. Tan, and N. Marzari, "Sensing mechanisms for carbon nanotube based nh3 gas detection," *Nano Letters*, vol. 9, no. 4, pp. 1626–1630, 2009. (Cited on page 53.)

[97] A. Kis and A. Zettl, "Nanomechanics of carbon nanotubes," *Phil. Trans. R. Soc. A*, vol. 366, pp. 1591–1611, 2008. (Cited on pages 53 and 76.)

[98] A. Kis, G. Csanyi, J.-P. Salvetat, T.-N. Lee, E. Couteau, A. J. Kulik, W. Benoit, J. Brugger, and L. Forro, "Reinforcement of single-walled carbon nanotube bundles by intertube bridging," *Nat Mater*, vol. 3, pp. 153–157, Mar. 2004. (Cited on page 53.)

[99] T. Rueckes, K. Kim, E. Joselevich, G. Y. Tseng, C.-l. Cheung, and C. M. Lieber, "Carbon nanotube-based nonvolatile random access memory for molecular computing," *Science*, vol. 289, pp. 94–97, 2000. (Cited on page 53.)

[100] J. Cumings and A. Zettl, "Low-friction nanoscale linear bearing realized from multiwall carbon nanotubes," *Science*, vol. 289, no. 5479, pp. 602–604, 2000. (Cited on pages 53 and 54.)

[101] S. Akita, Y. Nakayama, S. Mizooka, Y. Takano, T. Okawa, Y. Miyatake, S. Yamanaka, M. Tsuji, and T. Nosaka, "Nanotweezers consisting of carbon nanotubes operating in an atomic force microscope," *Applied Physics Letters*, vol. 79, no. 11, pp. 1691–1693, 2001. (Cited on page 53.)

[102] P. Kim and C. M. Lieber, "Nanotube nanotweezers," *Science*, vol. 286, pp. 2148–2150, 1999. (Cited on page 53.)

[103] M. C. Strus, L. Zalamea, A. Raman, R. B. Pipes, C. V. Nguyen, and E. A. Stach, "Peeling force spectroscopy : Exposing the adhesive nanomechanics of one-dimensional nanostructures," *Nano Lett.*, vol. 8, no. 2, pp. 544–550, 2008. PMID : 18189440. (Cited on pages 53 and 55.)

[104] B. Chen, M. Gao, J. M. Zuo, S. Qu, B. Liu, and Y. Huang, "Binding energy of parallel carbon nanotubes," *Applied Physics Letters*, vol. 83, no. 17, pp. 3570–3571, 2003. (Cited on page 53.)

[105] T. Hertel, R. Martel, and P. Avouris, "Manipulation of individual carbon nanotubes and their interaction with surfaces," *The Journal of Physical Chemistry B*, vol. 102, no. 6, pp. 910–915, 1998. (Cited on pages 53 and 54.)

[106] M. J. Buehler, Y. Kong, H. Gao, and Y. Huang, "Self-folding and unfolding of carbon nanotubes," *Journal of Engineering Materials and Technology*, vol. 128, no. 1, pp. 3–10, 2006. (Cited on page 53.)

[107] Z. Li, P. Dharap, S. Nagarajaiah, R. P. Nordgren, and B. Yakobson, "Nonlinear analysis of a swcnt over a bundle of nanotubes," *International Journal of Solids and Structures*, vol. 41, no. 24-25, pp. 6925 – 6936, 2004. (Cited on pages 53 and 54.)

[108] T. Tang, A. Jagota, C.-Y. Hui, and N. J. Glassmaker, "Collapse of single-walled carbon nanotubes," *Journal of Applied Physics*, vol. 97, no. 7, p. 074310, 2005. (Cited on pages 53 and 54.)

[109] W. Zhou, Y. Huang, B. Liu, J. Wu, K. Hwang, and B. Wei, "Adhesion between carbon nanotubes and substrate : Mimicking the gecko foot-hair," *Nanoscale Research Letters*, vol. 2, no. 3, p. 175, 2007. (Cited on page 53.)

[110] W. Zhou, Y. Huang, B. Liu, K. C. Hwang, J. M. Zuo, M. J. Buehler, and H. Gao, "Self-folding of single- and multiwall carbon nanotubes," *Applied Physics Letters*, vol. 90, no. 7, p. 073107, 2007. (Cited on page 53.)

[111] M. J. Buehler, "Mesoscale modeling of mechanics of carbon nanotubes : Self-assembly, self-folding, and fracture," *Journal of Materials Research*, vol. 21, pp. 2855–2869, 2006. (Cited on page 53.)

[112] T. Hertel, R. E. Walkup, and P. Avouris, "Deformation of carbon nanotubes by surface van der waals forces," *Phys. Rev. B*, vol. 58, pp. 13870–13873, Nov 1998. (Cited on pages 53 and 54.)

[113] M. R. Falvo, R. M. Taylor, A. Helser, V. Chi, F. P. B. Jr, S. Washburn, and R. Superfine, "Nanometre-scale rolling and sliding of carbon nanotubes," *Nature*, vol. 397, pp. 236–238, 1999. (Cited on page 54.)

[114] R. LÃ$\frac{1}{4}$thi, E. Meyer, H. Haefke, L. Howald, W. Gutmannsbauer, and H. J. GÃ$\frac{1}{4}$ntherodt, "Sled-type motion on the nanometer scale : Determination of dissipation and cohesive energies of c60," *Science*, vol. 266, no. 5193, pp. 1979–1981, 1994. (Cited on page 54.)

[115] C. Ke, M. Zheng, G. Zhou, W. Cui, N. Pugno, and R. N. Miles, "Mechanicall peeling of free-standing single-walled carbon-nanotube bundles," *Small*, vol. 6, no. 3, pp. 438–445, 2010. (Cited on pages 54 and 55.)

[116] A. P. Russell, *A contribution to the functional morphology of the foot of the tokay*, vol. 176. J. Zoo. London, 1976. (Cited on page 55.)

[117] K. Autumn, M. Sitti, Y. A. Liang, A. M. Peattie, W. R. Hansen, S. Sponberg, T. W. Kenny, R. Fearing, J. N. Israelachvili, and R. J. Full, "Evidence for van der waals adhesion in gecko setae," *Proceedings of the National Academy of Sciences*, vol. 99, no. 19, pp. 12252–12256, 2002. (Cited on page 55.)

[118] R. Ruibal and V. Ernst, "The structure of the digital setae of lizards," *Journal of Morphology*, vol. 117, no. 3, pp. 271–293, 1965. (Cited on page 55.)

[119] U. Hiller, "Comparative studies on the functional morphology of two gekkonid lizards," *J. Bombay Nat. Hist. Soc.*, vol. 73, pp. 278–282, 1975. (Cited on page 55.)

[120] L. Qu, L. Dai, M. Stone, Z. Xia, and Z. L. Wang, "Carbon nanotube arrays with strong shear binding-on and easy normal lifting-off," *Science*, vol. 322, no. 5899, pp. 238–242, 2008. (Cited on page 55.)

[121] M. Ishikawa, R. Harada, N. Sasaki, and K. Miura, "Visualization of nanoscale peeling of carbon nanotube on graphite," *Applied Physics Letters*, vol. 93, no. 8, p. 083122, 2008. (Cited on pages 55 and 58.)

[122] M. Ishikawa, R. Harada, N. Sasaki, and K. Miura, "Adhesion and peeling forces of carbon nanotubes on a substrate," *Phys. Rev. B*, vol. 80, p. 193406, Nov 2009. (Cited on pages 55 and 58.)

[123] M. C. Strus, R. R. Lahiji, P. Ares, V. Lopez, A. Raman, and R. Reifenberger, "Strain energy and lateral friction force distributions of carbon nanotubes manipulated into shapes by atomic force microscopy," *Nanotechnology*, vol. 20, no. 38, p. 385709, 2009. (Cited on pages 55 and 58.)

[124] M. C. Strus, C. I. Cano, R. B. Pipes, C. V. Nguyen, and A. Raman, "Interfacial energy between carbon nanotubes and polymers measured from nanoscale peel tests in the atomic force microscope," *Composites Science and Technology*, vol. 69, no. 10, pp. 1580 – 1586, 2009. <ce :title>CNT-NET 07 Special Issue with regular papers</ce :title>. (Cited on page 58.)

[125] J. Buchoux, L. Bellon, S. Marsaudon, and J. Aimé, "Carbon nanotubes adhesion and nanomechanical behavior from peeling force spectroscopy," *The European Physical Journal B - Condensed Matter and Complex Systems*, vol. 84, pp. 69–77, 2011. 10.1140/epjb/e2011-20204-1. (Cited on pages 67 and 81.)

[126] L. Landau and E. Lifchitz, *Theory of elasticity*. Mir, Moscow, 1967. (Cited on pages 68 and 76.)

[127] J. W. Obreimoff, "The splitting strength of mica," *Proceedings of the Royal Society of London. Series A*, vol. 127, no. 805, pp. 290–297, 1930. (Cited on page 69.)

[128] U. Seifert, "Adhesion of vesicles in two dimensions," *Phys. Rev. A*, vol. 43, pp. 6803–6814, Jun 1991. (Cited on page 69.)

[129] Y. Li and M. Kroger, "Viscoelasticity of carbon nanotube buckypaper : zipping-unzipping mechanism and entanglement effects," *Soft Matter*, vol. 8, no. 30, pp. 7822–7830, 2012. (Cited on page 107.)